Design and Characterization of Microwave Assisted Plasma Spray Deposition System:

Application to Eu Doped Y_2O_3 Nano-Particle Coatings

by
Marek Radosław Merlak

A thesis submitted in partial fulfillment
of the requirements for the degree of
Master of Science
Department of Physics
College of Arts and Sciences
University of South Florida

Major Professor: Sarath Witanachchi, Ph.D.
Pritish Mukherjee, Ph.D.
Myung Kim, Ph.D.

Date of Approval:
May 14, 2010

Keywords: Pyrolysis, Microwave Plasma, Y_2O_3:Eu Phosphor, Nano-Particle

TABLE OF CONTENTS

LIST OF TABLES

LIST OF FIGURES

Design and Characterization of Microwave Assisted Plasma Spray Deposition System: Application to Eu Doped Y_2O_3 Nano-Particle Coatings

Marek Radosław Merlak

ABSTRACT

This thesis presents a Microwave Plasma Assisted Spray Deposition (MPASD) system design, characterization, and application to produce nano-sized particle coatings of metal oxides. A commercially available rectangular waveguide microwave power delivery system is utilized to initiate and sustain the plasma discharge within the customized plasma applicator where micron-sized droplets of a metal ion solution are heated to evaporate the solvent and thermally process the resulting nano-sized particles. The investigation of optimum conditions for oxygen, argon, and air plasma ignition in the MPASD system was presented. Measured electron temperature of the plasma was between 6000K and 40000K for the plasma conditions used in the MPASD process. Successful deposition of Y_2O_3:Eu nano-particles using the MPASD system was achieved. MPASD process allows control of the particle's properties, shown through XRD and photoluminescence studies of the Y_2O_3:Eu coatings. The MPASD process settings effect on particles activated doping concentration and, as a result, its photoluminescence was shown.

CHAPTER 1. Nanotechnology

The topic of this manuscript is the design, characterization, and application of a system to produce nano-particle coatings. This chapter starts with a brief introduction to nanotechnology.

Nanotechnology has been hailed to be the technology of the 21st century. The rapid growth of our knowledge in this field and its many existing and predicted applications are critical to science, technology, economy, and most importantly to the well being of people. There are multitudes of efforts from scientific communities, commercial entities, governments and public to envision the predicted advancements nanotechnology promises to bring.

When trying to define what is nano-science often the dimension is the criteria of choice. The most often utilized criteria is that at least one dimension of an object is between 1nm and 100nm (nano.gov). However, a more insightful definition of nano-science uses system properties as criteria and it states that:

> *Nano-science is dealing with functional systems based on the use of sub-units with specific size-dependent properties or of individual or combined functionalized sub-units.* (Schmid 2006)

In essence, this definition does not specify the size limits but that the size is such that, size change varies the properties of material or combination of such materials. This definition better explains what nano-science is about: it is about controllable or variable properties of materials.

1.1. History of Nano-Technology

When nano-science and technology start is difficult to say. There are some early examples of nanotechnology. Nearly 2000 years ago Greeks and Romans used dyeing methods (Walter 2006) described later by Arabian authors of medieval times to dye their gray hair black. This method worked because dyeing process created nano-crystals of PbS within the hair volume. The Lycurgus cup made by Romans in 4^{th} century A.D. is an example of ancient nanotechnology as its glass optical properties are due to the 60nm nano-particles of gold-silver alloy dispersed within it (Freestone 2007). A similar technique was in use since medieval times for creating stained glass (Min'ko 2008). Silver and copper nano-clusters found in the luster decorations of Italian pottery were made by the method described by Piccolpasso in 1557 (Borgia 2001, Padovani 2004). Photography developed as early as 1790 (Lichfield 1973) is an example of nanotechnology since it relies on decomposition of silver halides into silver nano-particles under exposure of light. These early applications show that nanotechnology is not a new topic.

However, the understanding of the nanotechnology is a work of modern science. It is worthy to mention Michael Faraday in his 1857 lecture titled "Experimental Relations of Gold to Light" presented his work in gold particle suspension that we know

now to be nano-particles. This lecture is not only the beginning of colloidal chemistry but could be the earliest scientific work in nano-science. In his work Faraday investigated the light interaction with particles "very minute in its dimensions", and he concluded that "phenomena appeared to indicate that a mere variation in the size of its particles gave rise to a variety of resultant colours" (Faraday 1857). Later work of Gustav Mie quantified the light interaction with the small particles that Faraday observed (Mie 1908). The first instruments to probe into matter beyond what the optical microscope allowed was the electron microscope invented by Max Knott and Ernst Ruska in 1931 (Ruska 1987).

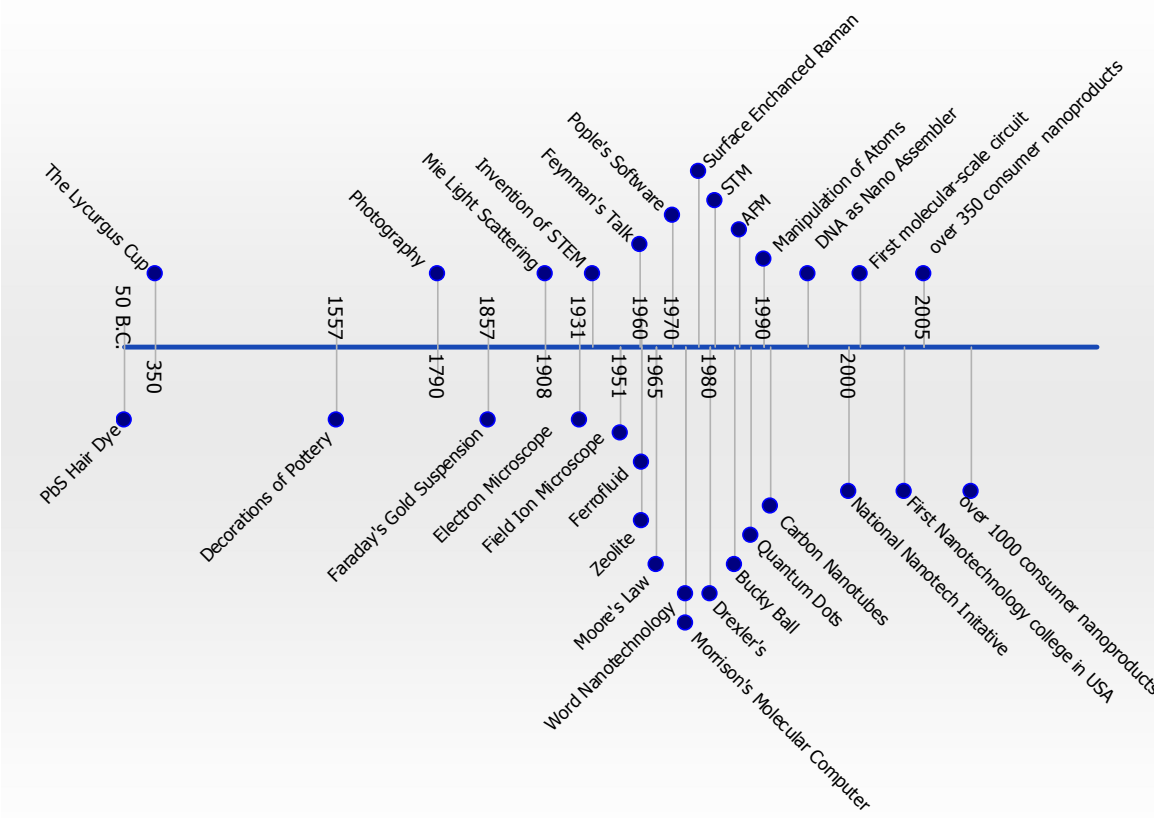

Figure 1.1. Timeline of nanotechnology selected events.

This invention, which was improved in later years, allowed observation of atoms using the field-ion electron microscope developed by Erwin Mueler in 1951 (Melmed

1995). The invention of new microscopy was important for the field of nano-science. The ancients did not know about nano-sized particles of PbS in their hair or that the nano-particles of gold and silver within the glass that absorb the blue light resulted in the deep red color of the light coming through the Lycurgus Cup. They could not know because one cannot see the nano-particles with the bare eye. Faraday through his systematic study suspected particles too small to see were responsible for the red color of the gold suspension but the verification did not come until necessary instrumentation was developed nearly a century later.

Nano-science and technology, as we know it today, is often said to start with Richard Feynman's talk titled "There is Plenty of Room at the Bottom" (Fenman 1959). This is the beginning of the so-called Feynman-STM-IBM-NNI history of nanotechnology: introduction of the field by Feynman, followed by the invention of the scanning tunneling microscope (STM) (Golovchenko 1986), manipulation of atoms by scientists at IBM (Eigler 1990), and the foundation of the national nanotechnology institute (NNI) (nano.gov). The timeline presented in Figure 1.1 outlines some of the more important discoveries and inventions relating to nanotechnology. However, history, goals, market forces, and even politics have complicated the nanotechnology story.

For example, the beginning of modern nanotechnology is unclear. Feynman's talk is often introduced in nano-science and engineering classrooms as the birth of nano-science, and his talk is said to inspire the research in nanotechnology. However, Feynman's role was more that of the Nostradamus of nanotechnology. Many scientists such as the inventors of the STM and AFM stated, years after Feynman's talk, that "There is Plenty of Room at the Bottom" lecture did not influence their work or they

were not aware of it at the time of their discoveries. This suggests that his talk was not as influential or important as it is often credited. In addition, Feynman did not do any work in the nano-science field, and his talk, at the time of its introduction, sparked little debate and went mostly unnoticed (Toumey 2005, 2008). It is interesting to notice that it is not until 1974 that Norio Taniguchi uses the term nanotechnology.

Deciding the birth date of nanotechnology sparks controversy, but not as much as deciding what is its direction: the nano-science road is littered with conflicting views and directions, and sometimes with the ideas of the impossible. Richard Smalley and Eric Drexler are both highly regarded scientists, yet their conflicting ideas sparked the Drexler–Smalley open letters exchange (Baum 2003). Drexler in his work strongly emphasized his nano-assembler direction for nanotechnology (Drexler 1986, 2003). Drexler approaches nanotechnology in an engineering manner: the nano-assembler performs tasks and can self-replicate, in turn, a large amount of them can quickly build devices in a nano-factory manner. Smalley opposes such direction pointing to problems in this concept. His "fat fingers" and "sticky fingers" arguments show that mechanical nano-assembler would not be able to manipulate atoms or molecules in the precise or reliable manner required. In addition, he counters the Drexler argument of utilizing enzymes or ribosome as manipulators by noticing that such method requires water chemistry. This would greatly limit the applications and would not be able to create the devices that Drexler envisioned.

The history and direction of the nanotechnology is unclear but its growth is real, as can be seen by the growth in research and applications (Hullmann 2007, Salerno 2008).

1.2. Nano-Particles

The focus of this manuscript is on nano-particles and a technique for their synthesis. Nano-particles are of great interest for science and industry for their new or enhanced properties. The changing properties of materials in nano-scale are due to the quantum and surface effects occurring in small-dimensioned objects. These two phenomena are discussed separately. The thermal, mechanical, magnetic, chemical, conductivity, and optical properties of nano-particles are of great interest for scientific as well as commercial use.

Some examples of chemical and physical methods for producing nano-crystalline materials include sol-gel synthesis (Bui 2009), laser-vaporization (Geohegan, Abdelsayed 2007), gas phase condensation (Champion, Guo 2007), plasma processing (Jerby 2009), mechano-chemical synthesis (Yang 2003, Tsuzuki 2004), combustion synthesis (Sun 2008), and sputtering techniques (Dreesen 2009, Chen 2008).

The optimal synthesis process should produce particles with small diameter (less than 100nm), narrow size distribution, and crystalline structure. Small diameters are preferred because above 100 nm, the properties tend to approach those of bulk materials. Narrow particle distributions are preferred for potential application purposes. Crystalline phase particles often have the desired properties over the amorphous phase.

1.2.1. Surface Effect

Often the ratio of surface atoms to the bulk atoms, or dispersion, is the source of the changing properties of the material on the nano-scale. The atoms at the surface do not have the ability to form the same bonds as the bulk atoms do. This creates dangling bonds

and changes in crystal structure of the surface. Therefore, the ratio of an objects surface area to its volume does affect the properties of the object.

For an object with spherical geometry the surface area ratio to its volume is

$$\frac{A}{V} = \frac{4\pi \cdot R^2}{\frac{4}{3}\pi \cdot R^3} = \frac{3}{R} \tag{1.1}$$

Since the ratio is inversely proportional to the objects radius, then the ratio is small and does not change significantly for large objects. However, for small objects the ratio increases significantly with decreasing radius. This is the main reason why the surface effects are largely unnoticeable for objects with macroscopic dimensions, while the surface effects are significant on the nano-scale. However, for real objects with nano-scale dimensions the ratio of surface atoms to the total number of atoms is a more appropriate estimate of the surface effect. For a cubic crystal the ratio is

$$F = \frac{6 \cdot n^2 - 12 \cdot n - 8}{n^3} = \frac{6}{N^{\frac{1}{3}}}\left(1 - \frac{2}{N^{\frac{1}{2}}} + \frac{8}{6 \cdot N^{\frac{2}{3}}}\right) \approx \frac{6}{N^{\frac{1}{3}}} \propto \frac{1}{R}. \tag{1.2}$$

Because the ratio varies as $N^{-\frac{1}{3}}$ then the surface effect on the nano-scale can change greatly with the dimensions of the particle while the change is unnoticed with objects of larger dimensions. This is because for the smallest nano-particles all atoms can be surface atoms, while larger particles, like 100nm lithium nano-particles, ~5% of atoms are surface atoms (N~10^6).

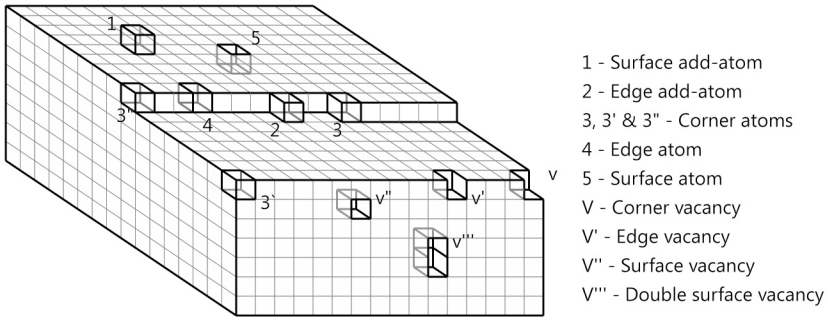

Figure 1.2. Example of surface atoms and surface vacancies in cubic structure.

Surface atoms behave differently than bulk atoms, and not all surface atoms necessary behave alike. For example, in the cubic crystal in Figure 1.2, the lack of some of the nearest neighbors for the surface atoms creates dangling bonds. The number of nearest neighbor atoms affects the number of dangling bonds for each atom and it depends on the location on the surface. Similarly, a vacancy at a surface creates dangling bonds from the atoms surrounding the vacancy. Dangling bonds could be terminated to lower the surface energy by creating bonds with other surface atoms, by absorbing atoms from the surrounding atmosphere that will terminate the dangling bonds, or by changing the chemistry of the surface in multi-element compounds (Kawarada 1996, Shiraishi 1996, Camillone 2002).

1.2.2. Quantum Effects

On the other hand, the quantum effects are due to the small dimensions of the object and decreasing number of atoms within the particle. As the size of the particle decreases, the interaction of the particle with light changes. The magnetic particles can become magnetic single domains. The number of energy levels within the energy band of

the crystal decrease as the number of atoms decrease. The density of states function changes depending on dimensionality and is summarized in Figure 1.3.

The quantum effect can be explained using model of single electron being confined within infinite square well potential. Time independent Schrödinger equation is

$$-\frac{\hbar}{2m}\Delta\Psi(r)+V(r)\Psi(r)=E\Psi(r) \tag{1.3}$$

For square well of width L, zero potential inside, and infinite potential outside the solution is

$$E_n=\frac{n^2\hbar^2\pi^2}{2mL^2} \tag{1.4}$$

The discrete energy levels depend on the square inverse of the dimension of the object. Although, nano-sized objects are multi-electron this simple example can be extended to illustrate the size effect on small-dimensioned objects.

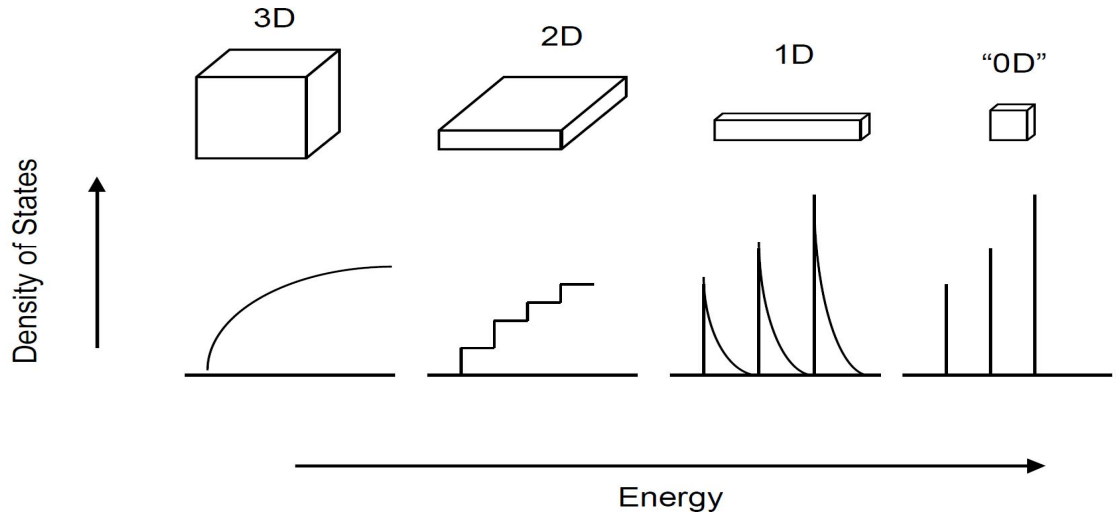

Figure 1.3. The density of states function for bulk (3D), thin film (2D), nanowire (1D), and quantum dot (0D).

If only one dimension is in the nano-size range then the surface is often referred to as a thin film. Due to the thickness of such surface quantum, effects can be observed

that can be explained by modeling the surface as a two-dimensional object. Similarly, if two dimensions are small enough quantum effects occur that can be explained using a one-dimensional model. Examples of such 1D objects are nanowire and nanotubes. If the size of the object in all three dimensions is small enough quantum effects occur that can be explained by the zero-dimensional model. Such 0D objects are often referred to as quantum dots(QD).

1.2.3. Nano-Particle Properties

The study of nano-structures is driven by the ability of nano-structures to have different properties from the bulk materials. For nano-particles, the changes observed in thermal, mechanical, magnetic, chemical, or optical properties create great interest in scientific and commercial worlds.

The thermal properties of particles on the nano-scale are different from the bulk, such as the melting point of particles was observed to change (Goldstein 1992, Sun 2007). This allows for lower temperature processing of materials such as in sintering. The thermal conductivity of fluids is enhanced in the presence of suspended nano-particles (Keblinski 2001, Das 2003). The thermal effects are often due to the high hydrostatic pressure due to particle surface curvature.

Super elasticity has been observed in nano-structured ceramics (Gao 2006) and thin films (Rumpf 2005). Rumpf also has shown enhanced tensile strength in thin films. Strengthening of nano-structured materials has been observed and modeled (Scattergood 2007).

A particle's size as well as its shape can greatly affect the magnetic properties of nano-particles. Of most interest is the single domain and super paramagnetic effects observed in nanoparticles (Lu 2007). Magnetic nano-particles are of great interest in biology and medicine for applications in therapy, drug delivery and diagnostic (Pankhurst 2003).

The large surface area to volume ratio of nano-particles can greatly increase the chemical activity of a material. This is utilized to increase the sensitivity of chemical sensors and the effectiveness of the catalysts (Astruc 2005). It was found that these materials have higher organic compound adsorbity than that of activated carbon.

The small size of nano-particles can create quantum confinement of an electron, often called quantum dot (Meijerink). Quantum confinement can change the overlap of the wave function of the doping atoms with those of host atoms resulting in more efficient interaction between the doping and host atoms. The decrease in size causes a blue shift in absorption that reflects the band gap increase of the host material, increased photoluminescence, and decreased luminescent decay as shown in published studies (Bhargava 1994).

1.3. Hazards of Nanotechnology.

Nanotechnology has allowed us to discover new and exciting applications for materials, but there is a great risk that these newly discovered materials can cause harm to health and the environment. Just like Maria Skłodowska-Curie, today's scientists are looking for discoveries but sometimes not realizing the potential harm to themselves. In

addition, the discoveries can harm society through their effects on health and the environment.

For example, a carbon nanotube with its very small diameter yet comparatively very large length, and many interesting properties is proposed to solve many technological issues. Many applications of carbon nanotube are studied from electronic devices (Javey 2003) to mechanical actuators (Baughman 1999). However, studies show that carbon nanotubes can be as dangerous as the now infamous asbestos (Poland 2008).

Another example of problematic nanotechnology application is nano-particle silver. Nano-particle silver is one of the most common materials used in nanotechnology-based consumer products. Because of its antimicrobial properties the nano-particles of silver are used in bedding, washers, water purification, toothpaste, nursing nipples and bottles, toys, and kitchen utensils. However, the EPA decided to regulate washing machines in similar way as they regulate pesticides. Their decision was made because, in contrast to manufacturers claims, nano-particles of silver were released with wastewater (EPA 2008). This poses question about other applications of nano-particle silver: is it safe?

In light of the fast growing nanotechnology field governmental regulatory bodies struggles to protect society from the potential harm. This is often difficult since the materials once known to be safe, can become dangerous just by being nano-sized. Possible dangers can appear in the research, production, use, and disposal of products that utilize nanotechnology.

1.4. Thesis Outline

The thesis topic is the design and characterization of a microwave plasma assisted spray deposition system, its application to grow Y_2O_3:Eu nanoparticle coatings, and the characterization of these coatings. A brief description of the spray pyrolysis process is presented in Chapter 2 of this manuscript. The design of the Microwave Plasma Assisted Spray Deposition (MPASD) system and its characterization are presented in Chapters 3 and 4, respectively. The deposition and characterization of Y_2O_3:Eu is presented in Chapter 5.

CHAPTER 2. Spray Pyrolysis

There are multiple methods of producing nano-scale particles. However, for many materials, these methods require a post-annealing step to create the desired crystalline phase. The annealing step often leads to particle agglomeration and prevents depositions on temperature sensitive surfaces such as polymers. In addition, the high temperature materials often are difficult to make using standard techniques because of the temperature limitations of the process. To eliminate agglomeration of the particles many techniques utilize a surfactant that terminates the surface dangling bonds. Although the surfactant reduces agglomeration, often the surfactant causes changes in the surface effect of the nano-particle and obscure quantum effects within the particle.

There is a need to overcome these limitations, as ability to produce size controlled, surfactant free, and crystalline nano-particles of high temperature materials can lead to new discoveries and applications. The spray pyrolysis techniques can achieve such results.

2.1. Spray Pyrolysis Overview

Pyrolysis is a process by which a solid (or liquid) undergoes degradation of its chemicals into smaller volitale molecules under heat, without interaction with

oxygen or any other oxidants, that is necessary for almost all solids (or liquids) to burn (Stauffer 2003).

Pyrolysis is one form of the more general thermolysis process. The MPASD system described in Chapters 3 and 4 is a pyrolysis system. However, the application of the MPASD system presented in Chapter 5 is, strictly speaking, not a pyrolysis process but technically a thermolysis process since the carrier gas used was oxygen. Nevertheless, the term pyrolysis will be used throughout the manuscript for all of the MPASD processes due to its similarity to other spray pyrolysis techniques. Other authors had allowed for this discrepancy, one example being the flame spray pyrolysis (Madler 2002).

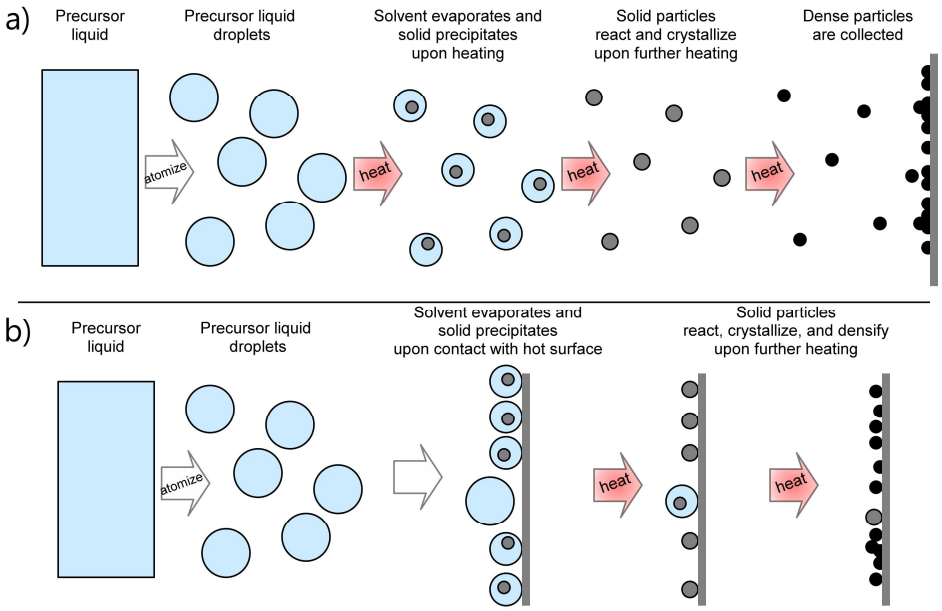

Figure 2.1. Spray pyrolysis process. The pyrolysis occurs (a) in flight of the atomized precursor droplets or (b) upon contact on a hot surface.

Spray pyrolysis is a process of pyrolysis of a sprayed material. This can be achieved by thermally processing the spray after its atomization but before reaching a surface, or the pyrolysis can occur on a hot surface (Figure 2.1). The product of spray pyrolysis can be gas, liquid, or a solid. This manuscript describes a processs of spray

pyrolysis where the pyrolysis occurs before reaching surface and focuses on a final product that is a powder coating of solid particles.

The topic most relevant to this manuscript is the application of spray pyrolysis to produce particles. In such an application, a precursor is atomized and the pyrolysis is achieved by heating the atomized droplets. Upon heating, the solvent is removed and the reaction occurs where the solid product of pyrolysis forms a particles. Figure 2.1b presents the process where the precursor is a liquid solution and the particles are captured on the substrate surface. The process of pyrolysis can be as simple as solid precipitation within droplets or more complicated as in metal-citric chelate pyrolysis.

2.2. Spray Pyrolysis Atomization Techniques

The precursor can be atomized using several techniques. The most common means of atomization are the liquid jet atomizer, air-assisted atomizer, jet instabilities atomizer, surface instabilities atomizer, and the electrostatic spray atomizer techniques. The basic characteristic of each method are summarized in Table 2.1.

Table 2.1. Comparison of different liquid atomization techniques (Lucas 1994).

	Liquid jet atomizer	Air-assisted atomizer	Jet instabilities	**Surface instabilities**	Electrostatic spray
Droplet size dispersion	Broad	Broad	Very narrow	**Narrow**	Very narrow
Independent gas and liquid flow rates	Independent	Gas dependent	Independent	**Independent**	Liquid dependent
Possible liquid flow rate	Small to large	Small to large	Very small	**Small**	Very small
Initial kinetic energy of the droplet	Very high	High	High	**Very low**	Small
Design and fabrication technology	Intermediate	Easy	Difficult	**Intermediate**	Difficult

The liquid jet atomizer is a hydraulic method where a liquid is pumped through a narrow opening. The liquid turbulence in the jet, jet surface instabilities, and jet velocity profile are just few methods of atomization of the liquid jet (Reitz 1982, Ibrahim 1999). This method allows for large material flow, but suffers from broad droplet size distribution.

The air-assisted atomizer allows atomizing the liquid stream by pheumatic means. The liquid jet or droplets are mixed (internal mix method) before reaching a nozzle, the turbulence of the mixture causes atomization of the stream. In the external mix method the liquid jet is ejected similarly, but not at a large pressure, as in the liquid jet atomizer, the atomization is achieved by the air stream impacting on the jet. The air-assisted atomization methods are widely used in industrial applications, especially in paint systems and fuel injectors for turbine engines (pnr-nozzles.com, Watanawanyoo 2009). Although the air-assisted atomizers are easy in application, their broad droplet size distribution and the high base flow rates limit its applications.

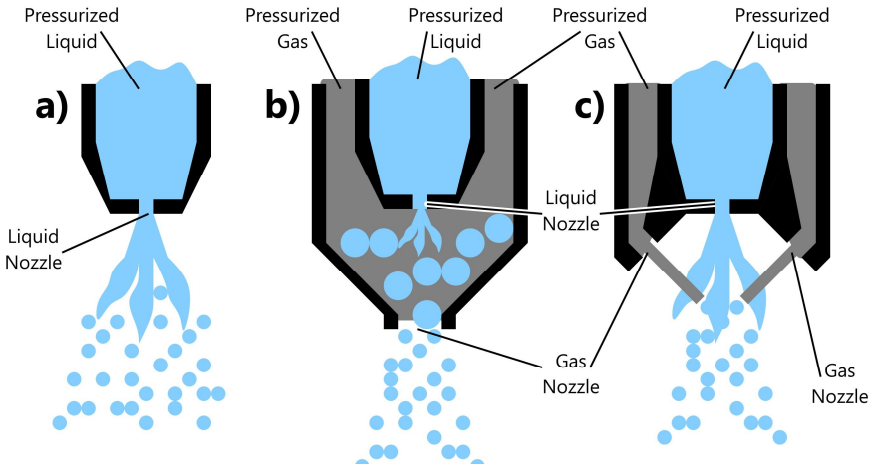

Figure 2.2. Diagram of examples of atomization techniques. The (a) liquid jet, (b) internal air assisted, and (c) external air assisted nebulizer are shown.

The jet instabilities atomizer is a combination of liquid jet atomizer with sonic or ultrasonic technology. The liquid jet is again atomized by the instabilities in the jet. However, the instabilities are due to the sonic vibrations induced in the jet. This allow for lower jet velocities because only the induced sonic vibrations cause atomization and the resulting droplet size is very narrow (Avvaru 2005).

The surface instabilities atomizer also uses sonic or ultrasonic methods of atomization. The sonic vibration disturbs the liquid surface. Given large enough amplitude of vibration the surface disturbance can result in liquid atomization. This method uses gas flow to transport the particles and the gas flow is independent from the material flow. The surface instabilities atomizer has a narrow droplet size distribution compared to those previously presented.

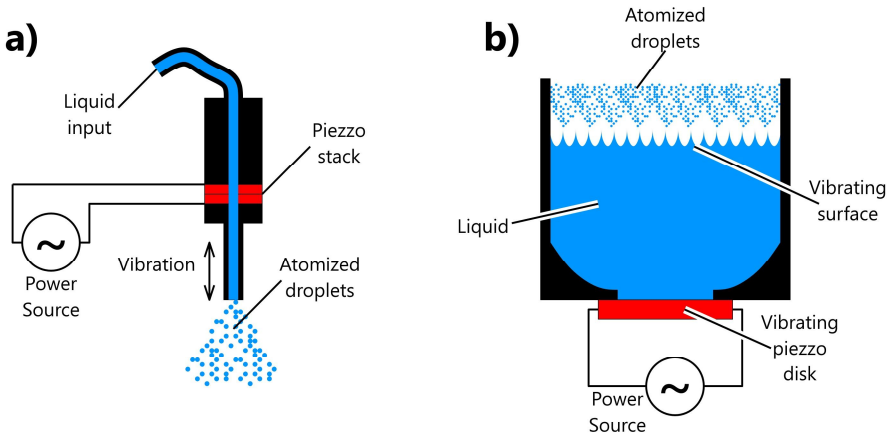

Figure 2.3. Diagram of examples of atomization techniques. The (a) jet instabilities and (b) surface instabilities atomizers are shown.

Electrostatic atomization uses intense electric field between the charged atomizer and surface to be coated. The charge transfers to the fluid and repulsive forces between the atomizer and the fluid tear the droplets from the atomizer and send them toward the work surface. The energy source for electrostatic atomization is the electric charge that

the fluid receives. The particle size with electrostatic atomization is a function of three main factors electric; field strength, liquid flow rate, and fluid properties (including its electrical properties). This method results in a narrow droplet size distribution.

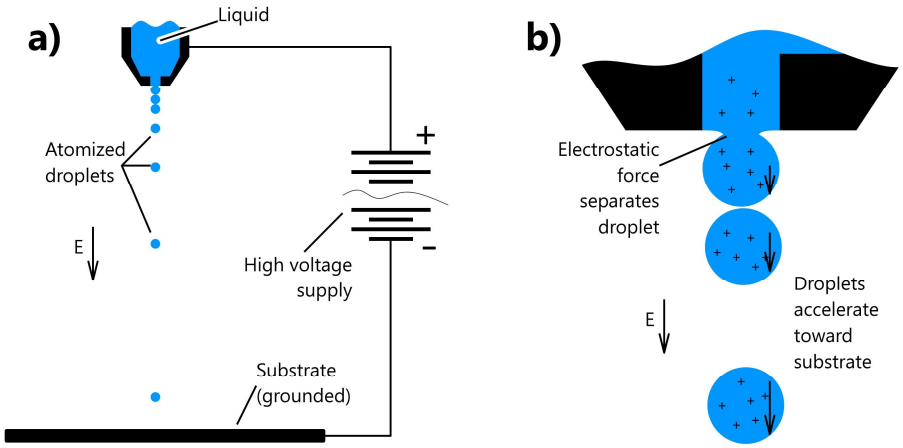

Figure 2.4. Electrostatic atomization technique. The (a) diagram of the apparatus and (b) the principle of the drop formation.

2.3. Spray Pyrolysis Heat Sources

Spray pyrolysis depends on heating to achieve its chemical decomposition. There are many techniques of heating that can be utilized in spray pyrolysis. Some of the common techniques include the hot surface (Mooney 1982), column oven (Messing 1993), laser-induced (Dedigamuwa 2009), flame heating (Madler 2002, Sheen 2009), and plasma heating (Hoder 2005, Gell 2007, Jia 2009) as shown in Figure 2.5 and 2.6. The choice of the technique utilized strongly depends on the particle's desired physical properties, chemistry and desired deposition rate. The choice of the heating technique will dictate the resulting process temperature and the time that the droplet/particle is being heated.

In hot surface pyrolysis processes, the atomized precursor is sprayed onto a hot surface. The pyrolysis occurs upon contact with the hot surface (Figure 2.5a). Because the liquid precursor is allowed to contact the surface, the coating is usually a film made up of platelets/splats. This process does not result in nano-particles, but allows for easy process temperature adjustment.

The oven spray pyrolysis process uses one or more heating columns. The atomized droplets are moved through a hot area created by the oven where the pyrolysis occurs (Figure 2.5b). The number and length of the ovens depends on desired process temperature and required reaction time. In this method, both temperature and pyrolysis time can be adjusted.

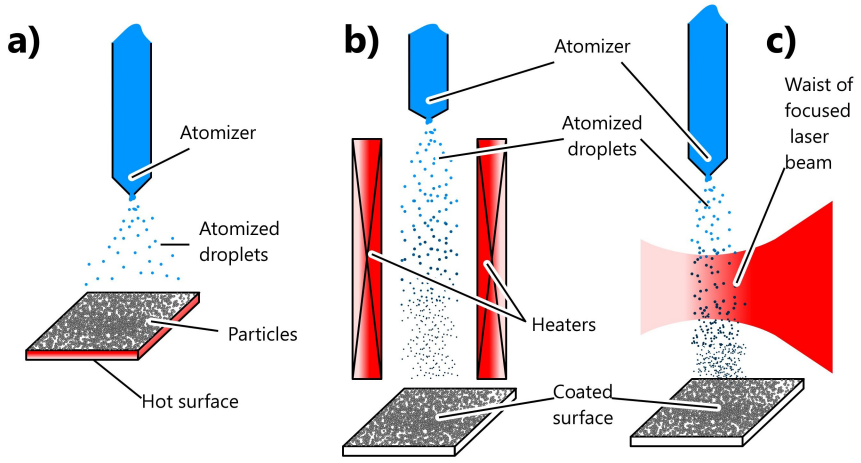

Figure 2.5. Selected pyrolysis processes. The (a) hot surface pyrolysis, (b) oven pyrolysis, and (c) laser assisted pyrolysis processes are shown.

In laser-assisted spray pyrolysis, a focused laser beam accomplished the heating. The atomized precursor is directed through the beam waist of focused laser beam (Figure 2.5c). Often the carrier gas is chosen to absorb the laser light creating a hot zone. The reaction occurs within the hot zone and the reaction temperature can be adjusted by regulating the power of the laser beam or change in material flow rate.

Flame spray pyrolysis uses the heat generated by burning a fuel to promote pyrolysis of the precursor droplets. A diagram of one arrangement of this technique is presented in Figure 2.6a. The precursor carried by the fuel (gas) flow mixes with an oxidizer at the nozzle tip. The ignited flame supplies heat to promote reaction. The processed particles are collected on the sample's surface. The process temperature can be changed by using different fuels and oxidizers, changing fuel to oxidizer ratio, and their flow rates. In addition, contact time with precursor droplet can be adjusted in this technique.

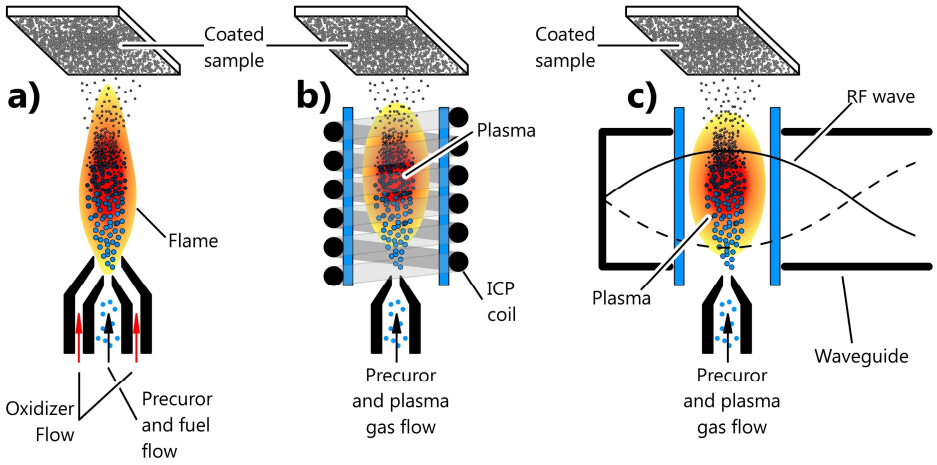

Figure 2.6. Plasma spray pyrolysis processes. The (a) flame, (b) ICP plasma, and (c) microwave plasma assisted spray pyrolysis systems are shown.

The flame in the previous technique can be replaced with an induction-coupled plasma (ICP) or microwave induced plasma. Plasma heating can reach very high temperatures without the need for a fuel. Plasma gasses can be reactive or inert depending on the needs of the particular deposition process. In these techniques, the temperature of the hot zone can be adjusted by changing the plasma operation parameters. The droplet/particle contact time with the plasma can be adjusted in the ICP arrangement

by changing the RF coil and reaction tube length. The waveguide dimensions limit the microwave plasma size.

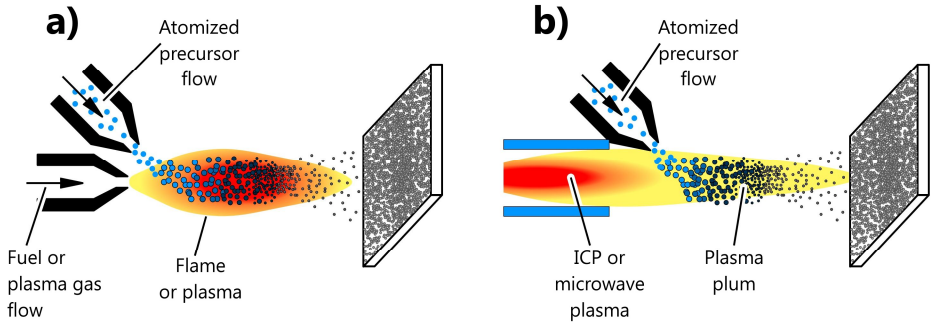

Figure 2.7. Material side injection technique. The material can be injected into (a) the plasma or (b) the plasma tail.

The material flow presented in Figures 2.5 and 2.6 is the same as fuel or plasma gas. However, the material and fuel for plasma gas flow can be separated. The side flow pattern shown in Figure 2.7a is often utilized (Gell 2007). This technique allows injecting the material at different parts of the plasma: material can be injected to the plasma itself or into the plasma tail.

By injecting the material into different parts of the plasma, the temperature and precursor/particle contact time with the plasma can be adjusted.

2.4. Chapter Summary

Spray pyrolysis is often utilized for synthesis of fine and ultrafine particles. A large selection of atomization, heating, and material injection techniques allows one to tailor spray pyrolysis to a specific application. Proper choice of the spray pyrolysis technique utilized one must consider the desired temperature, time needed to complete reactions, and the chemistry of the deposited material.

CHAPTER 3. Microwave Assisted Spray Deposition System Design

The Microwave Plasma Assisted Spray Deposition (MPASD) system was designed at the Laboratory for Advanced Materials Science and Technology (LAMSAT). The main advantage of the MPASD was its capability for depositing nano-sized particles that were surfactant free, needed no further annealing, and could be deposited in the required final crystal form on surfaces that are sensitive to high temperatures.

The MPASD system was composed of five sub-systems: microwave power delivery, material delivery, deposition chamber, vacuum pump, and control sub-systems. Figure 3.1 presents a diagram showing the key components and important electrical, gas, vacuum, and water connections.

The role of the microwave power delivery sub-system was to produce a high electric field localized within a plasma tube. The material delivery sub-system supplied metered amounts of process gas and the atomized precursor. The deposition chamber was used to create a controlled deposition environment and to enclose the sample mounting assembly. The vacuum sub-system created a stable and precise process pressure. The automated control helps to control and monitor the process variables, and record experimental data and process parameters. The control software was customized to accommodate many experiment scenarios

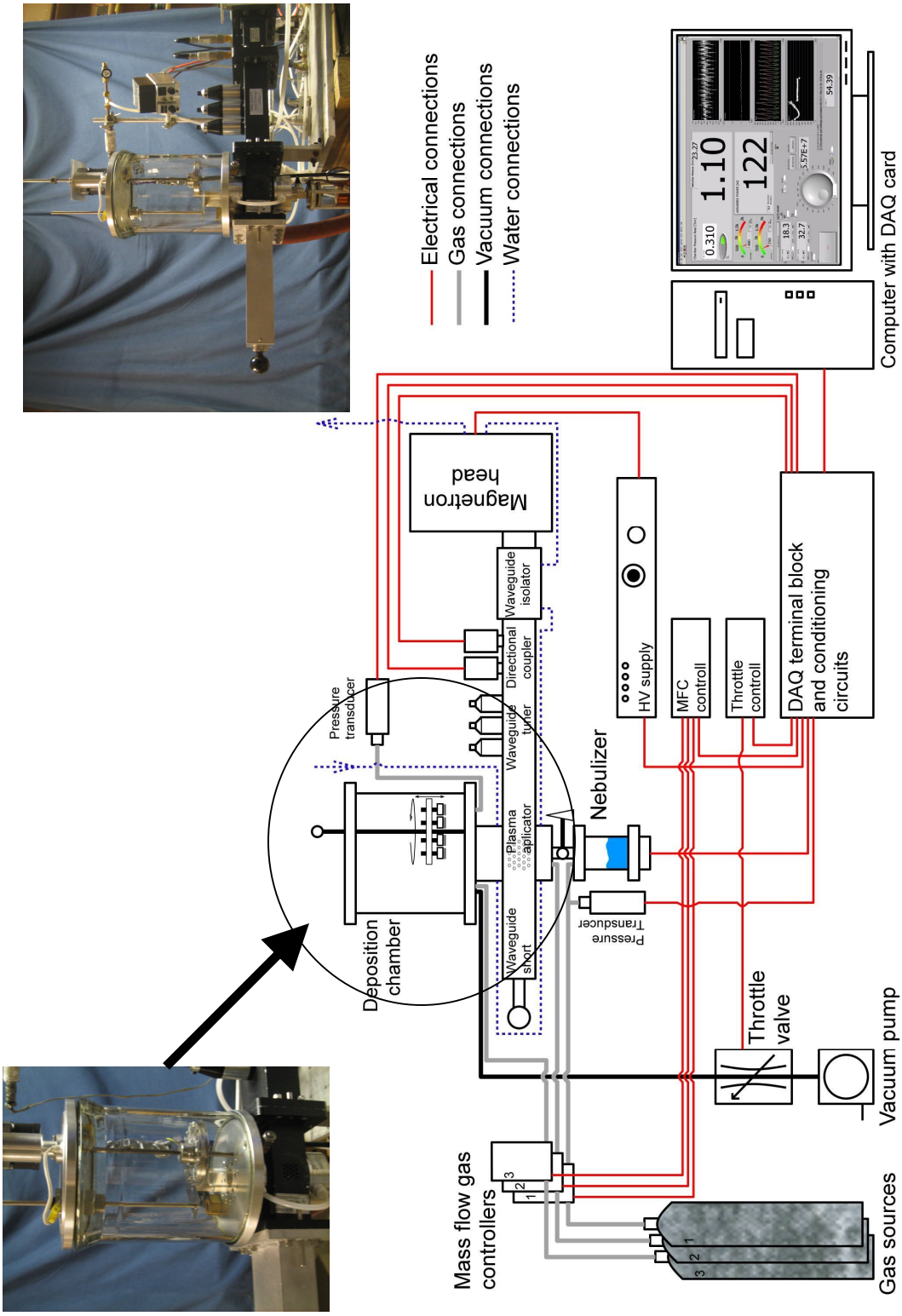

Figure 3.1. The Microwave Plasma Assisted Spray Pyrolysis (MPASD) system component diagram.

The MPASD system presented was successfully utilized to produce Eu doped Y_2O_3 particles with a diameter of 100nm. The results of this application are presented in Chapter 5 of this manuscript.

3.1. Microwave Power Delivery Subsystem.

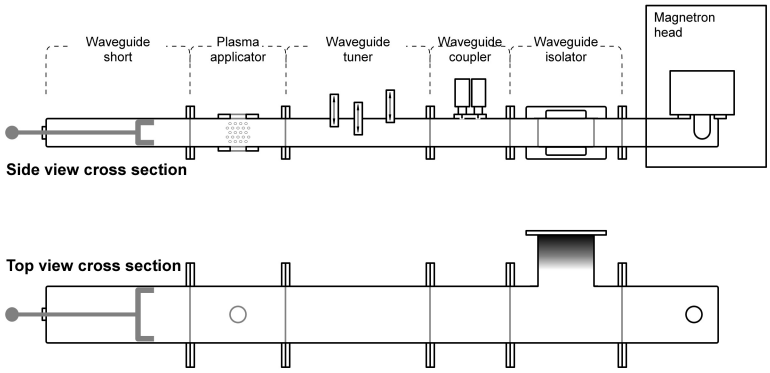

Figure 3.2. Microwave power delivery subsystem diagram.

The MPASD system uses a microwave power delivery sub-system to deliver microwave power to the plasma discharge zone. This subsystem was constructed using standard WR340 size waveguide components designed to work at a 2.45 GHz frequency in TE_{01} mode.

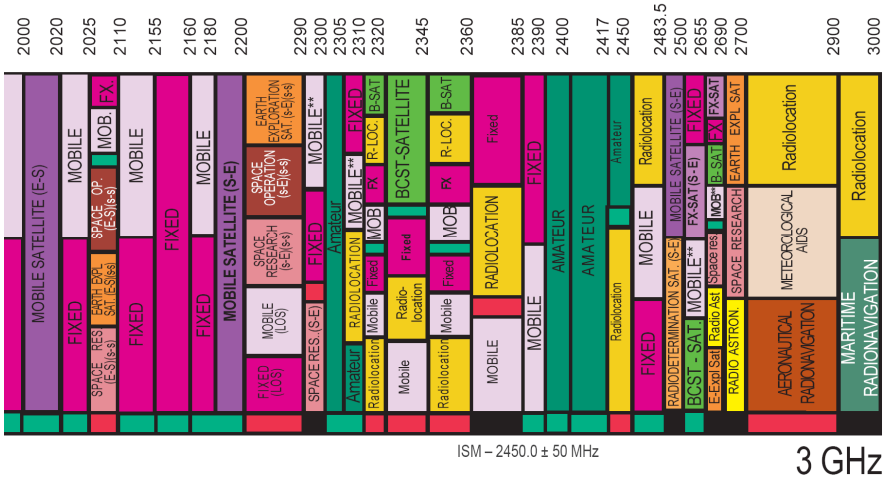

Figure 3.3. Selection of the United States radio spectrum frequency allocations chart (year 2003). (US dept of commerce)

Component availability and governmental regulations limit the choice of system operating frequency to the 2.45 GHz. The radio frequency spectrum is strictly regulated to avoid interference between users of the busy radio frequency (RF) spectrum (Figure 3.3). The RF spectrum allocated for industrial, scientific, and medical (ISM) applications use frequency bands ranging from 6.78 MHz to 245 GHz. The common ISM bands are listed in Table 3.1.

Table 3.1. The commonly used ISM bands of radio frequency spectrum.

Frequency range [Hz]	Center frequency [Hz]	Availability
6.765–6.795 MHz	6.780 MHz	Subject to local acceptance
13.553–13.567 MHz	13.560 MHz	
26.957–27.283 MHz	27.120 MHz	
40.66–40.70 MHz	40.68 MHz	
433.05–434.79 MHz	433.92 MHz	
902–928 MHz	915 MHz	Region 2 only (includes US)
2.400–2.500 GHz	2.450 GHz	
5.725–5.875 GHz	5.800 GHz	
24–24.25 GHz	24.125 GHz	
61–61.5 GHz	61.25 GHz	Subject to local acceptance
122–123 GHz	122.5 GHz	Subject to local acceptance
244–246 GHz	245 GHz	Subject to local acceptance

The most common “microwave heating” frequencies used commercially are the 915 MHz, 2.45 GHz, and the 5.8 GHz bands. Operation at these frequencies was desired since the availability off-the-shelf components speeds up the designing and prototyping of the system. The choice of the 2.45 GHz over the 915 MHz and 5.8 GHz was dictated by the overall system size and cost. The waveguide system operating at 915 MHz would require bulky WR975 (9.75 in. by 4.875 in. rectangular cross-section) or WR770 (7.7 in. by 3.85 in. cross-section). On the other hand, the system operating at 5.8 GHz would require small WR159 (1.590 in. by 0.795 in. rectangular cross-section) waveguide, with

higher components cost than for systems operating at 2.45 GHz. The 2.45 GHz system can use convenient sized WR340 waveguide (3.4 in. by 1.7 in. cross-section) and the component cost is lower than the other systems. The 2.45 GHz band is used in common household microwave ovens. In fact, very early designs leading up to MPASD system utilized common household microwave oven components.

3.11. Waveguide Theory

For a rectangular waveguide propagating a TE wave in the z-direction the propagation is:

$$E_y = i\frac{\omega \cdot a}{\pi \cdot c} B_0 \sin\left(\frac{\pi \cdot x}{a}\right) \cdot e^{i\alpha \cdot z - i\omega \cdot t} \tag{3.1}$$

The propagation coefficient α depends on free space and critical wavelength, and

$$\alpha = \frac{2\pi}{\lambda_c}\sqrt{1-\left(\frac{\lambda_c}{\lambda_0}\right)^2} \ . \tag{3.2}$$

For operation wavelengths longer than the critical wavelength, the propagation coefficient is a purely imaginary number and the resulting wave is attenuated as it propagates (evanescent wave). On the other hand, for wavelengths shorter than the critical wavelength, the propagation coefficient is a real number and as a result, the wave freely propagates through the waveguide.

For the TE_{01} mode of propagation, the electric field within a rectangular waveguide that depends on the power level and the time averaged electric field strength is given by (Metaxas 1988).

$$E_{TE01} = \sqrt{4 \cdot P \frac{\lambda_g}{\lambda_0'} \frac{1}{a \cdot b}\sqrt{\frac{\mu_a}{\varepsilon_a}}} \ . \tag{3.3}$$

Due to the propagation path of electromagnetic wave within a rectangular waveguide (Figure 3.4) the waveguide wavelength λ_g is different from the free space wavelength λ_0. The waveguide wavelength depends on free space wavelength and waveguide critical wavelength (Metaxas 1988).

$$\lambda_g = \frac{\lambda_0'}{\sqrt{1-\left(\frac{\lambda_0'}{\lambda_c}\right)^2}} \tag{3.4}$$

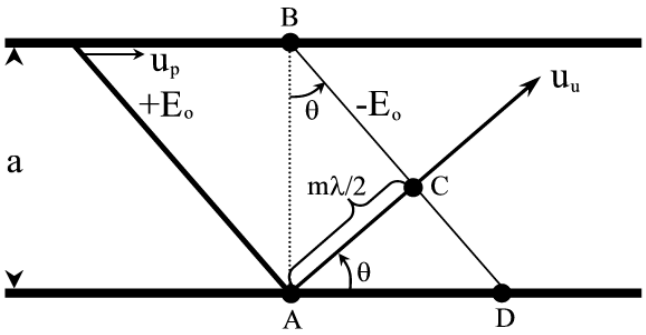

Figure 3.4. Wave propagating in a rectangular waveguide (TE_{01} mode). The relation between the free space propagation and waveguide propagation is shown.

The critical wavelength λ_c for a rectangular waveguide depends on its dimensions. For the $TE_{m,n}$ mode the critical wavelength is

$$\lambda_c = \frac{2}{\sqrt{\left(\frac{m}{a}\right)^2+\left(\frac{n}{b}\right)^2}} \quad (a > b \text{ and } TE_{m,n} \text{ mode}). \tag{3.5}$$

The above equations allow calculation of the electric field strength of a free running wave in a rectangular waveguide.

3.1.2. Microwave Power Delivery Subsystem Components

The microwave power delivery sub-system utilized a waveguide terminated magnetron head with power supply, waveguide isolator, waveguide directional coupler,

waveguide three stub tuner, waveguide plasma applicator, and waveguide adjustable short to create a standing EM wave of controllable position and strength. The magnetron head utilized a waveguide with one end closed and an additional opening in the broad wall. This additional opening allowed the magnetron antenna to be placed inside the waveguide cavity. The location of the antenna is usually $\frac{\lambda_g}{4}$ from the back wall of the waveguide. This location allows for the best coupling of the energy between the antenna and the waveguide.

Table 3.2. List of major components of microwave power delivery subsystem of MPASD system

PN:	Manufacturer	Description	Comments
GA4005	GAE	Magnetron Head	1.8 kW
GA1107	GAE	Waveguide Isolator	
GA3106	GAE	Waveguide Directional Coupler	
GA1002	GAE	Waveguide Tuner	
GA6103	GAE	Waveguide Plasma Applicator	
GA1219	GAE	Waveguide Adjustable Short	
SM745G.1001	Alter	Magnetron Power Supply	2 kW

The magnetron head used in MPASD was model GA4005 from Gerling Applied Engineering utilizing the water-cooled magnetron (Panasonic model 2M137). The microwave head was capable of generating microwave radiation a frequency of 2.45 GHz at up to 1.8 kW of power. The microwave output used the WR340 waveguide with UG554 flange. The model GA4006 magnetron head required a minimum of 1 GPM of coolant flow.

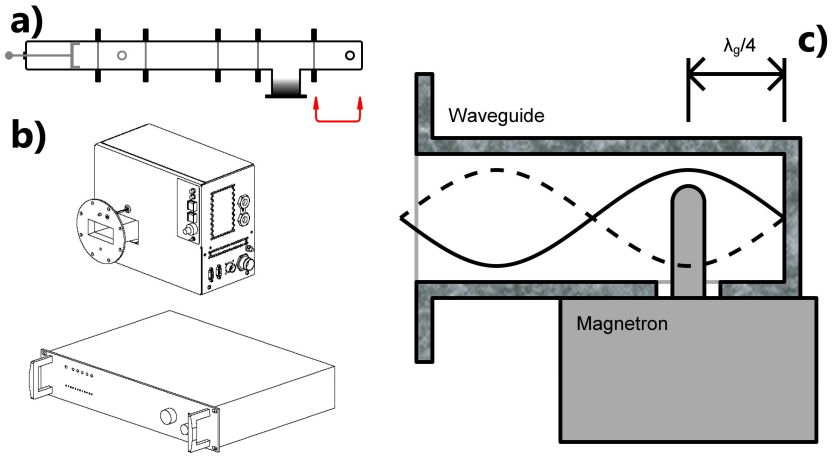

Figure 3.5. Magnetron head (a) location within MPASD, (b) picture of GA4002A magnetron head and SM745G power supply, and (c) operation diagram of magnetron launcher.

The magnetron head was powered using the high voltage power supply model SM745G made by Alter. This power supply was capable of generating a voltage of 4.6 kV and a current of up to 750 mA.

The controls built into the magnetron head were used during deposition to turn on and off the microwave generation and to adjust the microwave power level. The built-in safety interlock system prevented magnetron operation in case of coolant flow failure, magnetron over-temperature, and mechanical waveguide mounting failure.

The main role of the waveguide isolator in the MPASD was to protect the magnetron from damage due to the reverse microwave signal. The waveguide isolator is a device similar in design to the waveguide circulator in that both utilize the Faraday rotation of the EM wave within the ferromagnetic medium. In contrast from the circulator the isolator used in the MPASD had port #3 terminated with an absorbing media. In this configuration the forward wave entering port #1 (from magnetron head) was directed to port #2 (to plasma applicator). As the reflected wave entered the isolator at port #2 (from plasma applicator) it was redirected to port #3 where it was absorbed.

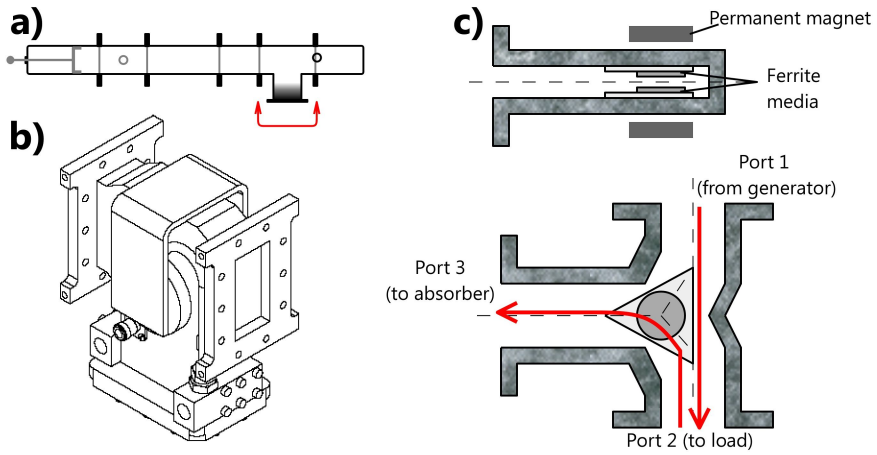

Figure 3.6. Waveguide isolator (a) location within MPASD, (b) picture of GA1107 waveguide isolator and (c) its operation diagram.

The waveguide isolator used in MPASD was the model GA1107 made by Gerling Applied Engineering. It is capable of operating at a frequency of 2.45 GHz and 6 kW of microwave power. The waveguide isolator utilized the WR340 waveguide with UG554 flanges. This waveguide isolator required a minimum of 0.9 GPM of coolant flow during operation.

The waveguide coupler is a waveguide device where a small portion of the microwave power was redirected from the waveguide into an external output. This task could be achieved by the use of an aperture array coupler, resistive loop coupler, and multi-probe reflectometer.

Because of the small size and low cost of application, the loop coupler was implemented. Other authors (Kulinski 1998, Mazur 2004) have treated the theory of operation of the waveguide loop coupler. The output signal of the loop coupler is rectified and the rectified voltage related to the power flow within the waveguide. The directivity of the loop coupler enabled separate measurement of the forward and reversed power.

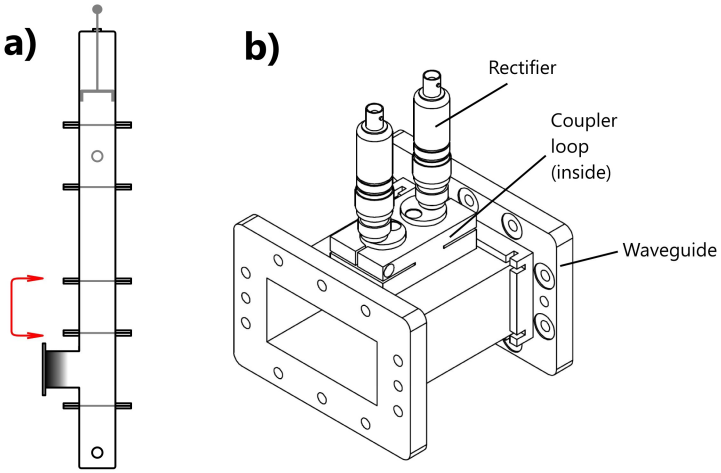

Figure 3.7. Waveguide directional coupler (a) location within MPASD and (b) picture of GA3106 dual directional waveguide coupler.

The waveguide coupler used in the MPASD was the model GA3106 made by Gerling Applied Engineering capable to operate at a frequency of 2.45 GHz. The directional coupler was matched with two detectors, and the set was calibrated for operation up to 2 kW of microwave power. The waveguide coupler utilized the WR340 waveguide with UG554 flanges. The directivity of the coupler was measured by the manufacturer to be 56 dB.

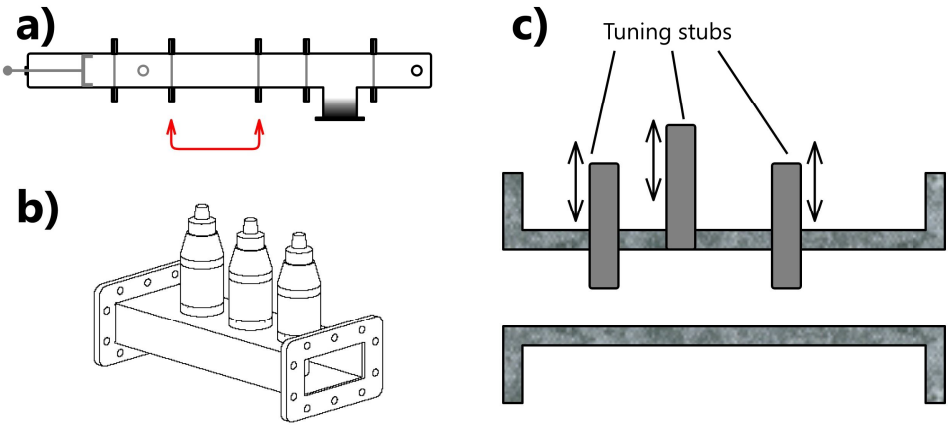

Figure 3.8. Waveguide three stub tuner (a) location within MPASD, (b) operation diagram, and (c) picture of GA1002 precision 3-stub tuner.

The waveguide system can be modeled using circuit theory. In this approach, each waveguide component is viewed as an equivalent R-L-G-C circuit (Figure 3.9) which the values depend, among other parameters, on geometry and dimensions of the waveguide.

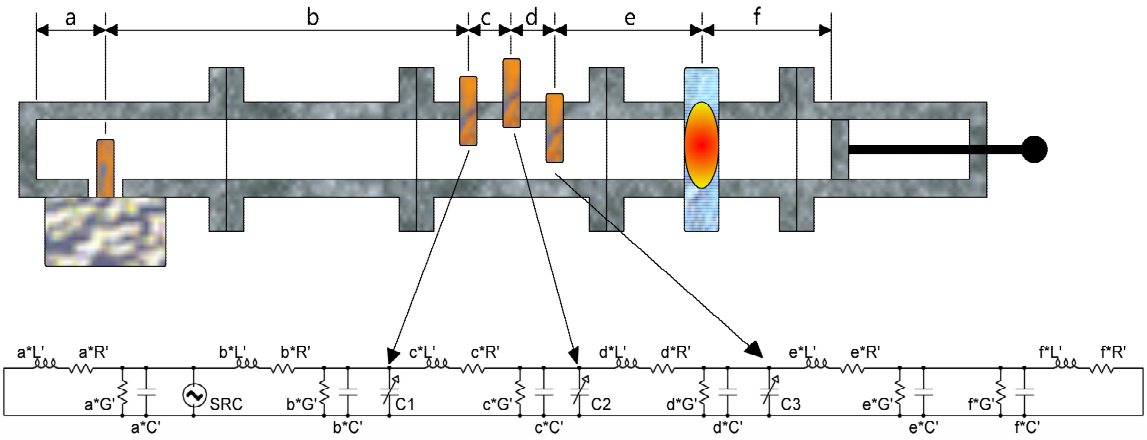

Figure 3.9. Example circuit model of waveguide components.

The role of three-stub waveguide tuner was to match the impendence of the plasma discharge to the impendence of the microwave source. The three metal stubs protruding through the broad wall of the waveguide had the protruding depths controlled. The metal stubs changed the impedance of the waveguide section and helped to reduce the reverse power within the waveguide by matching the load to the source impedance. Other authors (Griffin 1976, Muehe 1968) explain the theory and show experimental results for waveguide tuners

The waveguide tuner used in MPASD was the model GA1002 made by Gerling Applied Engineering capable to operate at frequency of 2.45 GHz and up to 6 kW of microwave power. The waveguide tuner utilized the WR340 waveguide with UG554 flanges.

The plasma applicator is a section of waveguide with openings in the wide side of the waveguide that allow placing the plasma discharge tube inside the waveguide.

Additional side view holes allow for optical diagnostic of the plasma. The size of the openings and their length are chosen to reduce the microwave leakage by taking advantage of the attenuation of the wave while operating below the cut-off frequency for the opening.

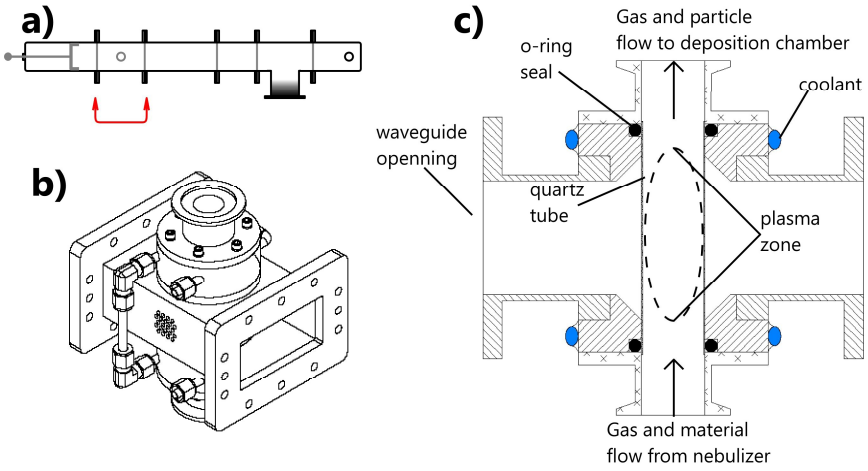

Figure 3.10. Plasma applicator (a) location within MPASD, (b) picture of GA6103 downstream plasma applicator, and (c) its detailed cross section.

The waveguide plasma applicator used in the MPASD was the model GA6103 made by Gerling Applied Engineering capable of operating at radio frequency of 2.45 GHz and up to 6 kW of microwave power. This waveguide plasma applicator utilized the WR340 waveguide with UG554 flanges. The plasma applicator was modified to improve the MPASD process. The original plasma applicator designed for generation of downstream plasma for semiconductor applications was found to be inadequate for use in MPASD process. The discharge chamber of the original applicator had a shape that allowed for better localization of the discharge for downstream plasma applications. However, in this design the discharge was difficult to maintain at larger process pressures of MPASD, and the plasma had routinely melted the narrow discharge tube. The redesigned applicator had the plasma tube assembly changed to increase the electric field

strength and to use a larger diameter discharge tube (Figure 3.11a). This resulted in ease of plasma ignition and plasma and maintenance during deposition, and the tube melting incidents were reduced.

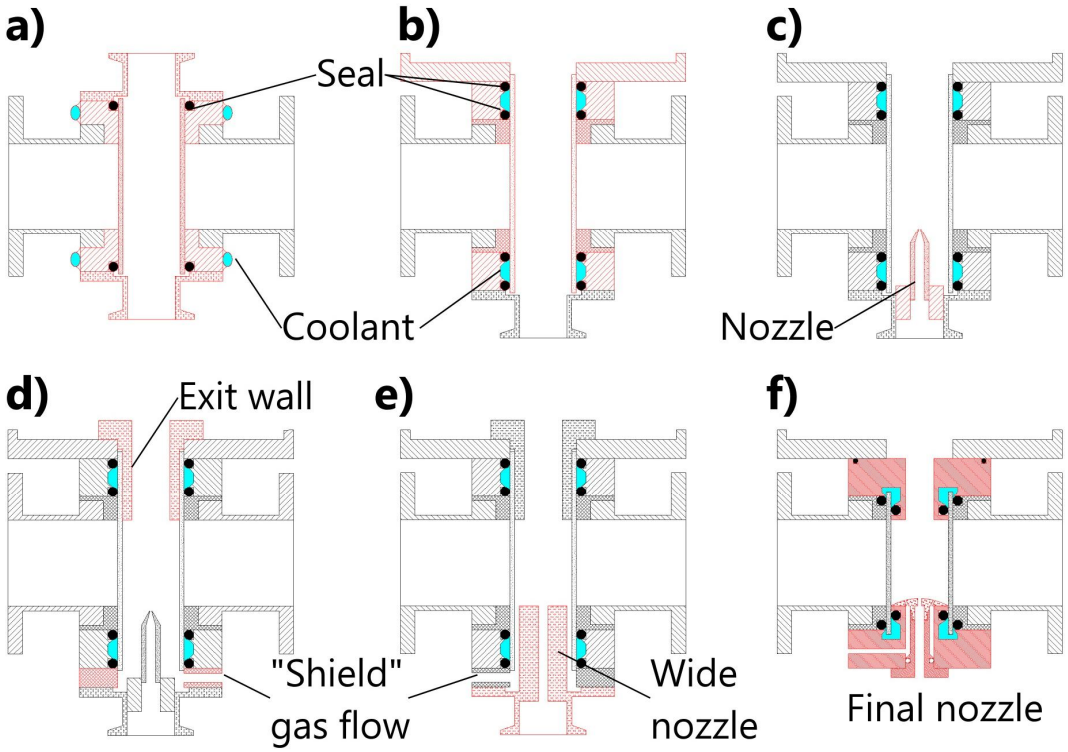

Figure 3.11. Plasma applicator redesign stages cross section diagram. Features marked red were new or redesigned from original. Seals are marked with solid black and coolant with light blue.

Plasma zone vacuum seals needed to be re-designed as the original seal design were inadequate. The original design utilized high temperature kalvarez o-ring seals, and the seals were indirectly cooled by water-cooling of the metal assembly. The exotic and expensive kalvarez orings are capable of operating at higher temperatures than the common buna of viton elastomeric o-rings. However, the original design did not efficiently cool the seals and seal failure occurred within few minutes of operation.

To reduce the seal failure rate an improved seal cooling scheme was introduced. The coolant was allowed to be in contact with the seal and the plasma tube. This

approach reduced the seal failure rate and did allow the use of less expensive buna and viton seals. Although this redesign (Figure 3.11b) increased the lifetime of the seal, it did not protect the seals sufficiently, as damage due to overheating and UV radiation occurred. The second redesign of the seal improved the reliability of the seal by allowing for direct contact of the coolant with the seals and the plasma tube, as well as shielding them from the plasma radiation (Figure 3.11d and e).

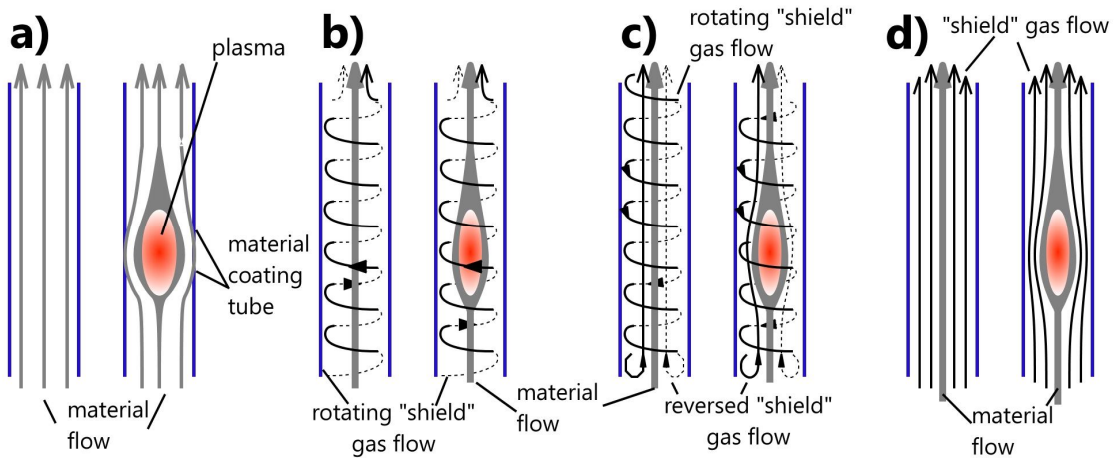

Figure 3.12. Different flow patterns possible in plasma zone. Material flow is marked gray and gas flow is marked black.

One reason for plasma tube and seal failure was overheating. This problem was reduced by changing the gas flow pattern within the plasma tube. The original flow of the plasma applicator was inappropriate for the MPASD process and required redesign. The wide straight through flow pattern of the GA6103 created significant plasma tube coating, material flow within the tube was unpredictable, and the plasma tube habitually overheated due to coating of the tube. These shortcomings of the plasma applicator were addressed in the plasma applicator redesigns. Several methods that included the material flow nozzle, sheath gas flow, reverse vortex flow techniques were experimented with to determine the optimal design (Figure 3.12). Although the material flow nozzle (Figure 3.11 c and d) improved the results, the tube coating was still a significant issue, and the

flow pattern, although better, was unsatisfactory. The plasma tube overheating due to material buildup persisted. The forward vortex (Figure 3.12b) and reverse vortex flow pattern (Figure 3.12c) both resulted in satisfactory flow pattern control: overheating of the plasma tube was reduced significantly and the tube coating was reduced. However, high flow of the gas was needed for the vortex to develop. This resulted in short contact time between the plasma and the material to be processed. The final design utilized the material flow nozzle with gas forward sheath flow (Figure 3.12d). This design allowed for lower gas flow rates and still maintained good plasma control and predictable material flow pattern.

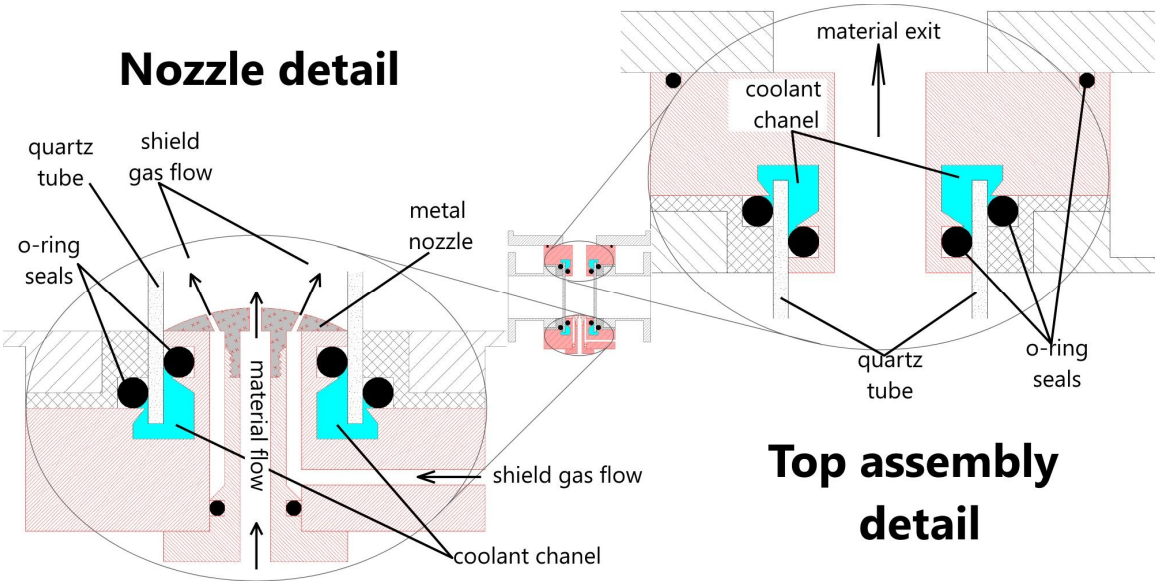

Figure 3.13. Plasma applicator final design.

The material flow pattern was improved by introduction of the material nozzle. The first and simplest material nozzle was made of a glass tube (Figure 3.11c) was found to be inappropriate for the MPASD. The high temperatures of the plasma melted the nozzle tip. The improved flat top metal nozzle (Figure 3.11e) helped to remove the heat from the nozzle tip, but also created instability within the plasma. Because this nozzle was made of metal it also most likely increased the electric field within the plasma zone,

but its flat top design created a situation where the plasma would “dance” around the center of material flow. These instabilities were eliminated using a dome shaped plasma nozzle. The dome design (Figure 3.11f and 3.13) localized the plasma discharge to the center of the plasma tube by increasing the electric field in the center of the nozzle (the top of the dome) as opposed to the edges.The final design of the plasma applicator detail is presented in Figure 3.13. The experiments described in Chapter 4 and 5 utilized this design.

An adjustable waveguide short was required to localize the standing wave in order to create an anti-node within the plasma cavity. The electric field at the movable wall was zero this locates the node of standing wave was wall. Therefore, the anti-nodes were located at $\lambda_g\left(\frac{1}{4}+n\frac{1}{2}\right)$ away from the shorting wall. As the waveguide short was moved, one of the anti-nodes could be located within the plasma tube.

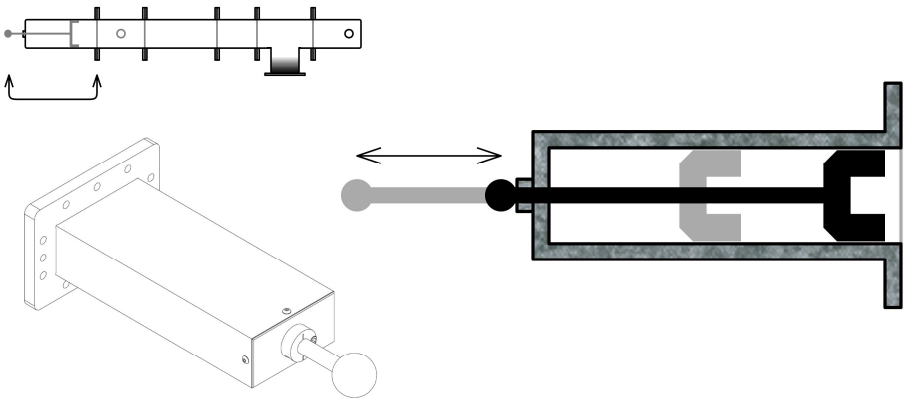

Figure 3.14. Adjustable waveguide short (a) location within MPASD, (b) operation diagram, and (c) picture of GA1219A basic sliding short circuit.

The adjustable waveguide short used in MPASD was the model GA1219 made by Gerling Applied Engineering capable to operate at frequency of 2.45GHz and up to 6kW

of microwave power. This waveguide short utilized the WR340 waveguide with UG554 flanges.

3.2. Material Delivery Sub-system

The role of the material delivery sub-system of the MPASD system was to supply the atomized precursor and process gases to the plasma applicator. The main parts of the sub-system were the precursor atomizer and gas metering controllers.

Table 3.3. Major components list of the material delivery subsystem of the MPASD system.

PN:	Manufacturer	Description	Comments
UFC-1000	MKS	Mass Flow Controller	50sccm N_2
UFC-81000	MKS	Mass Flow Controller	1slm NH_3
	Stec	Mass Flow Controller	
241T	Sonaer	Ultrasonic Nebulizer	

3.2.1 Precursor Atomizer

The size and size distribution of the precursor droplet used in MPASD directly affected the size and size distribution of the particles created. Proper choice of atomization technique of precursor solution was critical. The choice was made after considering the different atomizer techniques listed in Table 2.1.

A very narrow droplet size distribution of jet instability or electrostatic spray is desired for MPASD technique. However, because of the ease of application, the ultrasonic nebulizer was chosen. The ultrasonic nebulizer that was used is an example of the surface instability atomizer. The narrow distribution of the ultrasonic nebulizer, low

fluid flow rate, and low initial kinetic energy of the droplet is appropriate for application in MPASD.

The dynamic instability of surface submitted to oscillations at high frequency was used to obtain atomization. One method to create surface vibrations utilizes a vibrating piezo-crystal driven by alternating current (Figure 3.5). The vibrating crystal plate created disturbances on the surface of the liquid that resulted in liquid atomization.

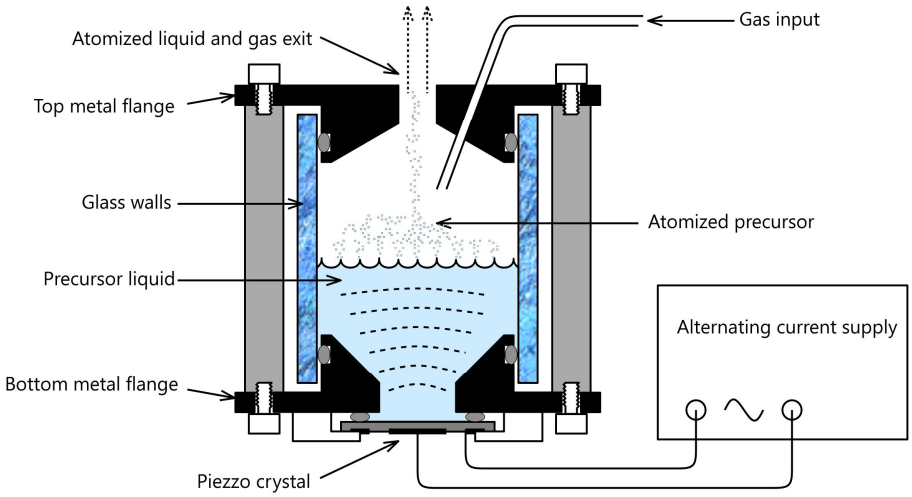

Figure 3.15. The diagram of ultrasonic atomizer utilized in MPASD system.

Given sufficient energy of the oscillations, the surface instabilities can result in formation of droplets. The droplet size distribution is narrow and the size depends on the oscillation frequency. According to Kelvin's expression (Lacas 1994) the disturbance wavelength relates to surface tension σ, liquid density ρ and oscillation frequency f by

$$\lambda^3 = 2\pi \cdot \frac{\sigma}{\rho \cdot \left(\frac{f}{2}\right)^2}. \tag{3.6}$$

Mizutani (1972) has shown that the droplet diameter was directly proportional to disturbance wavelength. Then

$$d^3 = k^3 \lambda^3 = 2\pi \cdot k^3 \frac{\sigma}{\rho \cdot \left(\frac{f}{2}\right)^2} \tag{3.7}$$

Mizutani showed that $k^3 \approx 0.53$ for Sauter's mean diameter then

$$d = 0.53 \cdot \sqrt[3]{\frac{8\pi \cdot \sigma}{\rho \cdot f^2}} = 1.55 \cdot \sqrt[3]{\frac{\sigma}{\rho \cdot f^2}} \tag{3.8}$$

For the nebulizer used in MPASD (Soaner model 241) the manufacturer indicated that the volume mean diameter of atomized droplets was (sonozap.com)

$$d = 0.73 \cdot \sqrt[3]{\frac{\sigma}{\rho \cdot f^2}} \tag{3.9}$$

The difference between equations 3.8 and 3.9 was due to different statistics used to calculate the average diameter.

Now suppose a solution droplet created by the nebulizer have its solvent removed and undergoes pyrolysis. The remaining solute will create a particle. The final diameter of such a particle relates to the diameter of the initial droplet by

$$d^3_{particle} = k \cdot d^3_{solution}. \tag{3.10}$$

Here the constant k directly depends on molar concentration of the precursor solution $\hat{c}_{sol}$, the molar mass of particle $M_{particle}$, density of particle $\rho_{particle}$, and molar ratio κ. The factor κ is the molar ratio of product to reagent in pyrolysis reaction. Then

$$d^3_{particle} = \left(\frac{\hat{c}_{solution} \cdot M_{particle} \cdot \kappa}{\rho_{particle}} \right) \cdot d^3_{solution} \tag{3.11}$$

and combining equations 3.9 and 3.11 results in

$$d_{particle} = 0.73 \cdot \sqrt[3]{\frac{\sigma}{\rho \cdot f^2} \frac{\hat{c}_{solution} \cdot M_{particle} \cdot \kappa}{\rho_{particle}}} \tag{3.12}$$

for a particle mean volume diameter.

The model 241T nebulizer utilized in MPASD system was operated at a frequency of 2.4 MHz. The precursor used during the deposition process used water as a solvent. Assuming that the small concentrations of the material in the solvent did not change the properties of the precursor from the solvent, surface tension, and density, then for water ($\sigma = 0.0728 \frac{N}{m}$ and $\rho = 1000 \frac{kg}{m^3}$) the atomized precursor mean volume diameter is $d_{solution} = 1.7\,\mu m$. Then the mean volume diameter of particle is

$$d_{particle} = \left(0.0120 \cdot \sqrt[3]{\frac{M_{particle} \cdot \kappa}{\rho_{particle}}} \right) \cdot \sqrt[3]{\hat{c}_{solution}} \,. \tag{3.13}$$

The cube root dependence of particle diameter on concentration requires that the solvent contamination needs to be considered when resulting particles are of nano-size. The contamination of precursor solvent is important issue for the small contamination of the precursor become much larger contamination of the resulting nano-particle.

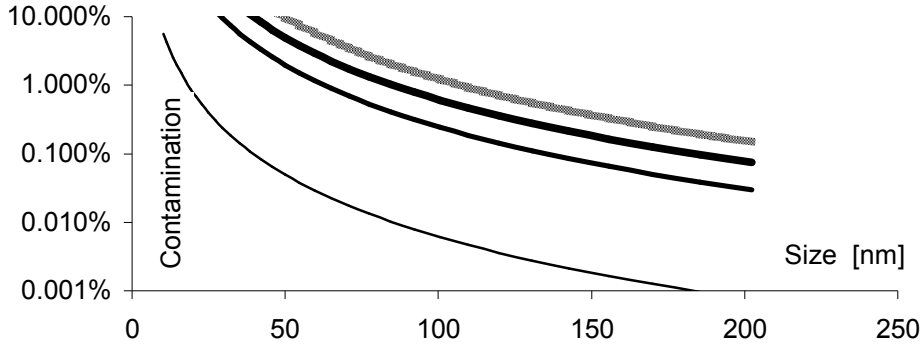

Figure 3.16. The effect of the precursor contaminate level on contaminate concentration within nanoparticle. The curves represent the contamination due to 0.01ppm, 0.4ppm, 1ppm, and 2ppm contaminated solvent if used to produce 100nm Y_2O_3 particles.

If depositions of nano-scale particles are desired then solvent quality plays a significant role as it is shown in Figure 3.16. Some of contaminates of the solvent might

incorporate into the particles resulting in unexpected or even undesired results. For example the reagent grade distilled water (Alpha Aesar PN:36645) can contain 0.01ppm of silicate, 0.01ppm of heavy metals, 0.04ppm chlorine, 0.4ppm NO, 1ppm PO, and 1ppm SO. The ultrapure spectrometric quality water (Alpha Aesar PN:19391) contains as much as 2ppm evaporation residue that includes 0.01ppm of heavy metals. This might result in over 1% contamination of the resulting 100 nm nano-particles of Y_2O_3 used in depositions presented in Section 5.2.

In order to reduce the solvent contamination effect on the resulting product, aside from using extremely pure solvents, the atomized droplet size would need to be decreased. This would allow using higher precursor concentrations and thus reducing the contaminant to solute ratio within each droplet. The practical method of reducing the droplet size requires nebulizer redesign. Changing the nebulizer operation frequency will allow reduction of the atomized droplet size. Atomized droplet size depends on the frequency as $d \sim f^{-\frac{2}{3}}$. In order to reduce the particle volume by a factor of 10 the frequency of the nebulizer operation needs to be increased by a factor of 3.16. This would decrease the contamination of the resulting coating by a factor of 10. Although high purity solvents are recommended for the MPASD process, the practical method of the contamination levels control in the nano-particle appears to be reduction of atomized droplet size by higher frequency nebulizer design.

3.2.2. Gas Mass Flow Controller

The precise control of the process gas mass flow is achieved by the use of mass flow controllers (MFC). The MFCs used in MPASD system utilize the commercially

available devices (UNIT models UFC-1000 and UFC-8100). The MFCs used have built in thermal flow sensor and electromagnetic (UNIT) or piezo-electric (STEC) flow-controlling valves.

The thermal flow sensor detects change in the thermal profile along the gas flow tube. Under a zero-flow condition the temperature profile will be symmetric on both sides of the heater (Figure 3.17a). During gas flow through the tube, disturbance of the temperature profile occurs. The temperature distribution is sensed by the thermistors mounted on each side of heating element. Thermisotors are connected as part of a Wheatstone bridge allowing measurement of the small voltage corresponding to a temperature difference. Therefore, the voltage difference relates to gas flow through the tube.

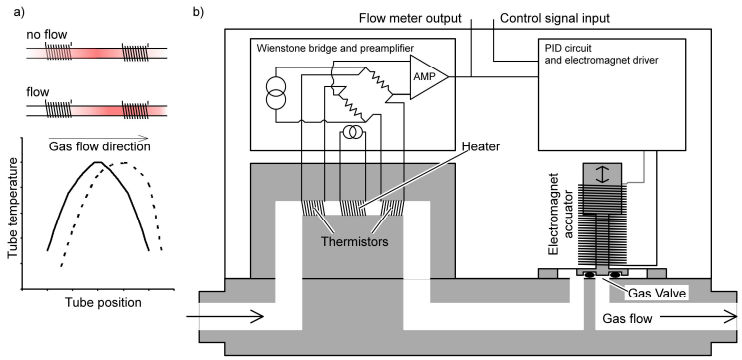

Figure 3.17. Basic operation of gas mass flow meter (a) and the diagram of typical gas mass flow controller.

The flow signal from the thermal flow sensor is compared to the flow control signal supplied from outside of the controller. Internal circuitry readjusts the gas valve position according to the difference signal between the gas flow measured and set value.

3.3. Deposition Chamber

As the processed material exited the plasma zone, it entered the deposition chamber where the material was deposited onto a substrate. The deposition chamber consisted of an 8 inch diameter aluminum base plate, cylindrical glass wall, the choice of various aluminum top plates, sample holder, deflection shield, and optional plasma tail directing tube.

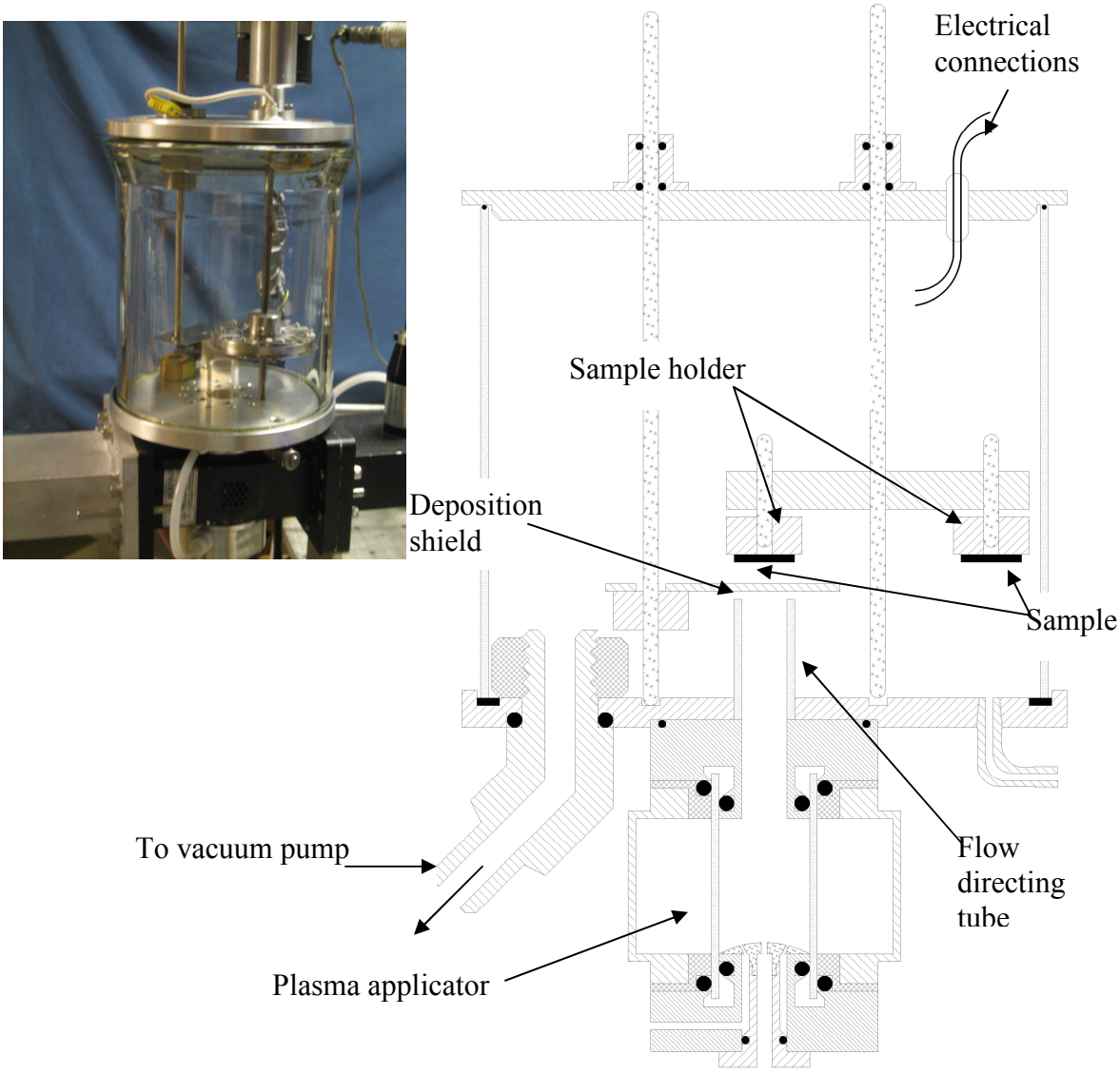

Figure 3.18. Picture and diagram of deposition chamber.

The base plate acted as a mechanical base for the vacuum chamber as well as the connection for gas, and vacuum lines. The base plate was mounted onto the plasma applicator's top water jacket that also acted as a heat sink for the chamber. The center opening of the base plate allowed for the gas flow directing tube to be installed. This improved the coating growth rate.

The cylindrical sidewall of the deposition chamber was made of Pyrex glass, and allowed for easy alignment of the sample before operation and visual diagnostics during operation of MPASD system. The vacuum seal was accomplished using the flat rubber gasket that makes the seal between the bottom plate and the chamber wall, and the o-ring seal that makes the seal between the cylindrical wall and top plate. The top plate is equipped with two mechanical feed-through that allowed manipulation of the sample holder by adjusting height and position of the depositing sample and operation of the deflection shield. The electric motor mounted on the top plate was utilized to rotate the multiple position sample holder which allowed deposition on several samples during one deposition rum. In addition, the electric feed-through in the top plate was used to connect probes located inside the chamber.

3.4. Vacuum Sub-System

As the material flows into the system the role of the vacuum sub-system was to remove the gasses from the system at a rate that will result in a controlled pressure within the deposition chamber. The vacuum subsystem utilized the dual stage rotary vacuum pump with a pumping speed of 70 cfm and capable of creating a vacuum level of 10^{-4} Torr.

The pressure control was achieved by utilizing a throttle valve located between the vacuum pump and the deposition chamber. The throttle valve was actuated by an electric motor controlled by an electronic controller.

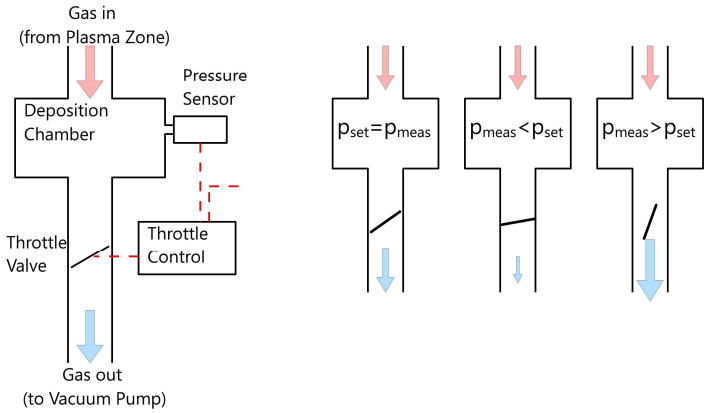

Figure 3.19. Operational diagram of vacuum sub-system. The different pressure conditions are shown.

The process pressure was measured by a silicon strain gauge pressure sensor. The throttle controller utilized a circuit that compares the set voltage representing the desired set pressure and the pressure sensor voltage representing the actual pressure. If the two were not at the desired balance, the internal circuit energized the throttle valve to open when the pressure is too high, or to close if the pressure was too low, as shown in Figure 3.19. The throttle control utilized a simple PID circuit that prevents control oscillations and improves the response of the system. The pressure set voltage was generated by the control and monitoring subsystem described later.

Table 3.4. List of major components of vacuum subsystem of MPASD system.

Model	Manufacturer	Description	Comments
2008A	Alcatel	Vacuum Pump	
253B-1-2CF-1	MKS	Throttle Valve	
152H-P0	MKS	Throttle Valve Control	
54-760-eng	Sensor Systems	Pressure Gauge	0-25 PSIa in, 1-5VDC out

3.5. Control and Monitoring Sub-System

The control and monitoring sub-system simplifies the MPASD deposition process by automatically monitoring and controlling some of the variables of the process. The deposition variables include microwave power, process pressure, precursor atomization rate, and process gas flow. In addition, this sub-system allows monitoring of the diagnostic temperature probe. This sub-system utilizes a computer based data acquisition card (DAQ) together with pressure, temperature, microwave power, and gas flow sensors and controllers.

Table 3.5. List of major components of control and monitoring subsystem of MPASD system.

PN	Manufacturer	Description	Comments
PCI-6221	National Instruments	DAQ card	
SCB-68	National Instruments	DAQ terminal block	
		Computer	Generic
	National Instruments	LabView 8.5	Software
	Power One	Power supply module	12V DC, Two needed
		PWM circuit	See Appendix A
		Diff amp circuit	See Appendix A

The heart of the control sub-system is the DAQ card controlled by the LabView software. The PCI-6221 DAQ card used is capable of measuring up to 16 voltage signals, generating 2 voltage signals, and 2 PWM digital pulse trains. The DAQ card measured the pressure sensor, temperature probe, microwave crystal rectifier voltage, and gas mass flow output voltage.

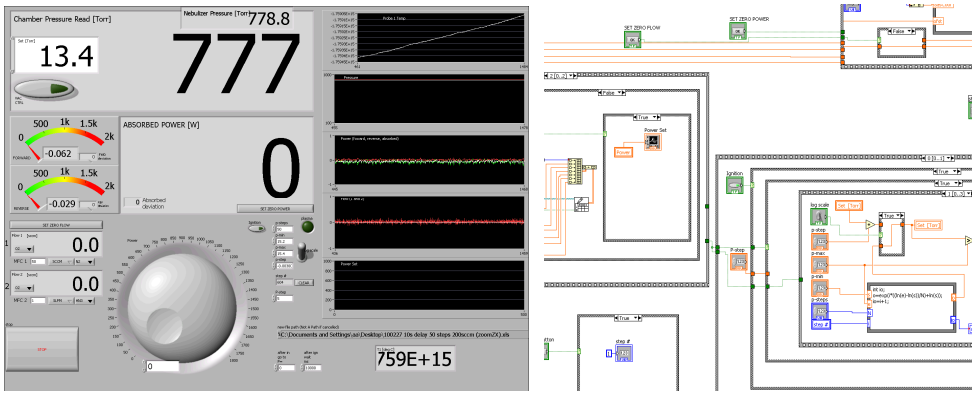

Figure 3.20. Front panel and program diagram (part) for MPASD control and monitoring program written in LabView.

The software interface recalculates the voltages into meaningful values representing the respective measurements that were accessed through the virtual control panel. The voltage output was utilized in the plasma ignition study (Section 4.3) to automatically vary the microwave power during the study. The PWM pulse train generated by the DAQ card was used to control the power of the nebulizer and in turn the rate of precursor atomization.

A differential amplifier circuit was used to eliminate common mode voltage of the temperature probes. The isolating circuit was used between the DAQ and the nebulizer allowing computer control of the nebulizer material atomization rate. The electrical diagram of the control and monitoring sub-system and schematics of the differential amplifier and the PWM circuit are presented in Appendix A.

3.6. Chapter Summary

The MPASD system utilizes microwave power to produce a thermal plasma. MPASD system utilizes rectangular waveguides to create a standing wave within the plasma applicator as described in Section 3.1.2. The process precursor was atomized using the nebulizer described in Section 3.2.1 and the material was heated in the plasma

applicator described in Section 3.1.2. The process gas was metered using the mass flow controller described in Section 3.2.2. The processed particles were collected onto a substrate located in deposition chamber described in Section 3.3. The vacuum system presented in Section 3.4 removed the process gas from vacuum chamber and controled the process pressure. The automatization sub-system utilized computer controls to ease the deposition process and monitor the multitude of process parameters (Section 3.5).

CHAPTER 4. Microwave Plasma Assisted Spray Deposition System Characterization.

The characterization of the MPASD system is presented in this chapter. The MPASD process relies on the plasma thermal heating of the material. The initial estimate of the plasma temperature, plasma emission spectroscopy study, as well as the plasma ignition study is presented in this chapter. In addition, the results of the precursor atomization rate study are presented.

4.1. Plasma Temperature Model

During the steady state of the MPASD operation, the microwave energy absorbed by the plasma gases could be estimated by adding the energy lost due to radiation, conduction, and mass transfer. Assuming thermal equilibrium within the plasma zone of MPASD process then the plasma temperature can be estimated using simple calorimetric and radiative relations. Since most of the materials grown by the MPASD system are oxides, the plasma temperature estimate was calculated for oxygen as carrier gas and water as a precursor solvent.

In the first approximation, it was assumed that the radiation and the conduction are not significant. Therefore, during steady state operation of the MPASD the power

absorbed by the plasma is equal to the thermal power flowing out due to the hot gas and material exiting the plasma zone. The power balance can be written as:

$$P_{absorbed} = P_{mass-transfer} = P_{mass-transfer-gas} + P_{mass-transfer-precursor} \tag{4.1}$$

The power needed to increase the temperature for a gas flow rate f_{mass} is

$$P_{mass-transfer-gas} = f_{mass} c_{gas} \Delta T \tag{4.2}$$

The heat capacity of c_{gas} can be treated as constant for Argon gas ($c_{p,Ar} = \frac{3}{2} \cdot R$) but it is a function of temperature for molecular oxygen. The heat capacity for oxygen has four main contributions: translational, rotational, vibrational and electronic modes. In the most general case, the heat capacity for molecular oxygen can be then written as sum of heat capacities due to translational, rotational, vibrational and electronic modes.

$$c_{v,o_2} = \left[\frac{3}{2}\left(\frac{\Theta_1}{T}\right)^2 e^{\frac{\Theta_1}{T}} + \frac{2}{2}\left(\frac{\Theta_2}{T}\right)^2 e^{\frac{\Theta_2}{T}} + \frac{1}{2}\left(\frac{\Theta_3}{T}\right)^2 e^{\frac{\Theta_3}{T}} + \sum_i \frac{1}{2}\left(\frac{\Theta_i}{T}\right)^2 e^{\frac{\Theta_i}{T}} \right] \cdot R \tag{4.3}$$

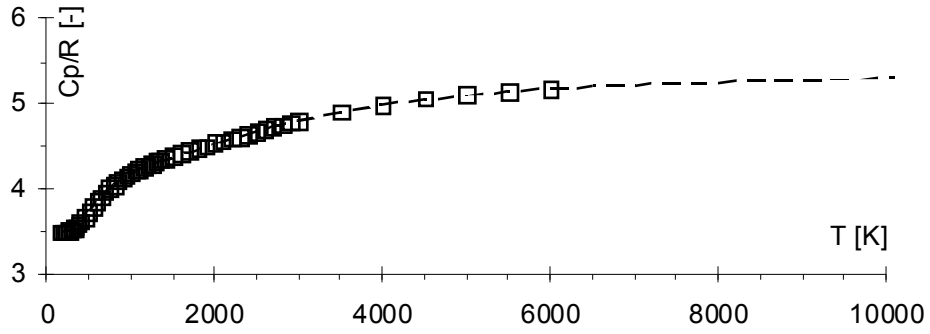

Figure 4.1. The experimental data for heat capacity of oxygen gas as a function of temperature and the fitted curve.

The Θ_1 , Θ_2 , Θ_3 , and Θ_i are the characteristic translational, rotational, vibrational, and electronic temperatures respectively. For the temperature range of interest (T>300K) the translational and rotational modes are fully available as it can be seen from the experimental data presented in Figure 4.1.

Using the published data and equation 4.3 the heat capacity function was determined as

$$c_{p,o_2} = \left[\frac{7}{2} + \frac{1}{2}\left(\frac{1917}{T}\right)^2 e^{\frac{1917}{T}} + \frac{1}{2}\left(\frac{2483}{T}\right)^2 e^{\frac{2483}{T}} + 0.878\left(\frac{10354}{T}\right)^2 e^{\frac{10354}{T}} \right] \cdot R \qquad (4.4)$$

for temperature T in Kelvin.

Now, taking equation 4.2 with 4.4 the relation between process temperature and absorbed microwave power for oxygen plasma can be summarized as

$$P_{absorbed} = R \cdot f_{O_2} \Delta T \cdot \left[\frac{7}{2} + \frac{1}{2}\left(\frac{1917}{T}\right)^2 e^{\frac{1917}{T}} + \frac{1}{2}\left(\frac{2483}{T}\right)^2 e^{\frac{2483}{T}} + 0.878\left(\frac{10354}{T}\right)^2 e^{\frac{10354}{T}} \right] \qquad (4.5)$$

Using equation 4.5 the oxygen plasma temperature dependence on absorbed power for gas flow rates of 5000 sccm and 700 sccm was calculated and the results are presented in Figure 4.2.

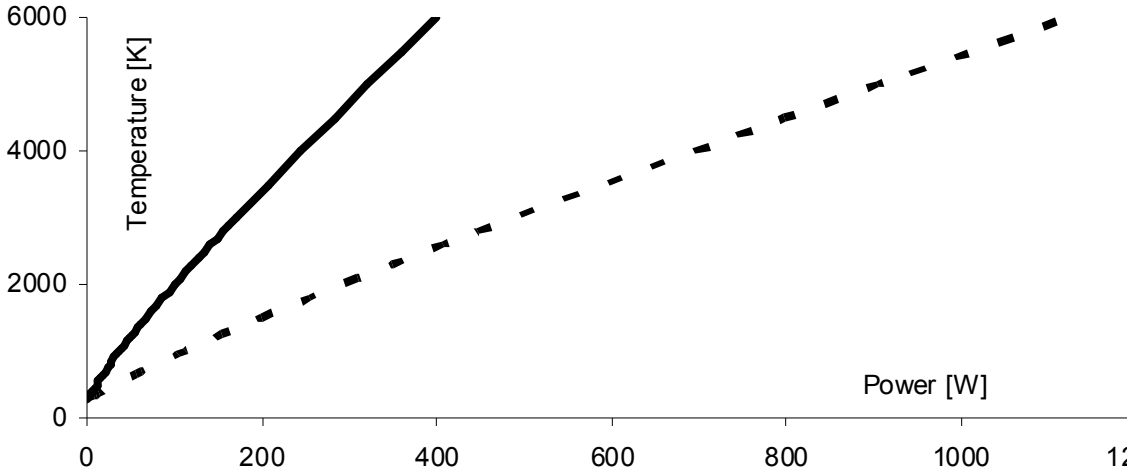

Figure 4.2. The plasma temperature as a function of absorbed microwave power. The oxygen gas temperature for 700sccm (solid line) and 5000sccm (dash line) gas flow were calculated. No radiation and conduction was included.

Since radiative losses increase as T^4, for temperatures higher than 1000K radiative losses can be significant. Therefore, the temperature prediction for argon or oxygen plasmas for the power range given should not ignore the radiative component.

After including the heat absorbed by water vapor, through similar analysis to equation 4.3, the plasma temperature was computed. Adding the precursor flow decreases the plasma temperature for the same absorbed power level as compared to the pure gas case. This was summarized in Figure 4.3. It can be seen that the plasma temperature decreases for larger precursor flow rates. Again, the high plasma temperatures suggest that the radiative energy losses are significant and should not be ignored.

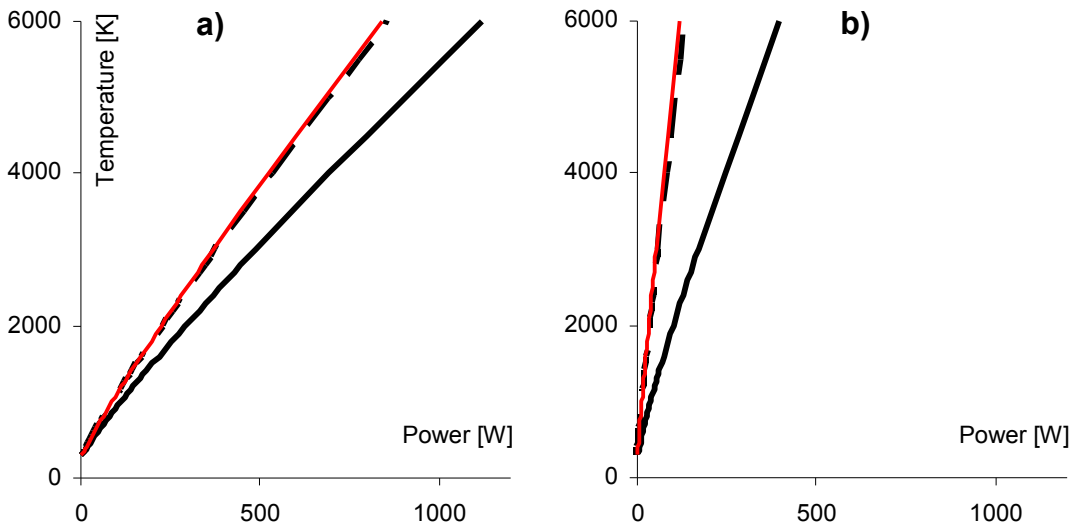

Figure 4.3. The plasma temperature as a function of absorbed microwave power for (a) 5000 ccm and (b) 700 sccm oxygen flow rate. The thick solid, dash, and red thin lines presents data for 1 g/min, 0.1 g/min, and 0.01 g/min precursor (H_2O) flow respectively.

To account for plasma radiation on the plasma temperature the gray body model was used for the radiation of oxygen gas and water vapor mixture.

Planck's law describes the radiative power of black body.

$$u(\lambda,T)=\frac{\beta}{\lambda^5}\left(\frac{1}{e^{\frac{h\cdot c}{k_B T\cdot\lambda}}-1}\right) \tag{4.6}$$

Integrating the above over all frequencies, the power output of black body radiation is described by Stefan-Boltzmann law

$$P=\sigma\cdot A\cdot T^4 \tag{4.7}$$

The gray body model assumes that the object radiates similarly to the black body except that the total radiated power of the gray body is less than that of black body. The proportionality factor ε (emissivity) relates the gray body radiation power to black body radiation power.

$$P_{gray}=\varepsilon\cdot P_{black}=\varepsilon\cdot\sigma\cdot A\cdot T^4 \tag{4.8}$$

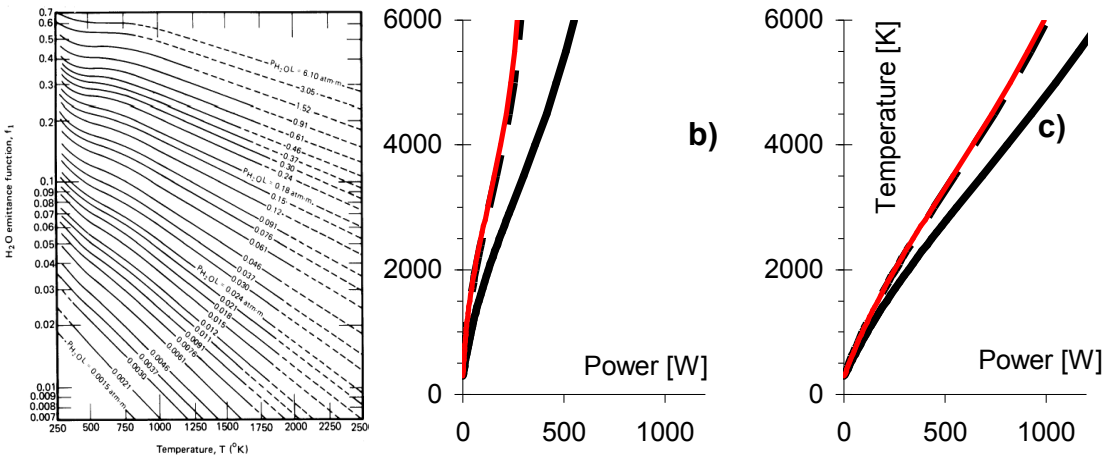

Figure 4.4. Emissivity data (a) and the calculated plasma temperature as a function of absorbed microwave power for (b) 700 sccm and (c) 5000 sccm oxygen flow rate. The thick solid, dash, and red thin lines present data for 1 g/min, 0.1 g/min, and 0.01 g/min precursor (H_2O) flow respectively.

Now, emissivity of oxygen and water vapor mixture strongly depend on its temperature. Using the emissivity data (Hottel 1967) the plasma temperature was

calculated for oxygen and water mixture accounting for the radiative transfer. Figure 4.4 shows a summary of the results.

The plasma temperature changes significantly after the emissivity was accounted for. The material trough output of nebulizer utilized in the MPASD system is about 0.05 g/min. In this regime, the plasma temperature depends little on material flow rate.

The resulting temperature changes with gas flow as well as material flow. However, the plasma dimension affects the radiative transfer rate, thus affecting the plasma temperature. Figure 4.5 shows the effect of plasma size on its temperature. As the plasma size increases, the plasma effective surface area increases resulting in larger radiative transfer. As a result, the plasma temperature decreases.

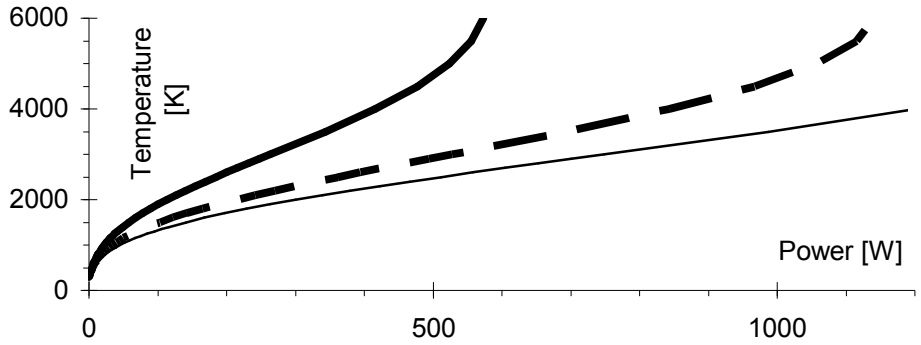

Figure 4.5. Plasma temperature for selected plasma discharge size. The plasma calculation results for (a) 2 cm diameter sphere, (b) 3 cm diameter sphere, and (c) 3 x 3 x 5 cm ellipsoid are presented by dash, solid thick, and solid thin line respectfully. Calculated for precursor flow rate of 0.01g/hr of water.

It is important to notice that the model presented does not predict the size of the plasma discharge.

The calculations presented are very rudimentary and can only be used as an estimate of the plasma temperature. Correct estimation of radiative energy transfer is important, as its effect on temperature prediction is significant: simple gray body modeling is not appropriate for reliable plasma temperature predictions. The spectro-

radiative analysis of oxygen plasma emission shows a spectrum rich in features (Figure 4.X) that change with plasma conditions. The plasma size varies with process conditions, changing the effective gray body surface area. The plasma dimensions cannot be predicted from the simple model presented. In addition, real oxygen plasma is composed not only of molecular oxygen, but also of atomic oxygen, oxygen ions, and electrons. This complicates the calorimetric analysis shown earlier.

Plasma modeling is treated by many authors, and the complexity of these models requires computational techniques to be used. Experimental measurement of the plasma temperatures presents less of a challenge. Experimental plasma characterization methods include the use of probes (Kiss'ovski 2006, 2007), spectroscopic methods (Tatarova 2007, Kitamura, Rabat 2004), and use of waves (Irish 1964, Stott 1969). Electrostatic probes, such as the Langumuir probe allows the determination of the density and temperature of ions and electrons in the plasma. Wave methods include RF cavity perturbation methods and the microwave propagation techniques. These methods allow the determination of electron and ion electrostatic, cyclotron resonance frequency, RF absorption, diffusion, reflection, and phase lag among other parameters. The refraction index found by these methods has direct relationship with plasma density. The spectroscopic methods allow for plasma species identification as well as electron, ion, atom, molecule vibrational, and molecule rotational temperature determination. Plasma emission spectroscopy is non-invasive and experimentally straightforward.

An introduction to plasma temperature determination by emission spectroscopy is described in the next section.

4.2. Emission Spectroscopy for Plasma Temperature Determination

Preliminary spectroscopic measurements of microwave plasma emissions are presented here and the possibility of plasma characterization using emission spectroscopy was discussed. The spectroscopic methods allow for making a qualitative determination of the chemical composition by identifying plasma emission or absorption lines. In addition, spectroscopic methods allow for measurement of electron, ion or atom temperatures especially in hot gasses and plasmas. The electron temperature was calculated using the emission spectroscopy for several plasma conditions.

4.2.1. Spectroscopic Temperature Measurement Theory

Electronic temperature can be determined by measuring the intensity of characteristic emission lines. Assuming local thermal equilibrium (LTE) condition of an optically thin plasma the ratio of two emission lines for a same atom or ion is (Griem 1997)

$$R = \frac{i_{n_1 m_1}}{i_{n_2 m_2}} \approx \frac{\omega_{n_1 m_1} A_{n_1 m_1} g_{m_1}}{\omega_{n_2 m_2} A_{n_2 m_2} g_{m_1}} e^{-\frac{E_{m_1} - E_{m_2}}{k_b T}} \tag{4.9}$$

For the elemental neutral and ionized species the statistical weight, the transitional probability, and frequency can be found from references (nist.gov). The temperature can be determined by direct calculation or by a graphical “slope” method.

The Doppler Effect due to thermal energy of the atom or ion can be quantified by measuring the emission line broadening and the broadening relates to temperature as (Kettani 1973)

$$\frac{\delta \nu_D}{\nu_D} = \frac{\ln(2)}{c} \sqrt{\frac{2 \cdot k_B T}{M}} \tag{4.10}$$

This method needs to be applied carefully as other effects, such as plasma turbulence and pressure, can cause significant broadening of the emission lines. To reduce contribution of other effects this method is mainly used for high temperature plasmas.

The molecule rotational temperature in a plasma has been found to be the same as the gas temperature under certain conditions (Touzeau 1991). The rotational mode emission spectra creates emission bands with closely spaced emission peaks. The rotational temperature of a molecule can be determined from the relation

$$\ln\left(\frac{I_e}{S_{J'}}\right) = A_{nm} - \frac{F(J')\cdot h\cdot c}{k_B T_{rot}} \quad \text{(Kylian 2002)} \tag{4.11}$$

where A_{nm} is the spontaneous transition probability, S_j is line strength, F(J') energy of J' level and I_e is the intensity of the spectral line. Using the graphical "slope" method the temperature T_{rot} can be determined if several spectral lines intensities are known.

4.2.2. Spectroscopy Experimental Setup

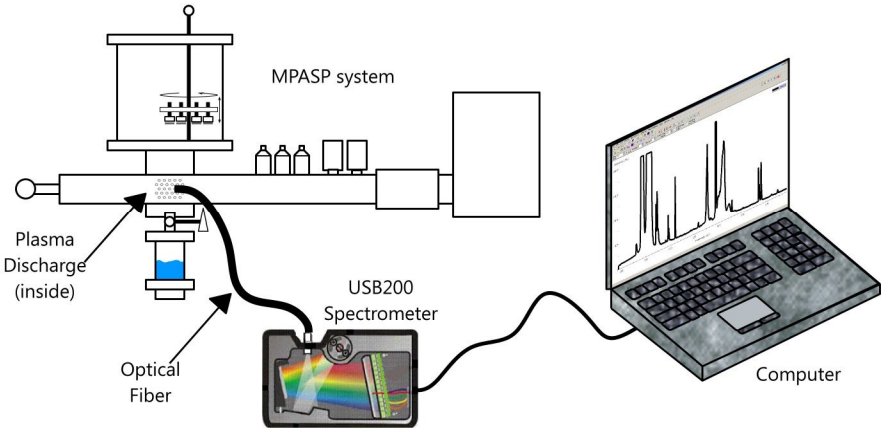

Figure 4.6. Experimental setup diagram for plasma emission spectroscopy.

The spectroscopy measurements were conducted utilizing the USB2000 spectrometer capable of detecting in the 200–900 nm range with optical resolution of 5 nm FWHM. The instrument sensitivity was sufficient to measure the spectra using an optical fiber and without the need of light collecting optics. The experimental setup is presented in Figure 6.4.

4.2.3. Spectroscopy Experimental Results

An example of the collected plasma emission spectrum is presented in Figure 4.7.

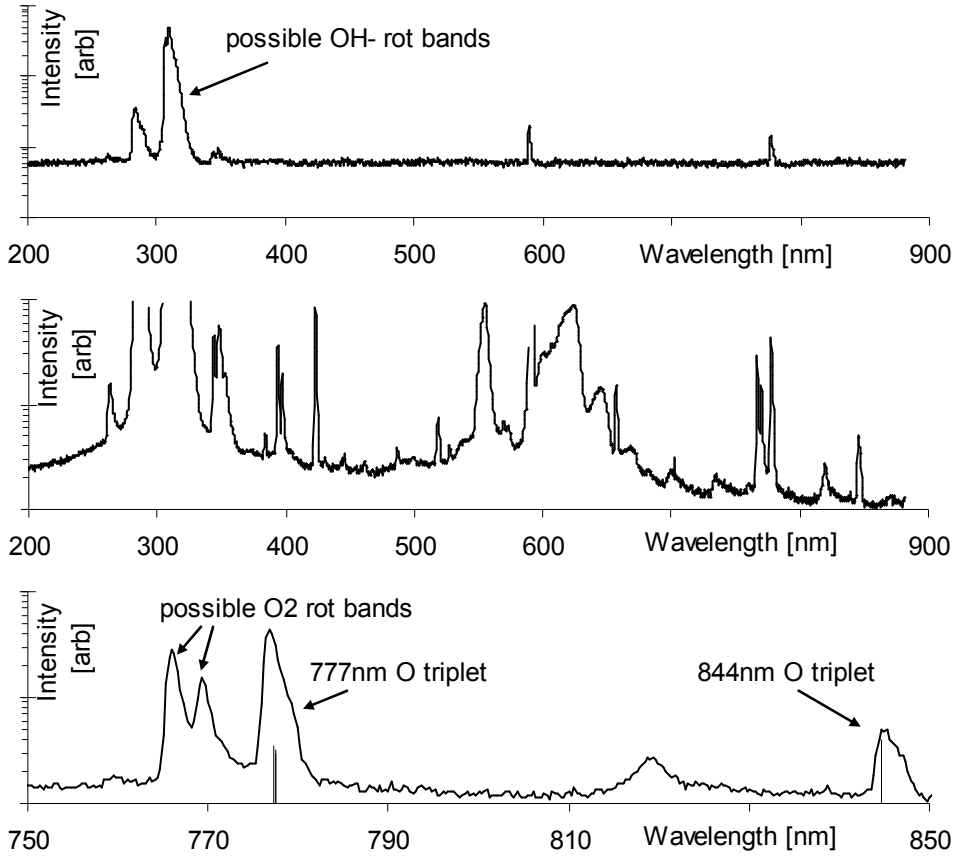

Figure 4.7. Microwave plasma emission spectra. Plasma absorbed microwave power was 200 W, process pressure was 40 Torr, nebulizer duty cycle was 3%, and oxygen gas flow was 700 +18 sccm.

During a short spectrometer detector integration time (low sensitivity), three emission bands were observed at 285 nm, 311 nm, and 350 nm. In addition, there were two peaks observed at 590 nm and 777 nm. During longer a integration time (higher sensitivity), the plasma emission spectrum shows a rich spectrum of atomic emission lines as well as several emission bands. The emission lines at 777 nm and 844 nm are of great interest as these lines are characteristic to neutral oxygen and the electron temperature can be determined from these emission lines. The emission band at around 311 nm is possibly due to a OH^- rotational mode and can be useful to determine the rotational temperature of the OH^- ion (Pellerin 1996). In addition, the emission band around 766 nm is possibly due to O_2 rotational mode, and could be used to calculate the O_2 rotational temperature.

A closer look at the emission lines at 777 nm and 844 nm allows for determination of the electron temperature. The intensity of the emission lines was measured from the collected spectra. The raw data collected by the spectrometer was rescaled to account for nonlinear intensity spectral response of the spectrometer. The reference used for recalibration was emission from a tungsten lamp (2900K).

The plasma emission spectral data collected for plasma under selected pressures was processed and the intensity of 777 nm triplet to 844 nm triplet was calculated. Then the plasma electron temperature was calculated using equation 4.9 from the measured triplet ratio. The resulting calculations were compared in Figure 4.8.

According to these calculations, the electron temperature was as low as 6000 K for 120 Torr plasma and as high as 40000 K for a 20 Torr plasma. The large uncertainty

of the triplet's ratio is due to radiometric calibration uncertainty as well as the uncertainty of the measured intensity.

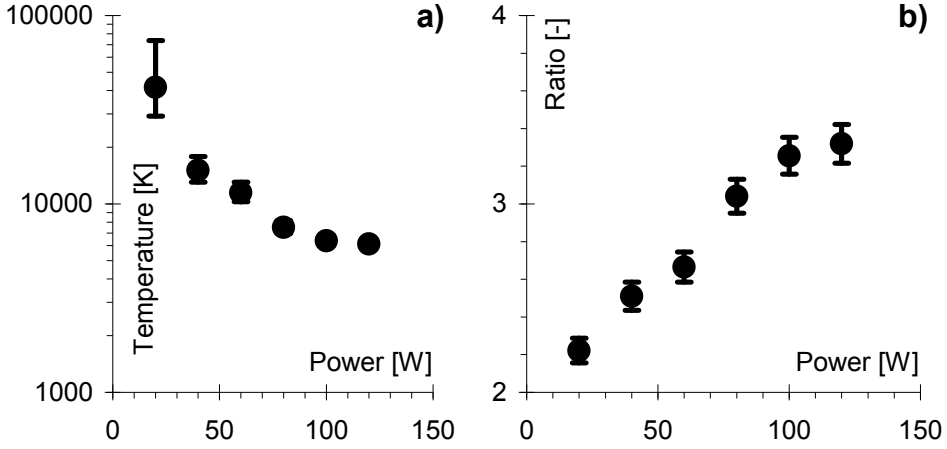

Figure 4.8. Calculated electron temperature as a function of process pressure from the measured emission 777 nm and 844 nm triplet ratio. The data was collected at 400W absorbed microwave power, 700+18 sccm O_2 flow, and 3% nebulizer duty cycle.

Similar calculations of electron temperature conducted on plasma emissions data give absorbed microwave power effect on electron temperature. These results are presented in Figure 4.9.

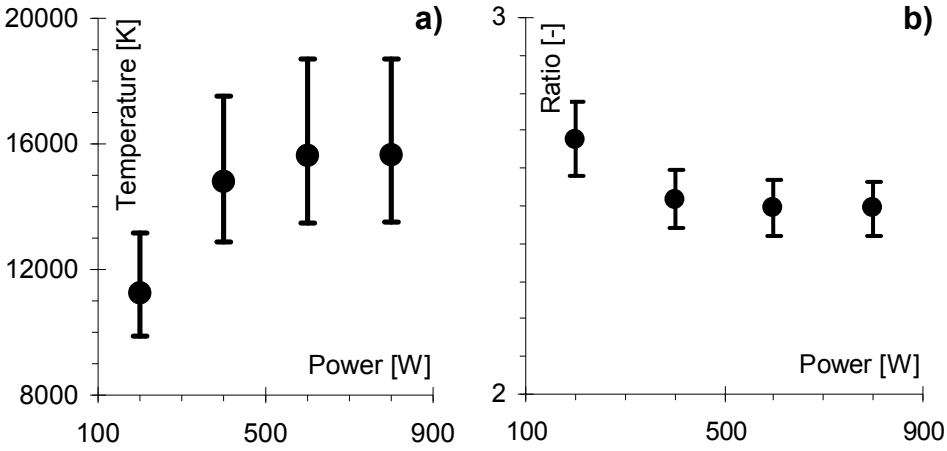

Figure 4.9. Calculated electron temperature as a function of process absorbed microwave power from the measured emission 777 nm and 844 nm triplet ratio. The data was collected at 40 torr process pressure, 700+18 sccm O_2 flow, and 3% nebulizer duty cycle.

The temperature change is smaller than the change observed in Figure 4.8. The temperature was determined to be between 1100 K for the 200 W generated plasma and 1500 K for 1000 W generated plasma. Again, the uncertainty of the observed temperature is due to radiometric calibration uncertainty and the uncertainty of the measured intensity.

The electron temperature measurement results might improve if additional spectral lines are measured. Looking at Table 4.1, the triplet emission at 926 nm is a good candidate for such calculations.

Table 4.1. Wavelength, transition probability, upper state statistical weight, and upper state energy for selected strong emission lines of neutral oxygen atom. (nist.gov)

λ [nm]	A_{nm} [s^{-1}]	g_m [-]	E_m [eV]
777.194	$3.69 \cdot 10^7$	7	10.740931
777.417	$3.68 \cdot 10^7$	5	10.740475
777.539	$3.70 \cdot 10^7$	3	10.740224
844.625	$3.22 \cdot 10^7$	1	10.988880
844.636	$3.22 \cdot 10^7$	5	10.988861
844.676	$3.22 \cdot 10^7$	3	10.988792
926.267	$2.60 \cdot 10^7$	5	12.078644
926.277	$2.97 \cdot 10^7$	7	12.078629
926.601	$4.44 \cdot 10^7$	9	12.078618

It is worth notice that the electron temperatures measured at higher pressures (80, 100, and 120 Torr) are around 6000 K a number similar to the calculated values presented in Figure 4.5.

The emission bands observed around 310 nm and 766 nm suggest that the rotational temperature of OH^- ion and O_2 molecule can be calculated. However, the resolution of the experimental setup used to collect data prevents measurement of

necessary data for calculations. In order to perform the calculation from equation 4.11, spectroscopic data with a resolution of 0.025 nm or better is recommended.

The temperature broadening for 777 nm line changes as $\sqrt{T}$ and can be calculated using equation 4.10. This broadening varies from 0.0025 nm FWHM at 300 K to less than 0.05 nm FWHM for temperature of 40000 K. This suggests that high-resolution spectrometers are necessary for the determination of temperature. However, the pressure broadening and Stark broadening due to RF electric field can make it difficult to measure the plasma temperature.

The experimental setup utilized for this initial study had optical resolution of only 9 nm. This prevents observation of the thermal broadening. In theory, this method allows for calculation of ion or atom temperature, however, the required instrumentation and possible difficulty of removal of effects of peak broadening resulting from strong electric field within the plasma and broadening due to plasma pressure might render this method impractical.

4.3. Plasma Ignition Study

The ignition of gas plasma discharge occurs when the rate of gas ionization exceeds the rate of electron recombination. In high frequency discharge, the rate of gas ionization depends on pressure, the strength of electric field and its orientation as well as the discharge chamber dimensions and geometry and the properties of the gas.

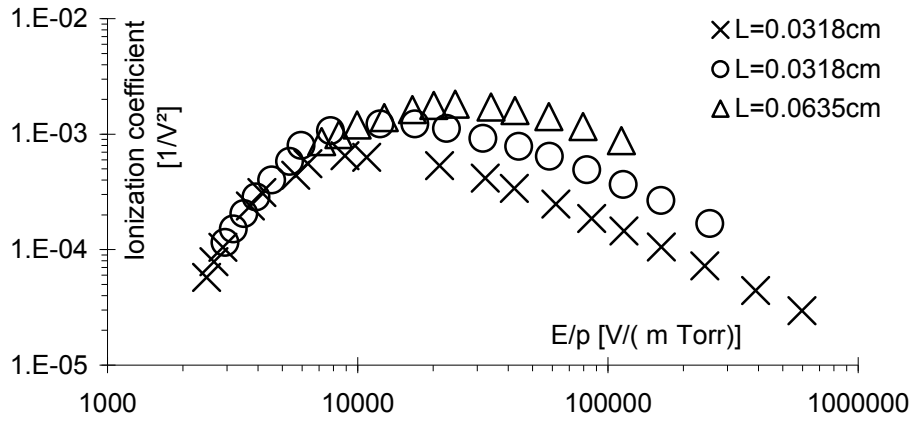

Figure 4.10. High frequency ionization coefficient ζ of air as a function of E/p (Herlin 1948).

In a parallel plate configuration with plate separation L and for a gas with ionization coefficient ζ the electric breakdown condition is given by (Herlin 1948)

$$\zeta = \frac{1}{\left(\frac{L}{\pi}\right)^2 \cdot E^2}. \tag{4.12}$$

The ionization coefficient ζ varies with strength of the electric field, pressure, and depends on experimental system dimensions as presented in Figure 4.10.

The resulting break down electric field dependence is shown in Figure 4.11. It is clear that there exists a pressure at which the electrical breakdown occurs its lowest electric field. As presented in Figure 4.11, the plate separation L affects the minimum electric field needed to breakdown air and the pressure at which the minimum occurs. Similar studies for other gases such as oxygen, air, and argon show a similar characteristic.

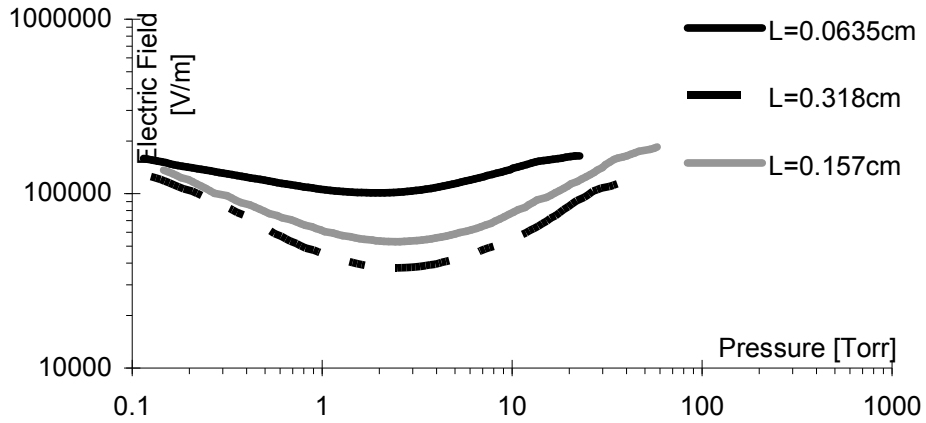

Figure 4.11. Breakdown electric field for air as a function of pressure for parallel plate configuration at three different distances (Herlin 1948)

The geometry of MPASD plasma zone creates non-uniform electric field , unlike parallel plate configuration used to derive equation 4.12, then the electrical breakdown of gas cannot be readily predicted for there is no ionization coefficient data available for MPASD plasma applicator geometry. However, it is reasonable to expect that the electric field strength needed for electric breakdown of gas in MPASD will change with process pressure. This change is expected to have similar features to the data shown in Figure 4.11: there exists a pressure at which the electric field strength needed for electric breakdown of gas is at a minimum.

4.3.1. Plasma Ignition Experimental Setup

The system condition at which the electric field strength needed for plasma ignition is at its minimum is the optimum condition for plasma ignition. In MPASD this condition depends on the process pressure and the waveguide short position. In order to determine the optimum ignition configuration of MPASD system a gas electric breakdown (or plasma ignition) study was conducted. In this study the output power of

the microwave source was varied to determine the strength of electric field needed to cause electric breakdown of the process gas. The study measured the forward microwave power level needed for gas electric breakdown as a function of pressure and position of waveguide short.

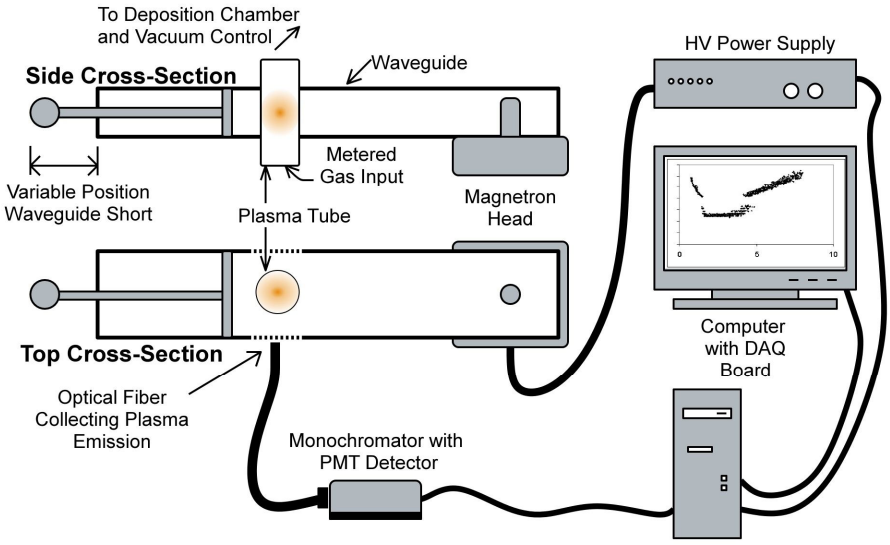

Figure 4.12. Diagram of the experimental setup for the electrical discharge of oxygen and argon gas in MPASD system.

Figure 4.12 presents the diagram of the experimental setup used for this study. The power level of the microwave magnetron was computer controlled.

Table 4.2. List of major components of plasma ignition study experimental setup.

PN:	Manufacturer	Description	Comments
-	-	MPASD system	See table 3.2
EP200	Verity	Monochromator	
GA1219	GAE	Waveguide Isolator	Optional
P400-5-UV-VIS	Ocean Optics	Optical Fiber	

The plasma ignition was detected using optical monochromator with build in PMT detector (Variety EP200) tuned to a selected atomic line of the process gas emission.

The electrical signal from the monochromator was connected to the computer through the DAQ card (National Instruments PCI-6251) and the signal was processed with the help of the custom written *ignition.vi*, a LabView virtual instrument program. The *ignition.vi* program also allows controlling and monitoring of the process pressure and microwave forward power.

After manually adjusting the variable position short at the desired location the *ignition.vi* program sweeps through the desired pressure range. The waveguide short position is measured from an arbitrarily chosen 0 cm location, and this location is kept constant throughout the experiment.

At each pressure step, the program increases the microwave forward power from 0 W until plasma is detected by the monochromator. The power level at which the plasma begins to occur together with the corresponding pressures is then stored into a file for further data analysis.

However, after the plasma is extinguished and after the microwave power is reduced to 0 W there is some ionized gas remaining in plasma tube. This ionized gas reduces the electric field needed to ignite the plasma in next experiment cycle. This in turn gives lower values for electric field strengths. The goal of the ignition study was to determine the electric field strength needed for plasma ignition in a situation where the gas is not already ionized. To reduce the remaining ions effect on ignition during the experiment the process gas was flown through the plasma zone at a rate of 18 sccm. This helps to remove ionized gas after each gas electrical breakdown and before the microwave power is cycled again.

4.3.2. Plasma Ignition Study Initial Results

Figure 4.13 presents two data steps of the ignition study for oxygen gas. As it is expected there is a pressure at witch the microwave power needed for ignition is at its lowest. From the graph it appears that the minimum occurs in the pressure range of 1.5 to 4 Torr.

The electric field within a rectangular waveguide can be calculated using the microwave power level and waveguide dimensions. The peak electric field strength in the rectangular waveguide with dimensions *a* and *b*, for a wave with free space wavelength λ_0' operating at $TE_{m,n}$ mode is given by equation 3.3. In the case of WR340 (a=86.4 mm, b=43.2 mm) waveguide operating at 2.45 GHz in $TE_{1,0}$ mode and power level *P* the strength of electric field within the waveguide is

$$E_{RMS} = 535\sqrt{P} \tag{4.13}$$

However, the strength of electric field in the discharge tube during the ignition experiment can not be estimated using equation 4.13.

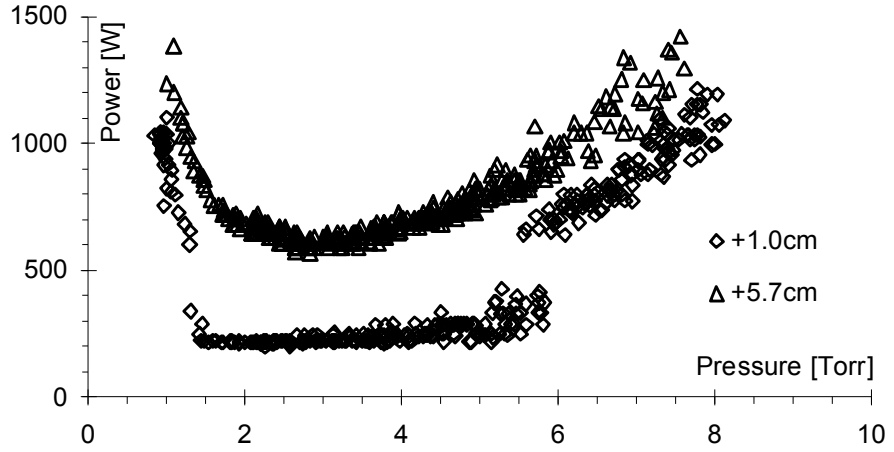

Figure 4.13. Experimentally determined minimum microwave forward power level during electrical breakdown of oxygen gas in MPASD system as a function of pressure at selected positions of waveguide short.

The dependence of the results in Figure 4.13 on the waveguide short position suggests that the electric field strength within the discharge tube varies depending on the waveguide short position. This effect is due to interference of the wave reflected by the waveguide short with the forward wave (see Figure 4.14a). This interference of the two waves creates locations of high electric field and locations of low electric field.

This effect is verified by rearranging the experimental setup to eliminate the reverse power. The new setup is presented in Figure 4.14b. An additional waveguide isolator was installed after the plasma applicator. In this arrangement, all of the microwave energy that passes through the plasma applicator is absorbed in the waveguide isolator and not reflected back as was the case in the experimental setup from Figure 4.14a.

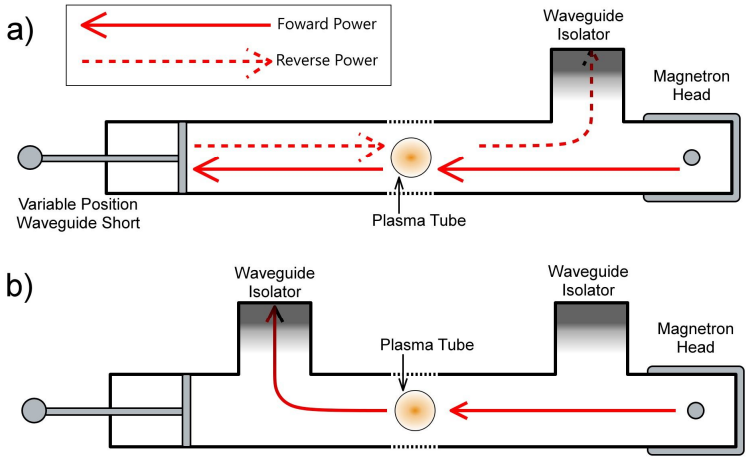

Figure 4.14. Microwave power flow diagram for (a) ignition study experimental setup and (b) the setup modified to reduce reverse power.

Utilizing the modified experimental setup shown in Figure 4.14b, values of the minimum microwave power needed to create breakdown of gas were collected for argon, oxygen, and air. The electric field strength from the collected data was calculated using

equation 4.13 and presented in Figure 4.15. The results in this configuration do not depend on the waveguide short position.

The results are similar to the result in Figure 4.11. Both have its minimum in the 2 to 4 Torr range. The minimum breakdown electric field strength found for air through experiment (16kV/m) is lower from the one shown in Figure 4.11 (40kV/m – 120kV/m). The difference is due to different geometry of MPASD plasma discharge zone from the idealized parallel plate capacitor arrangement used to compute Figure 4.11.

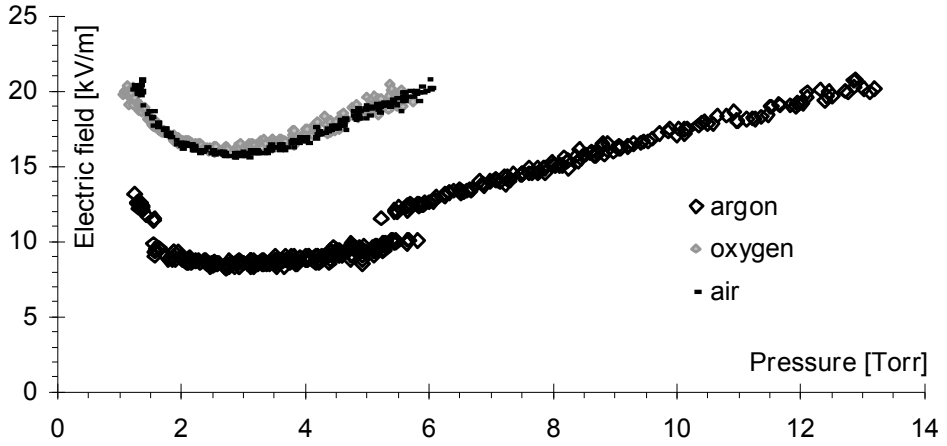

Figure 4.15. The breakdown electric field strength of different gasses as a function of pressure. Data collected using system shown in figure 4.14b.

4.3.3. Oxygen Plasma Ignition Study Results

The results of the ignition of oxygen plasma study performed using the experimental setup shown in Figure 4.12 are summarized in Figure 4.16. Each data set was processed to show the average microwave power at plasma ignition as a function of pressure

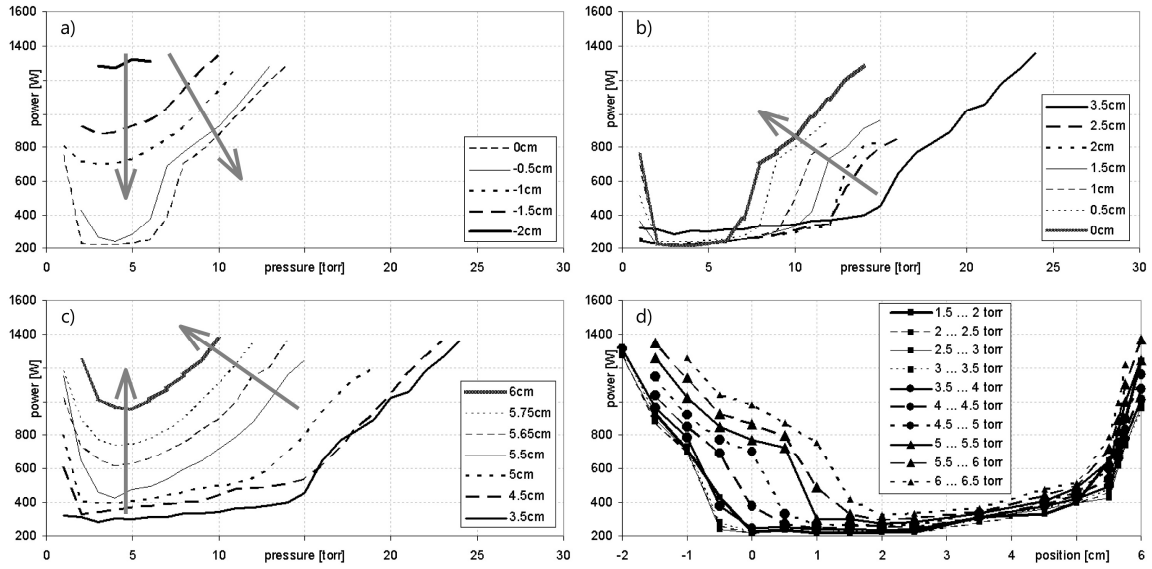

Figure 4.16. Average microwave power level needed to cause electrical breakdown of oxygen gas as a function of (a, b, c) pressure and (d) waveguide short position. The arrows show the direction of increasing waveguide short position (away from the plasma).

The dependence of ignition condition on the waveguide short position is summarized in Figures 4.16(a,b,c). Initially, as the waveguide short is close to plasma zone, the microwave power level needed for plasma ignition is high. However, as the waveguide short is moved away from the plasma zone the microwave power needed decreases (Figure 4.16a). While the waveguide short is moved from the 0 cm to 3.5 cm location the minimum microwave power needed remains constant, but the pressure range of the minimum microwave power range decreases (Figure 4.16b). Further movement of the waveguide short results in an increase of the plasma ignition minimum microwave power and reduces the pressure range (Figure 4.16c).

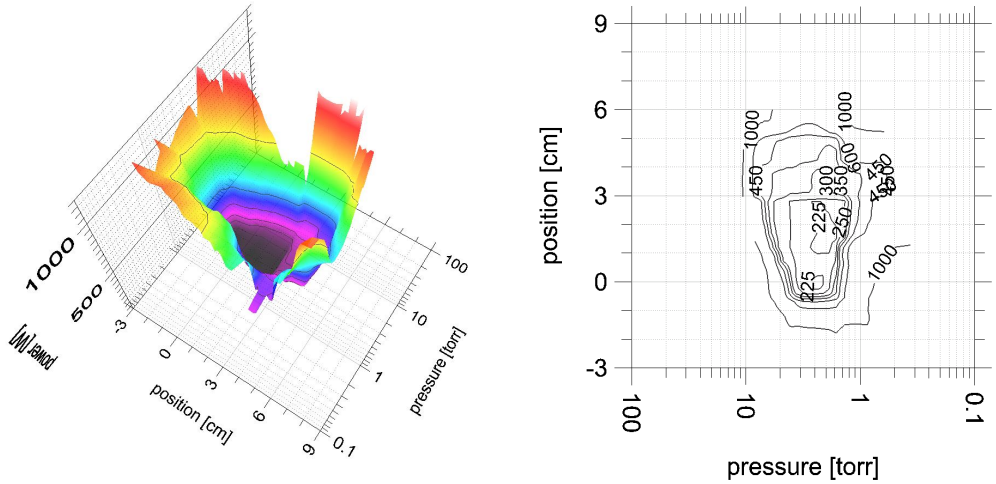

Figure 4.17. 3D (a) and (b) contour plot of experimentally obtained average microwave power level needed for oxygen plasma ignition as a function of position and pressure.

The Figure 4.17 allows to determination of the minima of the average microwave power level needed to ignite the oxygen plasma. Figure 4.17a shows that such a minima exists, and Figure 4.17b locates the minima in the pressure-power plane. The minima (the optimum ignition condition for MPASD system) for oxygen plasma ignition setting was determined to be 2 Torr, 2 cm waveguide short position, and microwave forward power of more than 225 W.

4.3.4. Argon Plasma Ignition Study Results

The ignition experiment was repeated for argon as the plasma medium. Similar to the results for oxygen there was significant dependence of microwave power needed to ignite plasma as a function of position and gas pressure. Figure 4.18 summarizes the collected data and allowed determination of the minima of the average microwave power level needed to ignite the argon plasma. Figure 4.18a shows that such a minima exist as well, and Figure 4.18b locates the minima in the pressure-power plane. The minima (the optimum ignition condition for MPASD system) for argon plasma ignition setting was

determined to be 3.5 Torr, 3 cm waveguide short position, and microwave forward power of more than 50 W.

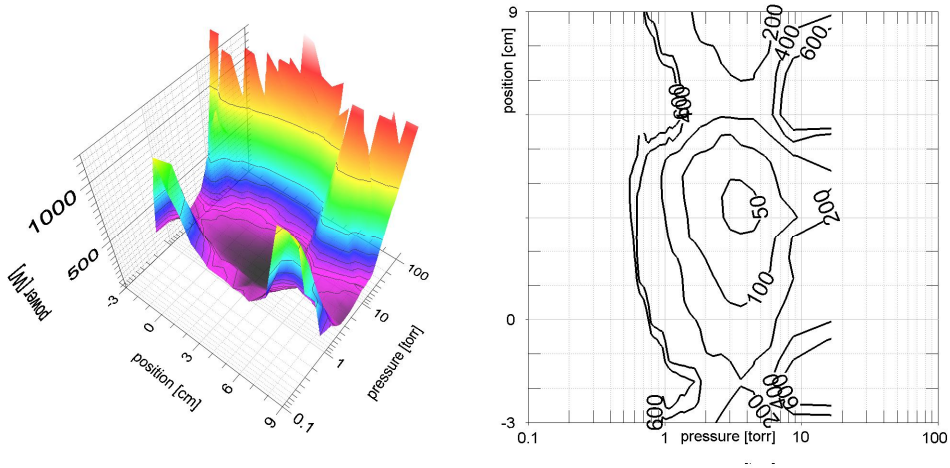

Figure 4.18. 3D (a) and (b) contour plot of experimentally obtained average microwave power level needed for argon plasma ignition as a function of position and pressure.

4.3.5. Air Plasma Ignition Study Results

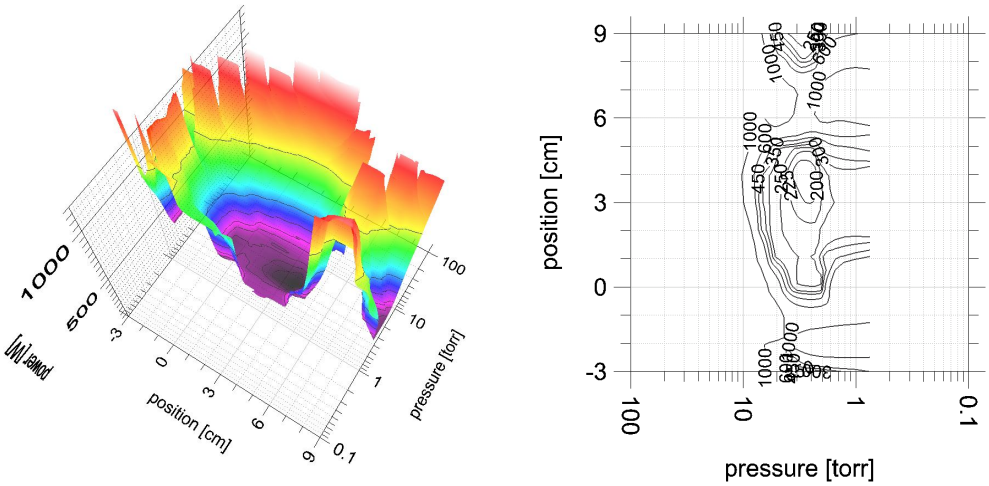

Figure 4.19. 3D (a) and (b) contour plot of experimentally obtained average microwave power level needed for air plasma ignition as a function of position and pressure.

The plasma ignition study was again conducted but using air as the plasma discharge gas. This study again showed the strong position and pressure dependence of

the power necessary to ignite the plasma. Figure 4.19 summarizes the microwave power level dependence on position and pressure during plasma ignition. Similar to the study for oxygen and argon there is a condition where the air plasma ignition occurs at the lowest power level. From Figure 4.19b this occurs at a pressure of 8 Torr, 3 cm position of the waveguide short, and with minimum power of 180 W.

4.3.6. Plasma Ignition Study Summary

The plasma ignition study showed that there was a strong relationship between the microwave power level necessary to ignite the plasma, the plasma gas pressure, and the MPASD system waveguide short position. The optimum conditions for the plasma ignition for oxygen, argon, and air were determined and the values were summarized in Table 4.3.

Table 4.3. MPASD process setting for optimum plasma ignition conditions.

Plasma gas	Waveguide position	Process gas pressure	Minimum power
Oxygen	2cm	2.0Torr	225W
Argon	3cm	3.5Torr	50W
Air	3cm	8.0Torr	180W

In addition, it was verified that the ignition microwave power level dependence on position is due to the reverse microwave interfering with the forward wave to create areas of high and low electric field strength.

4.4. Plasma Tail Temperature Study

As the gas exits the plasma zone, the MW source supplied energy is no-longer available to maintain the temperature and the temperature decreases due to radiation, gas expansion, and mixing with cooler gases. The temperature of the plasma tail in relation to the distance from the waveguide at given gas flow, process power, and pressure was studied. The tail temperature decreases with distance from the waveguide

4.4.1. Plasma Tail Temperature Study Experimental Setup

The experimental setup for this study is shown in Figure 4.20. The k-type thermocouple was used to probe the temperature. The location of the thermocouple was adjusted using the sample holder assembly and the plasma temperature was measured in the center of the gas flow.

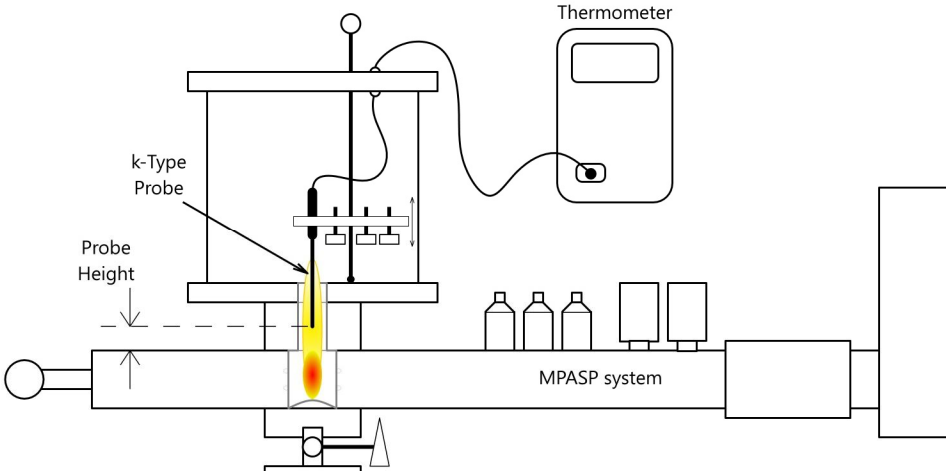

Figure 4.20. Plasma tail temperature study experimental setup.

Plasma tail temperatures were measured after the process pressure, microwave power, waveguide position, and waveguide tuner setting were adjusted until microwave reflected power was minimized and the desired absorbed power was reached.

.

4.4.2. Plasma Tail Temperature Study Results

The relation of plasma temperature and probe position is summarized in Figure 4.21. The tail temperature decreases with probe distance from the plasma zone. The distances of 44 mm and higher are possible sample locations and the temperatures in these locations were as high as 615 K. The lowest measured temperature was 370 K at 84 mm and 218 sccm of O_2 flow. The plasma tail can be utilized to heat the substrate by placing it close to the plasma zone opening. On the other hand samples that are sensitive to temperature can be placed farther away from the plasma opening where the tail temperature is lower and the process parameters can be changed to further decrease the tail temperature at the sample location.

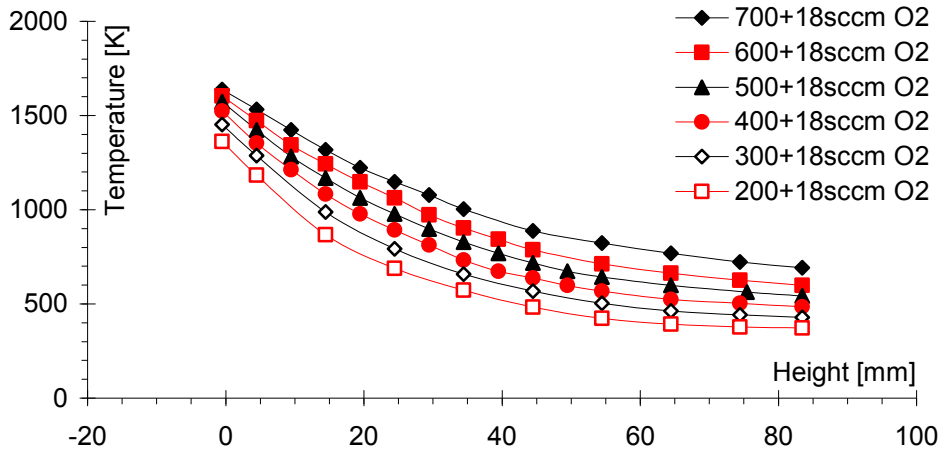

Figure 4.21. Plasma tail temperature as a function of probe position for selected material flow rates. The process pressure was 60 Torr and process power was 1000 W of absorbed power and nebulizer duty cycle was 3%.

It was found that the plasma temperature decreases with gas flow rate. This was surprising since the previous models predict that the temperature of the plasma increases with decreasing flow. The decrease of the temperature of the plasma tail with gas flow can be explained by looking at the time a gas molecule takes to move from plasma to the

location probed in the experiment. At lower gas flows this time is longer. This will result in more energy radiated away from the gas thus lower temperature of the gas in plasma tail.

The plasma tail temperature dependence on process pressure is presented in Figure 4.22. The process pressure was varied between 20 and 16 Torr. The tail temperature was measured at positions of 4 mm, 44 mm, and 84 mm away from the plasma zone. There was some variation (125 K) at position of 4 mm away from plasma zone, however, the variation is less significant at other distances.

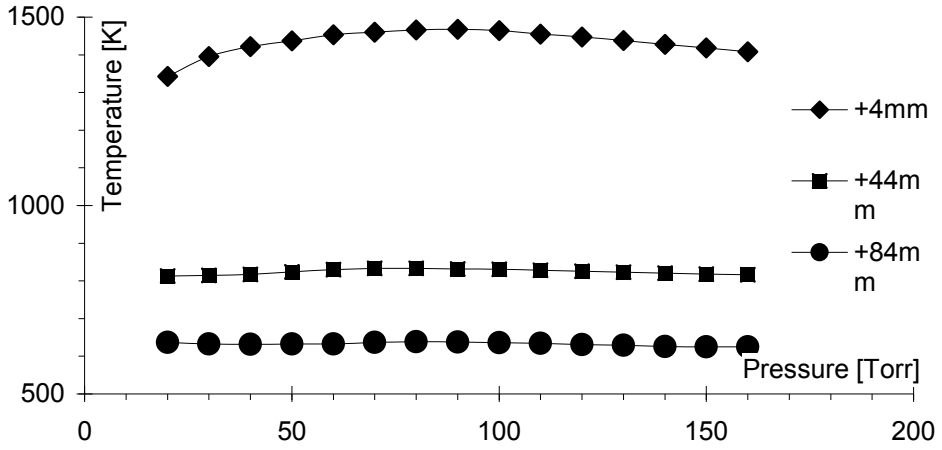

Figure 4.22. Plasma tail temperature as a function of process pressure for selected probe positions. The process power was 600 W, the process gas flow was 700 + 18 sccm O_2 and nebulizer duty cycle was 3%.

The plasma tail temperature dependence on nebulizer duty cycle is summarized in Figure 4.23. The nebulizer output mass flow dependence on its power duty cycle was presented in Section 4.5.

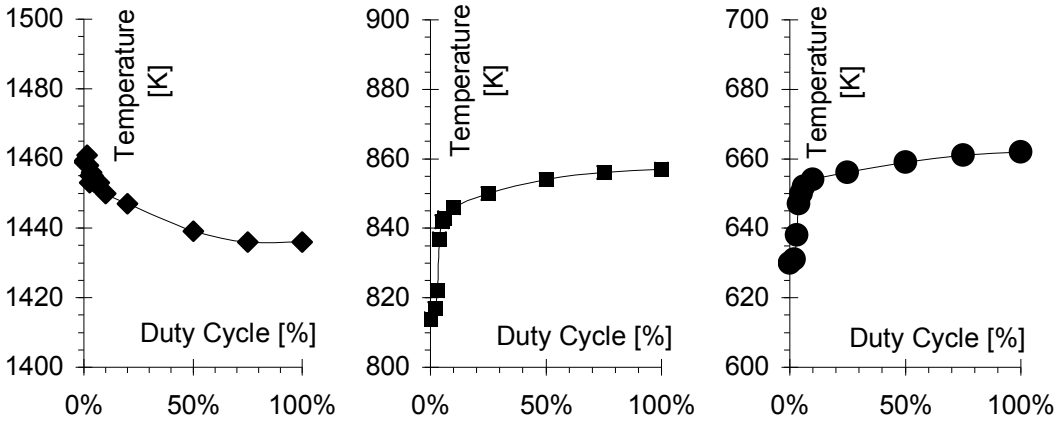

Figure 4.23. The plasma tail temperature as a function of nebulizer duty cycle for probe positions of (a) +4 mm, (b) +44 mm, and (c) 84 mm away from plasma zone. The process power was 600 W, process pressure was 60 Torr and the O_2 gas flow was 700 + 18 sccm.

The temperature of the plasma tail at a location of 4 mm away from the plasma zone decreased with increased nebulizer duty cycle. This is expected as the plasma temperature is expected to decrease with increased material flow. However, the temperature of the plasma tail at locations of 44 mm and 84 mm away from the plasma zone increase with increasing duty cycle of the nebulizer.

The increase of the temperatures at the 44 mm and 84 mm is consistent with the results for plasma temperature increase with gas flow as presented in Figure 4.21. Higher gas flow is expected for experiments with higher generated droplet flow rate due to higher water vapor content.

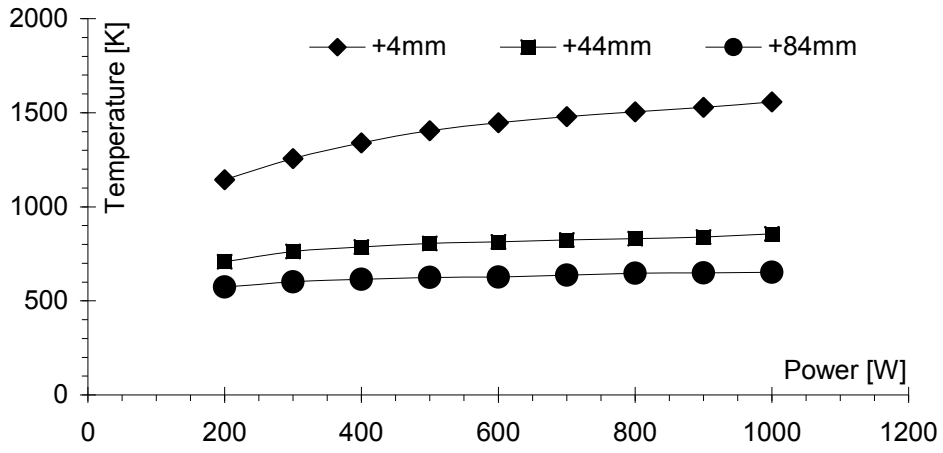

Figure 4.24. Plasma tail temperature as a function of absorbed microwave power for selected probe positions. The process pressure was 60 Torr, the process gas flow was 700 + 18 sccm O_2 and nebulizer duty cycle was 3%.

Plasma tail temperature also depends on absorbed microwave power. This relation is shown in Figure 4.24. Since increased absorbed microwave power is expected to increase the plasma temperature then the plasma tail temperature is also expected to increase. Indeed the plasma tail temperature increases with increasing absorbed power. However, the increase is small. Increase of the absorbed power from 200 W to 1000 W raises the tail temperature only 400 K at a position of 4 mm away from plasma zone. The plasma temperature at 200 W of absorbed power is 870 K higher than the temperature of the process gas as it enters the plasma zone.

4.4.3. Plasma Tail Temperature Study Summary

The plasma tail temperature decreases as the distance from the plasma increases. The plasma tail temperature pressure dependence is significant only at close distances from the plasma. Power changes do change the tail temperature especially at close

distances and the effect decreases at large distances from plasma. The material flow effect on the plasma tail temperature is small for the material flows utilized.

The plasma tail can be utilized as a mechanism of substrate heating or the plasma temperature at the sample location can be reduced by changing location of the sample. If the heating of the substrate by the plasma tail is insufficient for a given sample then the active heating can be implemented by utilizing an electric sample heater. For some samples the plasma tail heating might be excessive then active cooling of the sample would be required.

4.5. Atomizer Generation Rate

The generation rate study was conducted to determine the amount of material being generated under selected duty cycle operation of the nebulizer. The atomization rate is too small to measure below a 2% duty cycle and it remains constant above 10%. Between 2% and 10% of duty cycle the generation rate of the atomizer can be adjusted from 0 to 13 g/hr.

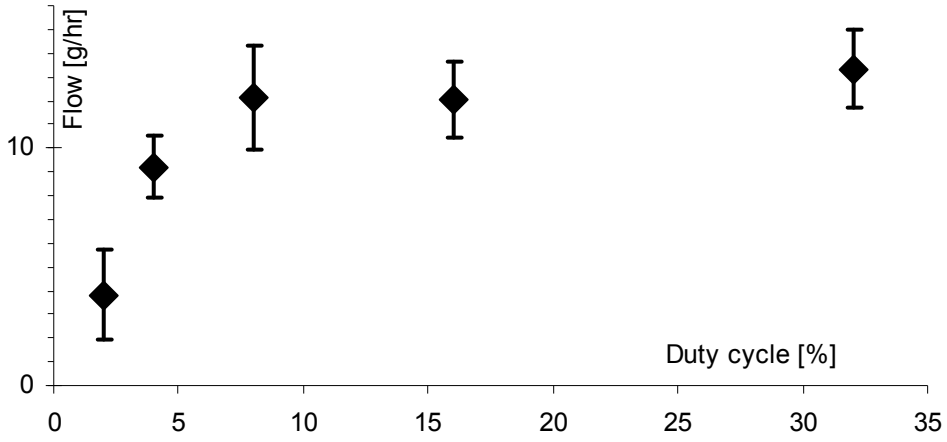

Figure 4.25. The atomizer generation rate as a function of power duty cycle.

4.6. Chapter Summary

MPASD system was shown to be capable of creating plasmas in argon, oxygen, and air, and optimal ignition settings were determined. The plasma was sustained upon introduction of atomized water. The electron temperature for the plasma was measured to be between 6000 K and 40000 K. The pressure and microwave power effect on electron temperature was observed. The plasma tail was measured and the position, pressure, power, and flow relation to temperature was measured. In addition, the atomizer generation rate was characterized.

CHAPTER 5. Case Study: Y_2O_3:Eu Nanophosphor

The synthesis of Y_2O_3:Eu nano-particles using the MPASD system described in Chapter 3 and Chapter 4 is presented here. The ability to successfully synthesize nanoarticles with varying properties that depend on process settings is shown. The coatings of Y_2O_3:Eu were analyzed and their crystal structure, crystal lattice size, luminescence was determined. In addition coating growth rate was measured and coating quality was observed.

5.1. Y_2O_3 and Y_2O_3:Eu Overview

Yttrium oxide, Y_2O_3, is an air-stable, white, solid substance. It is the most important yttrium compound and is widely used to make YVO_4 europium and Y_2O_3 europium phosphors that give the red color in color TV picture tubes and it is a common starting material for both materials science and inorganic compounds. Yttrium oxide is also used to make yttrium iron garnets, which are very effective microwave filters and yttrium aluminum garnet (YAG) for use as a lasing media.

The Y_2O_3 crystal is excellent host for lanthanides. Lanthanide doped Y_2O_3 crystals are widely used for their luminescence in visible and infrared range. The luminescence ranging from blue (Tm), trough green (Tb), yellow (Dy), pink (Sm), red (Eu), and infrared (Er, Tm, Yb, Nd) is possible for lanthanide doped Y_2O_3 (Guyot 1996,

Yoda 2004, Anh 2007). High thermal conductivity of Y_2O_3 makes it a promising material for high power laser media, being a possible replacement for the YAG crystal.

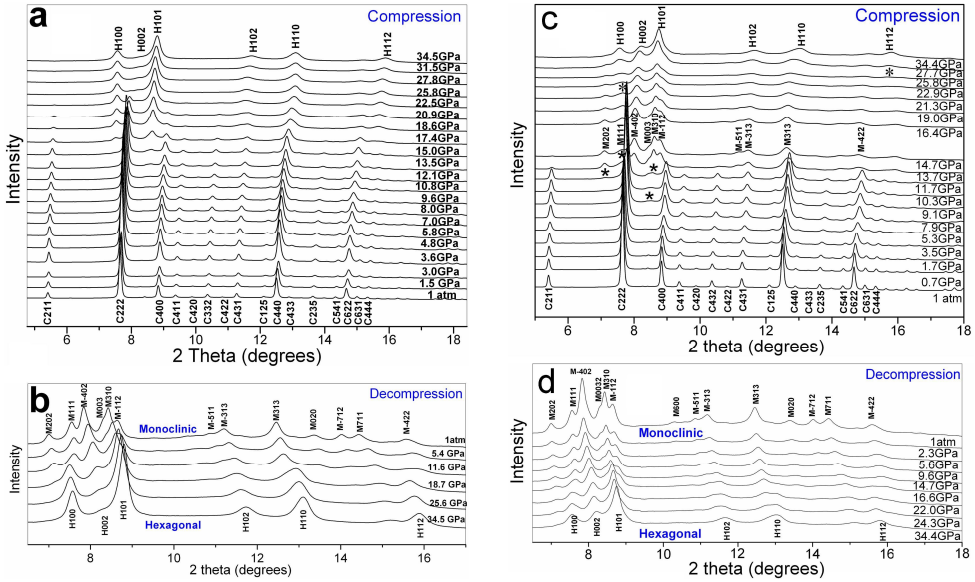

Figure 5.1. High pressure transition of (a, b) Y_2O_3 and (c, d) Eu:Y_2O_3. Reproduced from Wang (2009). X-ray wavelength λ=0.4084Å

The Y_2O_3 crystal has been observed to have cubic, monoclinic and hexagonal structures. The most common body centered cubic structure is widely utilized and synthesized commercially. The phase change from cubic to hexagonal upon compression and from hexagonal to monoclinic during decompression has been observed in high pressure studies of Y_2O_3 phase transitions (Wang 2009).

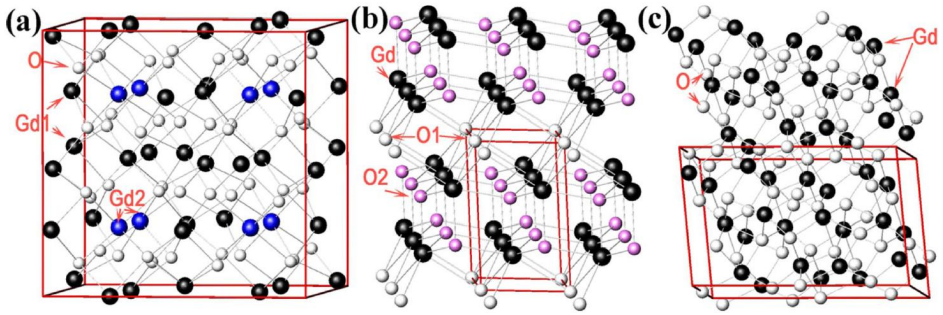

Figure 5.2. The Crystal structure of (a) cubic, (b) hexagonal, and (c) monoclinic Gd_2O_3 crystal. Reproduced from Zhang (2008)

Similar studies for Y_2O_3:Eu showed that the crystal cubic structure changes to monoclinic under high pressure and then to hexagonal at even higher pressures. Upon decompression the hexagonal crystal reverts to monoclinic phase. The monoclinic phase is stable at atmospheric pressure.

The structure of Y_2O_3 is similar to the Gd_2O_3 crystal presented in Figure 5.2 where the cubic, hexagonal, and monoclinic phase crystal structure is shown. The differences between crystal structures are important for Eu doped Y_2O_3 crystal as the crystal effect on the doped site is important for luminescence. Cubic Y_2O_3 has two distinct cation sites each six way coordinated. The oxygen atoms are located about the cation site on a distorted cube structure with two oxygen sites empty (Figure 5.3a), a quasi-octahedral arrangement (Frantisek 1984, Jollet 1990, Maslen 1996).

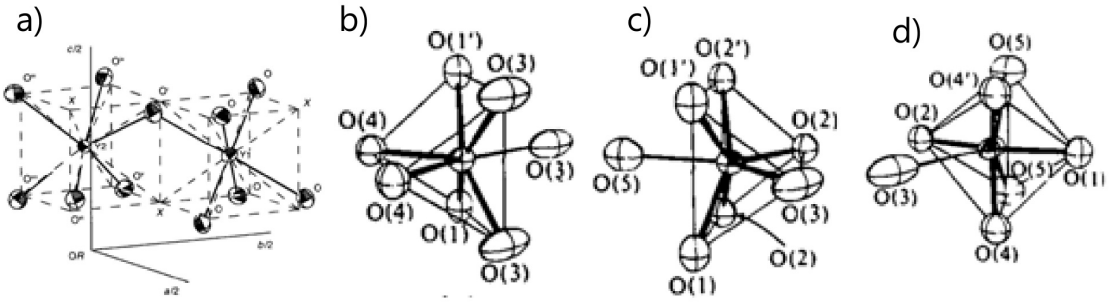

Figure 5.3. The cation site coordination for (a) cubic Y_2O_3 and (b, c, d) monoclinic Eu_2O_3. Reproduced from Maslen (1996) and Yakel (1978).

For the monoclinic phase of Y_2O_3 there are three distinct cation sites each seven fold coordinated. Two sites can be described as having oxygen located at the apexes of a trigonal prism with seventh oxygen located on a normal to the face. The third site is a distorted octahedron with seventh oxygen laying at large distance. This is similar to the monoclinic Eu_2O_3 presented in Figure 5.3b, c, and d.

The XRD patterns of most often observed body centered cubic (BCC) or the base centered monoclinic (monoclinic) crystal structures of Y_2O_3 are presented in Figure 5.4.

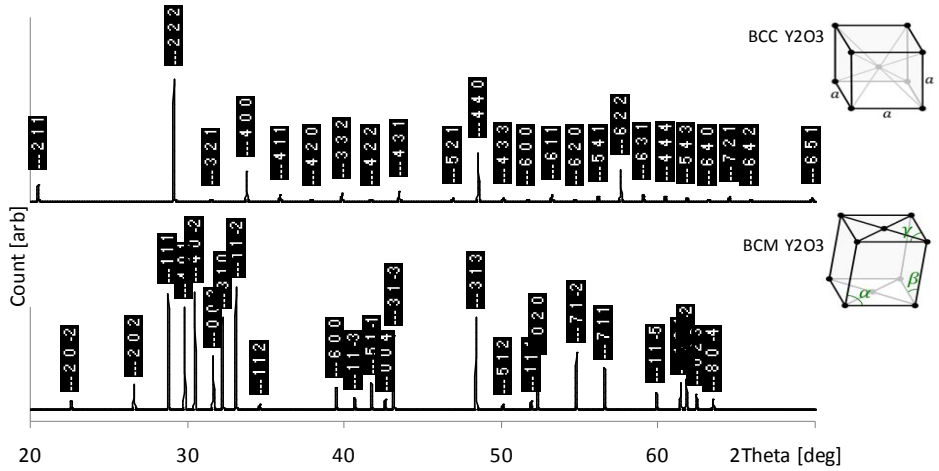

Figure 5.4. Powder XRD patterns of body centered cubic and base centered monoclinic Y_2O_3. X-ray wavelength λ=1.5406Å.

The distinct XRD patterns help to identify the phase quickly. Eu doped Y_2O_3 is known for its red luminescence. The luminescence observed is usually due to transition from $^5D_2$, $^5D_1$, $^5D_0$, to ^7F_J, ground level, $^5D_0$ to ^7F_J being the most dominant resulting in emission at 611nm. Since the emission of the Eu cation is affected by the host lattice, the emission was found to change with size and crystal phase for Eu:Y_2O_3 nano-particle.

5.2. Thermolysis of $Y(NO_3)_3$ powder

The study of thermal breakdown of $Y(NO_3)_3 \cdot xH_2O$ in air was conducted to determine the dynamics of formation of Y_2O_3. The reagent quality Yttrium (III) nitrate hydrate (Alfa Aesar #11187) was heated in an oven (Jelrus Temp-Master model 18000) at selected temperatures for the duration of 1 hour for each step. After each heating step the sample was ground and the powder XRD pattern was recorded. The measured XRD patterns are summarized in Figure 5.5.

The XRD pattern of $Y(NO_3)_3 \cdot xH_2O$ powder before heating showed that it contains $Y(NO_3)_3 \cdot 6H_2O$. Upon heating the sample dehydration occurred and the phases of $Y(NO_3)_3 \cdot 5H_2O$, $Y_2(NO_3)_6 \cdot 7H_2O$, $Y(NO_3)_3 \cdot 3H_2O$, and $Y(NO_3)_3 \cdot H_2O$ were the main phases detected for samples heated up to 300°C.

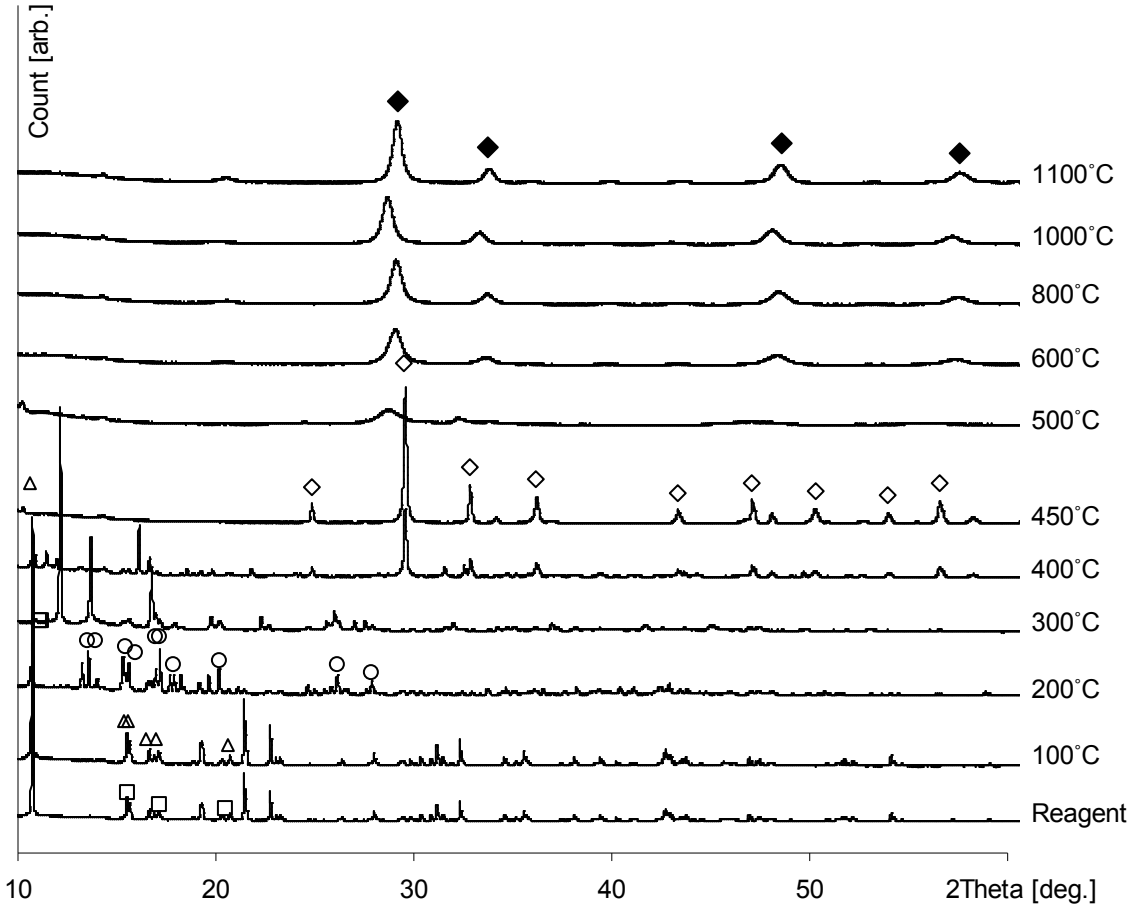

Figure 5.5. The powder XRD patterns of annealed $Y(NO_3)_3xH_2O$ reagent. Some of the XRD peaks of BCC Y_2O_3 (solid diamond), $YO(NO_3)$ (open diamond), $Y(NO_3)_3 \cdot 3H_2O$ (circle), $Y(NO_3)_3 \cdot 5H_2O$ (triangle), and $Y(NO_3)_3 \cdot 6H_2O$ (sqare) are marked.

The sample processed at 400 °C and 450 °C presented different picture. XRD pattern for this sample showed strong presence of tetragonal $YO(NO_3)$ suggesting that dehydration ended and thermal breakdown of $Y(NO_3)_3$ began. Upon further heating the $Y(NO_3)_3$ XRD pattern disappeared at 500 °C and broad peaks around 29° and 32° (2θ)

were observed. These peaks upon further heating had grown sharper and several other peaks evolved into the pattern representing the BCC phase of Y_2O_3.

This study suggest that the solution of $Y(NO_3)_3$ is appropriate for MPASD process where it is expected that the temperatures reach above 500 °C needed to synthesize Y_2O_3.

5.3. Deposition of Y_2O_3:Eu Coatings using MPASD System

The samples of Y_2O_3:Eu were deposited using the MPASD system. The precursor used during deposition was a solution of $Y(NO_3)_3xH_2O$ (Alfa Aesar #11187) and $Eu(NO_3)_3$ xH_2O (Alfa Aesar #15290) in water with the concentration of 0.0081 mol/L and 0.0009 mol/L respectively. Using equation 3.13, or easy to use Figure 5.6, the resulting particle size was expected to be 100 nm, and the resulting Y_2O_3:Eu particle to have 10% Yttrium replaced with Europium ($Eu_{0.2}Y_{1.8}O_3$)).

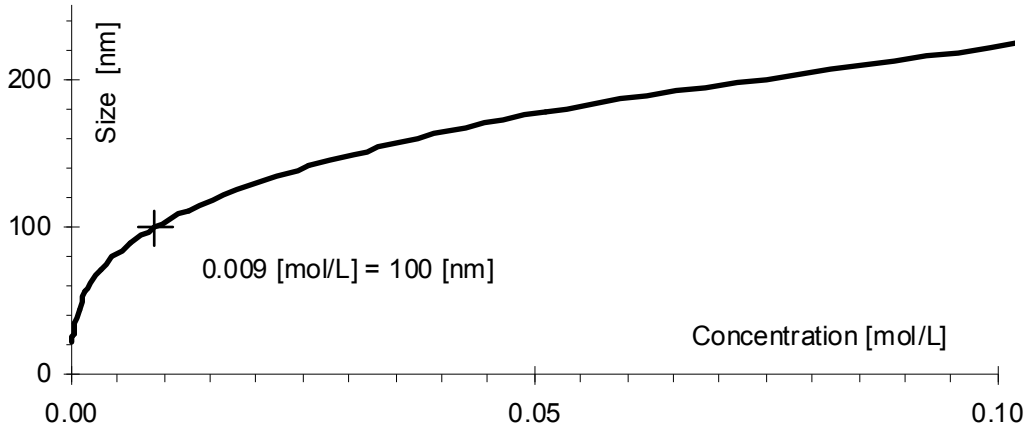

Figure 5.6. The processed nanoparticle size as a function of precursor concentration for MPASD system for Y_2O_3 process using $Y(NO_3)_3$ solution precursor.

Table 5.1. MPASD process conditions for Y_2O_3:Eu coating deposition.

Sample ID	Deposition pressure	Deposition power	Deposition O2 flow	Nebulizer duty cycle	Sample distance from plasma	Precursor Y concentration	Precursor Eu concentration	Comment
	Torr	W	Sccm	%	mm	mol/L	mol/L	
S1	20	200	700+18	2.5	80	0.0081	0.0009	Luminescence
S2	40	200	700+18	2.5	80	0.0081	0.0009	Luminescence
S3	60	200	700+18	2.5	80	0.0081	0.0009	Luminescence
S4	80	200	700+18	2.5	80	0.0081	0.0009	Luminescence
S5	100	200	700+18	2.5	80	0.0081	0.0009	Luminescence
S6	120	200	700+18	2.5	80	0.0081	0.0009	Luminescence
S7	140	200	700+18	2.5	80	0.0081	0.0009	Luminescence
S8	20	400	700+18	2.5	80	0.0081	0.0009	Luminescence
S9	40	400	700+18	2.5	80	0.0081	0.0009	Luminescence
S10	60	400	700+18	2.5	80	0.0081	0.0009	Luminescence
S11	80	400	700+18	2.5	80	0.0081	0.0009	Luminescence
S12	100	400	700+18	2.5	80	0.0081	0.0009	Luminescence
S13	120	400	700+18	2.5	80	0.0081	0.0009	Luminescence
S14	140	400	700+18	2.5	80	0.0081	0.0009	Luminescence
S15	20	600	700+18	2.5	80	0.0081	0.0009	Luminescence
S16	40	600	700+18	2.5	80	0.0081	0.0009	Luminescence
S17	60	600	700+18	2.5	80	0.0081	0.0009	Luminescence
S18	80	600	700+18	2.5	80	0.0081	0.0009	Luminescence
S19	100	600	700+18	2.5	80	0.0081	0.0009	Luminescence
S20	120	600	700+18	2.5	80	0.0081	0.0009	Luminescence
S21	140	600	700+18	2.5	80	0.0081	0.0009	Luminescence
S22	160	600	700+18	2.5	80	0.0081	0.0009	Luminescence
S23	40	800	700+18	2.5	80	0.0081	0.0009	Luminescence
S24	60	800	700+18	2.5	80	0.0081	0.0009	Luminescence
S25	80	800	700+18	2.5	80	0.0081	0.0009	Luminescence
S26	100	800	700+18	2.5	80	0.0081	0.0009	Luminescence
S27	120	800	700+18	2.5	80	0.0081	0.0009	Luminescence
S28	140	800	700+18	2.5	80	0.0081	0.0009	Luminescence
S29	60	1000	700+18	2.5	80	0.0081	0.0009	Luminescence
S30	80	1000	700+18	2.5	80	0.0081	0.0009	Luminescence
REF	70	700	700+18	2.5	80	0.0090	0	Reference Y_2O_3
G1	70	700	700+18	2.5	80	0.0090	0	Growth study
G2	70	700	700+18	2.5	80	0.0090	0	Growth study
G3	70	700	700+18	2.5	80	0.0090	0	Growth study
G4	70	700	700+18	2.5	80	0.0090	0	Growth study
G5	70	700	700+18	2.5	80	0.0090	0	Growth study
G6	70	700	700+18	2.5	80	0.0090	0	Growth study

The MPASD deposition condition is summarized in Table 5.1. During deposition oxygen was used for the main and nebulizer flow. The gas flow is noted as shield gas flow "+" nebulizer gas flow. For example, if shield gas flow is 700sccm and nebulizer gas flow is 18sccm then the gas flow will be written as 700+18sccm.

The generation power of the nebulizer was controlled using the circuit described in Appendix A. All samples in the power versus pressure study were deposited at the same operating conditions of MPASD except that the microwave power and process gas pressure were varied and the location of the waveguide short position was adjusted for each power and pressure setting in order to localize the plasma discharge within the discharge tube.

5.4. Morphology of Y_2O_3:Eu Coatings

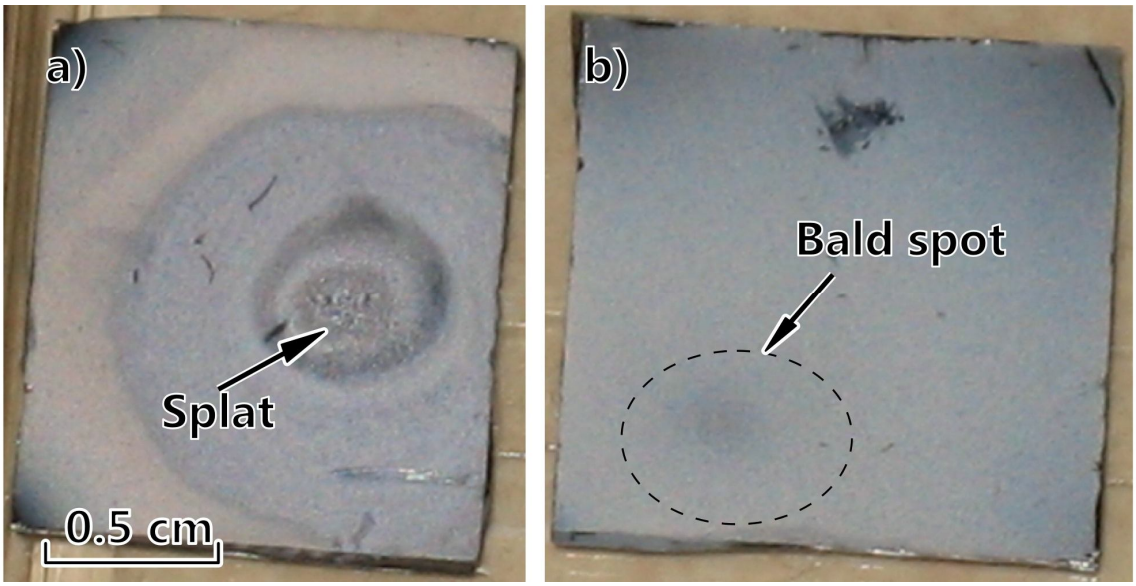

Figure 5.7. Picture of selected coatings. Samples S15 (a) and S16 (b) are shown.

The as-deposited samples were inspected visually for the coating quality. The coatings deposited at pressures of 20Torr had poor surface quality with uneven coating

and many visual blemishes. On the other hand, the coatings deposited at pressures of 40 Torr and above appeared to have smooth surface with only single spot blemish as it is presented in Figure 5.7. These coatings were easily disturbed and could be removed from the substrate by a gentle wipe down. In addition, the samples deposited at pressures of 120 Torr and above had either a very thin or no coating.

Further investigation of the coating using SEM showed that the samples deposited under 20 Torr of pressure did not have the desired nanoparticles. These samples had a solid thick film with an uneven surface (Figure 5.8a). On the other hand the samples deposited at pressures of 40 Torr and above had a smooth coating that was composed of nano-particles and some sub-micron sized particles (Figure 5.8b, c, and d).

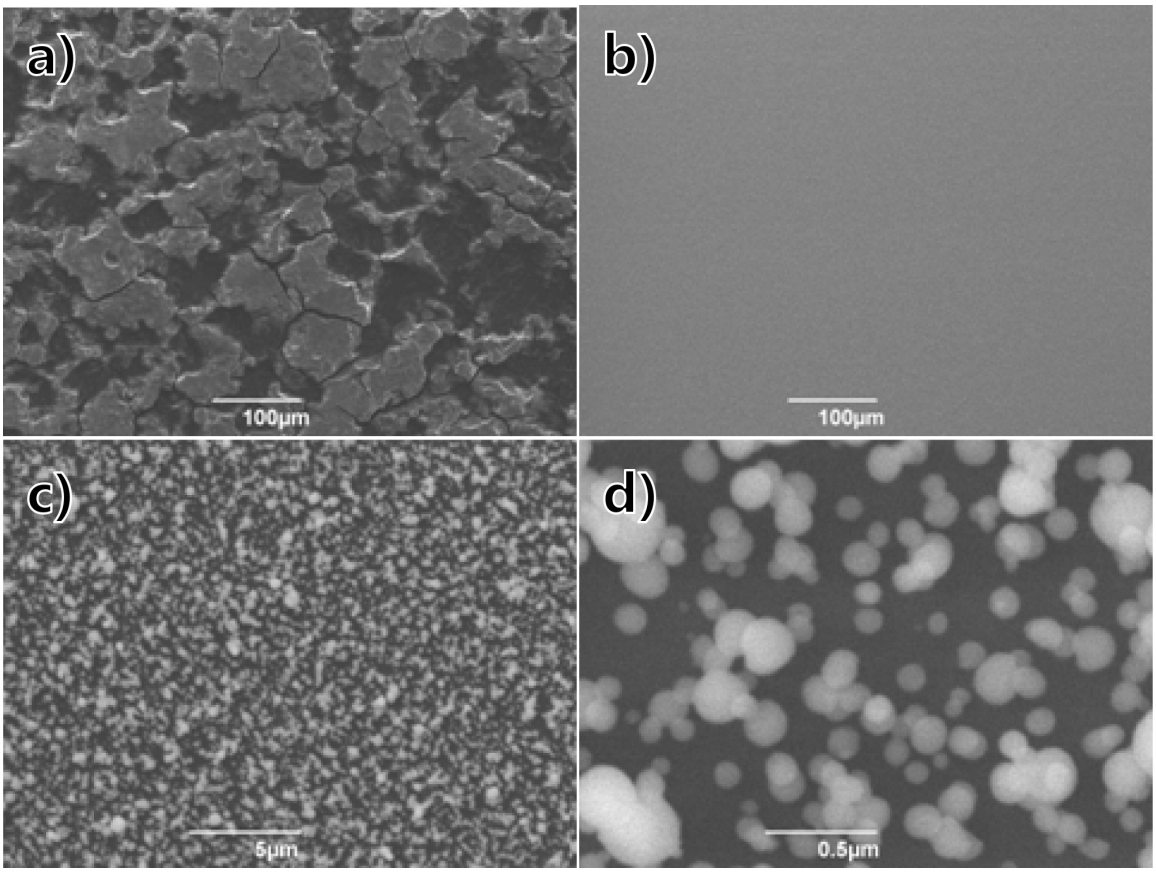

Figure 5.8. SEM images of coatings deposited at (a) 20 Torr and (b, c, d) 60 Torr. The coating deposited at 60Torr is shown at three magnification levels. Samples S15 (a) and S16 (b, c, d) are shown

One feature worth notice was a small patch, usually in the center of deposition, where the deposition was thinner. The analysis of the thinning, or bald spot, of the coating is presented in Figure 5.9. Each image was taken in 1 mm intervals sweeping across the bald spot, which clearly shows a sparser deposition in the center of the bald spot.

The bald spot can be explained by looking at the possible flow patterns of the gas as it exits the plasma zone. The bald spot is more apparent at low pressure depositions than at higher pressure depositions. For the low pressure depositions the velocity of the gas, under same mass gas flow, is higher than for high pressure depositions. Assuming the same temperature and same mass gas flow the velocity of the gas will be twice as high at 40 Torr as at 80 Torr. As a result, the fast moving gas blows off the coating in the center of the sample.

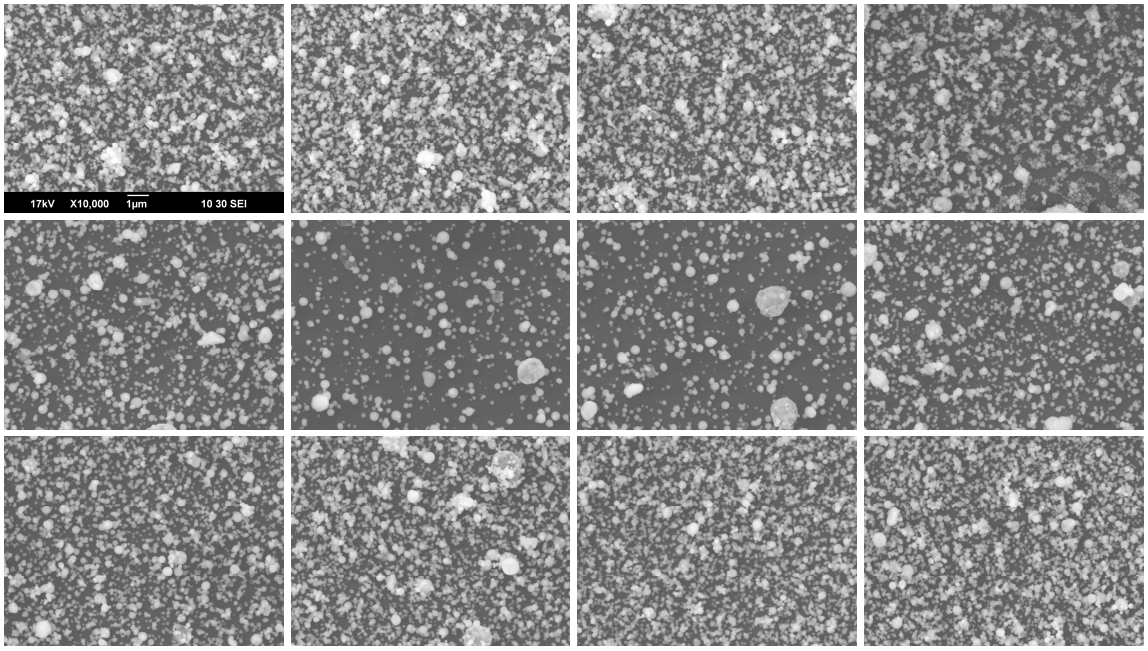

Figure 5.9. SEM images of a coating and the bald spot on the coating. The images were taken at same magnification and 1mm apart. Sample S16 is shown. The images were taken at same magnification and 1mm apart.

The presence of large particles can be contributed to size distribution of the nebulizer droplet generation and to atomized droplet collision before pyrolysis.

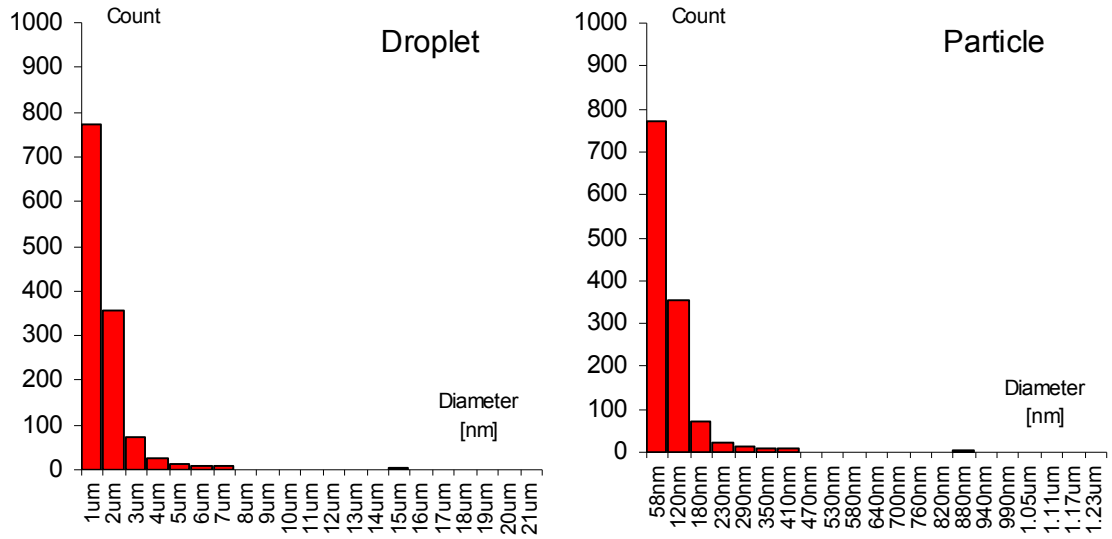

Figure 5.10. The droplet and resulting calculated particle size distribution. Data for droplet size distribution supplied by manufacturer.

The nebulizer data shows that the droplet size distribution will result in some large particles (Figure 5.10). The data shows that most particles fall in the 60 nm, and 120 nm statistical bins, but particles with sizes larger than that account for 10% of the particles count. Particles with sizes up to 1.2 μm can be expected from the statistical distribution of the nebulizer since droplets of 21 μm are found.

The TEM and STEM images (Figure 5.11. and 5.12) show that the deposited coatings are composed of spherically shaped particles. Many particles are in contact with each other, but do not appear to be bonded to each other

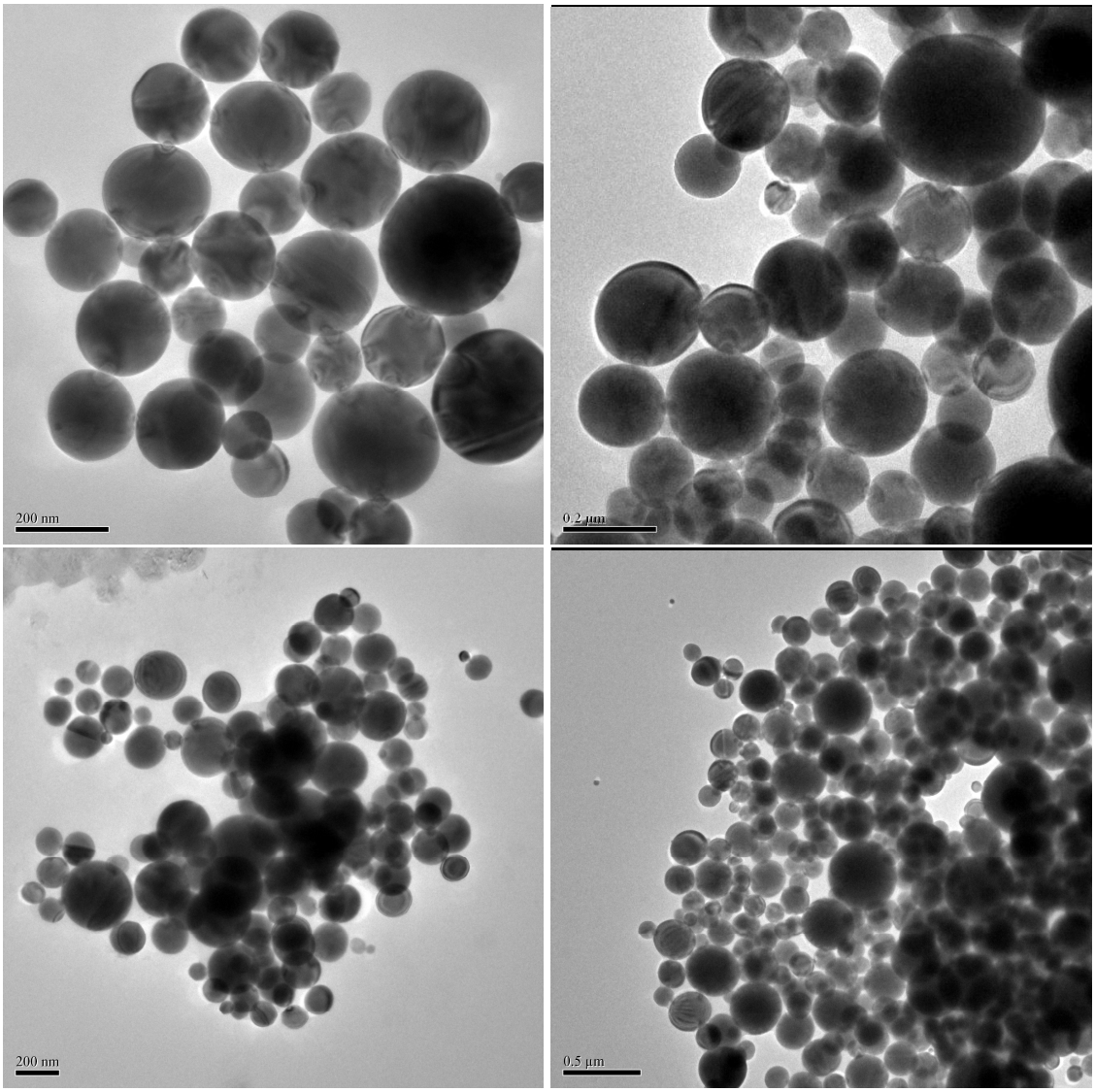

Figure 5.11. The TEM image of several particle clusters from Eu:Y_2O_3 nanoparticle coating.

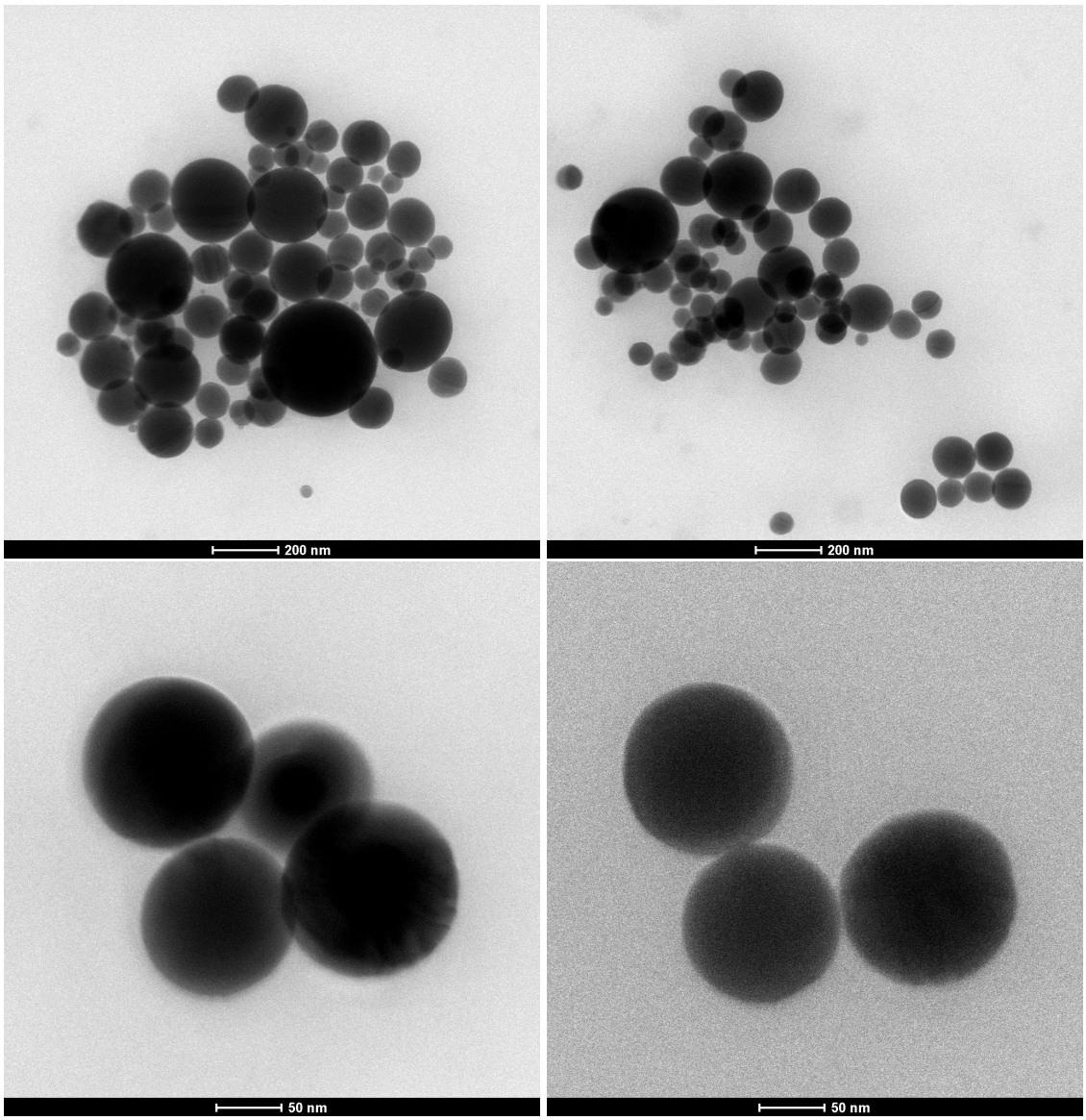

Figure 5.12. The STEM image of several particle clusters from Y_2O_3:Eu nanoparticle coating.

The TEM and STEM images presented in Figure 5.11 and 5.12 show that the particles in the deposited coating have a size distribution. An analysis of diameters of 120 particles is summarized in Figure 5.13. The largest particle found in the data set was 329nm and the smallest was 44nm. The average, median, and mean volume diameter are 151nm, 143nm, and 169nm respectfully. Although the mean particle diameter calculated from the precursor chemistry and the nebulizer is 100nm the distribution shown in Figure

5.13 is skewed toward larger diameters and peaks for particles in the 125nm bin. This could be due to the assumptions made about the precursor solution surface tension, density, and viscosity during calculation (Equation 3.13). In this calculation the surface tension and viscosity was assumed to be the same as of pure water and the actual the values for the precursor could account for the discrepancy between the calculated and the observed diameters.

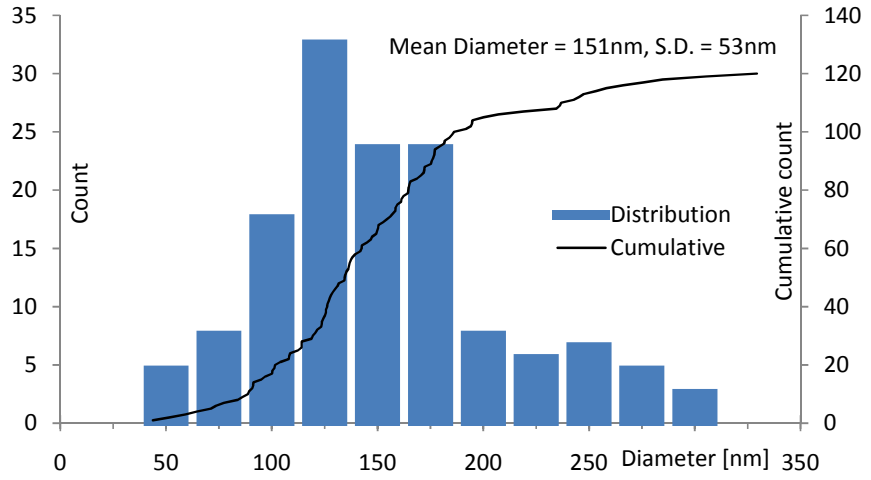

Figure 5.13. The histogram of particle size distribution of Eu:Y_2O_3.

The nebulizer operating frequency affects the droplet size. The actual operating frequency was not measured and its value could be different from the value advertised by nebulizer manufacturer, affecting the deposited coating's mean particle diameter.

In addition, the collisions of precursor droplets increase the final particle size. As the atomized droplet is moved toward the plasma zone, each collision between two droplets creates one larger droplet with volume that is a sum of the initial droplets. This will skew the statistical distribution toward larger sizes for the deposited particles.

If two droplets of 1.7um diameter collide, this would result in two 100nm particles collide, then the resulting particle size increases to 125nm. The particle size

after eight 1.7 um droplets collide will result in processed particle diameter of 200nm. These collisions could play large role in the distribution peak shift toward larger diameters in the statistical distribution shown

The statistical distribution of generated droplets is inherent to the atomization techniques and any improvements in this distribution would require redesign of the atomizer. However, the particle size distribution shift toward larger particles due to droplet collisions could can be addressed.

The number of the collisions mainly depends on droplet concentration in the material flow and the time that it takes the droplet to reach plasma zone. Both parameters can be regulated by changing the nebulizer gas flow, changing the process pressure, and changing the nebulizer generation rate. Increase in gas flow or decrease in process pressure decreases both concentration and transit time. The decrease in nebulizer generation rate decreases the concentration of particles in nebulizer flow.

5.5. Growth Rate Study of Y_2O_3:Eu Coatings

In order to determine the growth rate of the MPASD process several depositions of Y_2O_3 were performed and the coatings were analyzed using SEM. Each deposition was performed under same process conditions but with different deposition times.

Six depositions with deposition times varying from 30 seconds to 16 minutes were analyzed using SEM to make qualitative and quantitative observations. All samples were deposited at an 80 torr process pressure, 700 W absorbed microwave power, 500 sccm and 18 sccm of oxygen flow through the sheath and nebulizer nozzle, respectfully, and 2.5% nebulizer duty cycle.

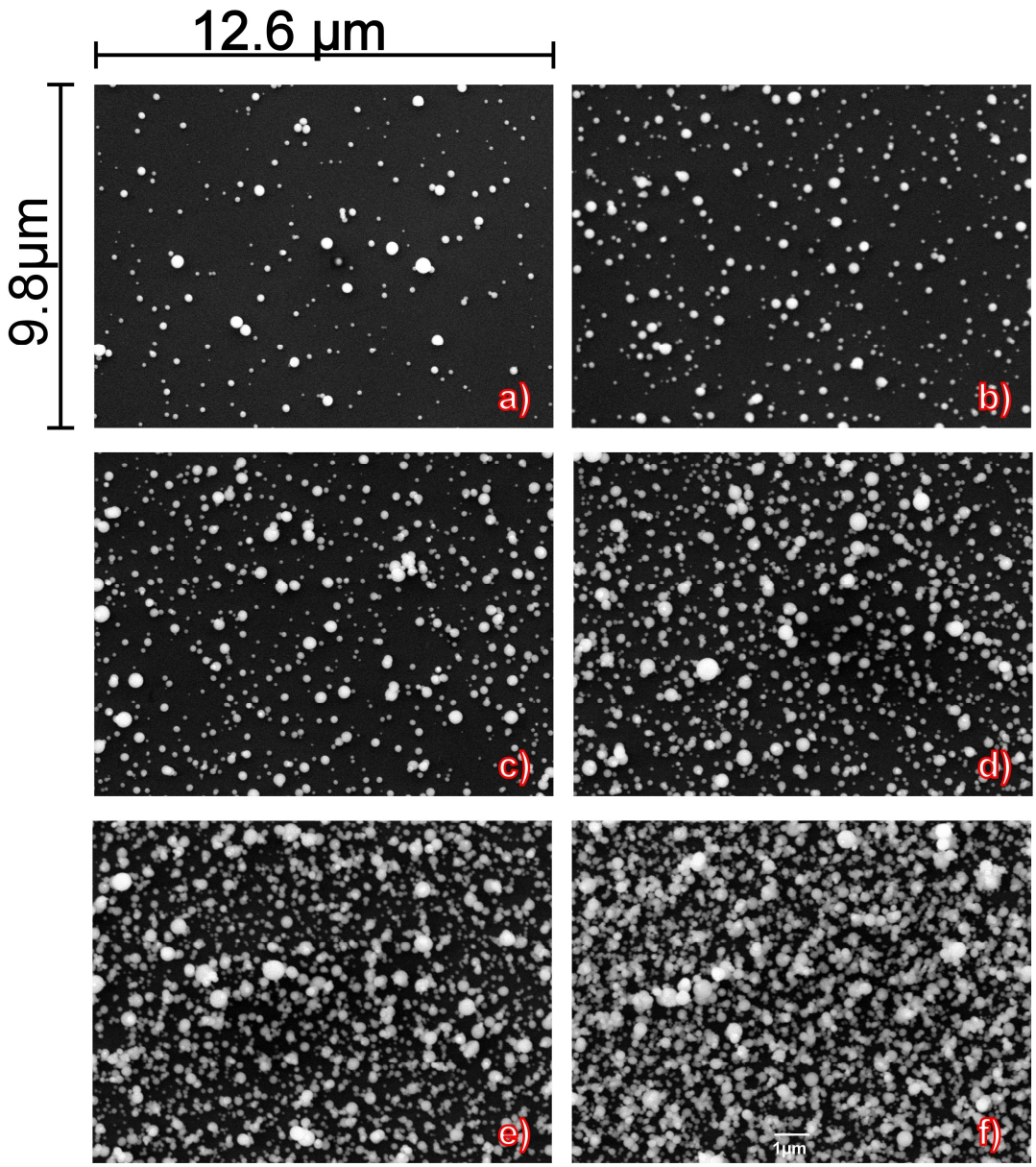

Figure 5.14. SEM images of Y_2O_3 coating deposited for (a) 30s, (b) 1min, (c) 2min, (c) 4min, (d), 8min, and (f) 16min.

The SEM images of the deposited samples are shown in Figure 5.14. Clearly, the thickness of the coating increased with longer deposition times. Usual methods of measuring thickness of a coating utilize contact probe profiling, noncontact AFM technique, x-ray reflectometry technique, elipsometry techniques, thin film interference techniques, and SEM cross section imaging. Unfortunately, the nature of the deposited

coatings did not allow one to utilize any of the standard techniques. Nevertheless, a method to estimate the coating growth rate was needed.

A method of measuring the observed coating coverage area was utilized to estimate the coating growth rate. In this technique the SEM high contrast images were taken resulting in high contrast, black and white images (Figure 5.15b). The white features of the image are due to the deposited particles while the black areas represent the uncoated substrate. The coating percentage area coverage was taken to be the ratio of white pixels to number of the image pixels.

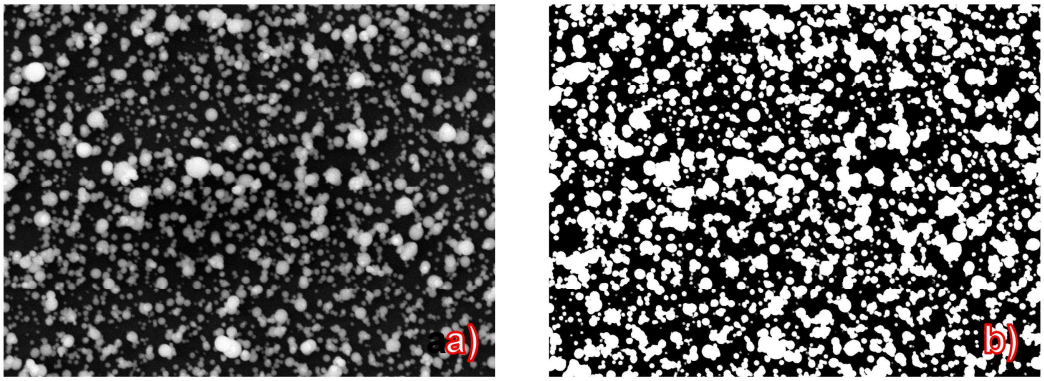

Figure 5.15. The normal (a) and high contrast (b) image of Y_2O_3 coating deposited for 16 minutes. The observed area coverage was 41%.

The coatings made during short depositions have the characteristic of being sparse with particles separated from each other and with very few agglomerations. However, for the depositions of 4 minutes and longer there is a significant agglomeration of particles resulting in part of the particles resting on top of the other. This agglomeration is undesired. If a particle was located atop of another then the observed coating coverage appeared to be lower than it actually was.

The calculated coverage values are presented in Figure 5.16. Assuming constant growth rate and non-overlapping coating the data should have a linear trend. From the

graph it is clear that the data has a nonlinear behavior. This behavior can be explained by noticing that for the samples with long deposition times some coating particles are resting on top of others. This causes some of the particles to be obstructed by other particles on the SEM image. The coating area coverage calculations for these overlapping particle images will incorrectly under estimate the coating growth rate.

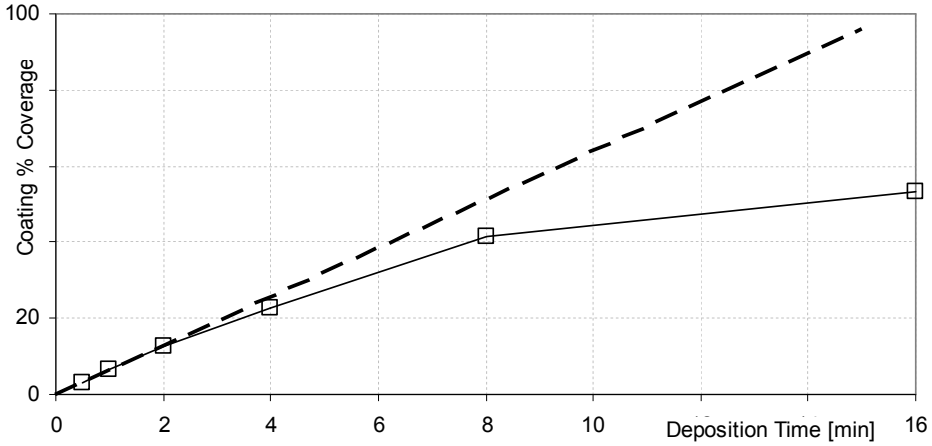

Figure 5.16. Observed coating percentage coverage as a function of time for deposition of Y_2O_3 coating (solid line). The dash line represents the calculated 6.4%/min growth.

In order to reduce the effect of particle overlap on the result of the growth rate estimation, only the coatings with short deposition times (<2 min) were utilized in the calculation. In addition, it was assumed that coating coverage was 0% at the start of the deposition. Under these assumptions of the deposition it was found that the coating area coverage rate is 6.4%/min.

The nebulizer manufacturer specified that the area mean diameter of the precursor droplet to be 1.41 m and volume mean diameter to be 1.79 m. This allows calculating the number of particles and coating volume based on area of coverage. Given the area coverage growth rate and volume mean diameters, the equivalent volume film thickness growth rate is comparable to 100 nm/min growth rate of a solid film.

5.6. Crystal Structure Study of Y_2O_3:Eu Coatings

X-Ray diffraction (XRD) and electron diffraction can help to determine crystal structure, chemical makeup, phase, crystal orientation, residual stresses, and crystallite size for powder samples. The XRD and selective area electron diffraction (SAED) techniques are utilized to study the crystal structure of the deposited coatings. In addition, the high-resolution transmission electron (HRTEM) imaging was utilized in this crystal structure study.

The powder XRD (θ - 2θ) technique allowed crystal identification as well as qualitative determination of lattice constant and crystallite size. The crystal structure was determined by comparison with the published crystallographic database.

Table 5.2. X-Ray diffraction parameters for θ-2θ scans

XRD model	Bruker AXS D8
Monochromator model	K-FL-Cu-2k with 0.4mm slit
Source aperture	0.4 mm
Divergence apreture	1.0 mm
Generator setting	40 kV, 40 mA
Goniometer type	200mm Brag-Brentano circle
Detector model	LynxEye, 192 x 75um detectors
Incident aperture	2.5° soller slit with Ni Kb fiter and optional 8mm slit
Scan type	θ-2θ scan

XRD data was collected using Bruker AXS diffractometer equipped with 2 kW Copper anode X-ray source, and the high speed LynxEye X-ray detector, on a 200 mm Brag-Brentano circle goniometer. The XRD pattern analysis was performed with the help of DiffracPlus EVA software from Bruker AXS that incorporated the PDF2 2005 release database for XRD pattern matching.

Figure 5.17 shows selected XRD patterns for substrate and samples deposited at pressures of 20 Torr and 40 Torr. The marked peak locations of corresponding base centered monoclinic phase of Y_2O_3. The results of this study had shown that samples deposited at pressures of 40 Torr and above are consistent with base centered monoclinic phase of Y_2O_3 and Eu doped Y_2O_3. On the other hand the samples deposited at a pressure of 20 Torr had not shown any presence of Y_2O_3.

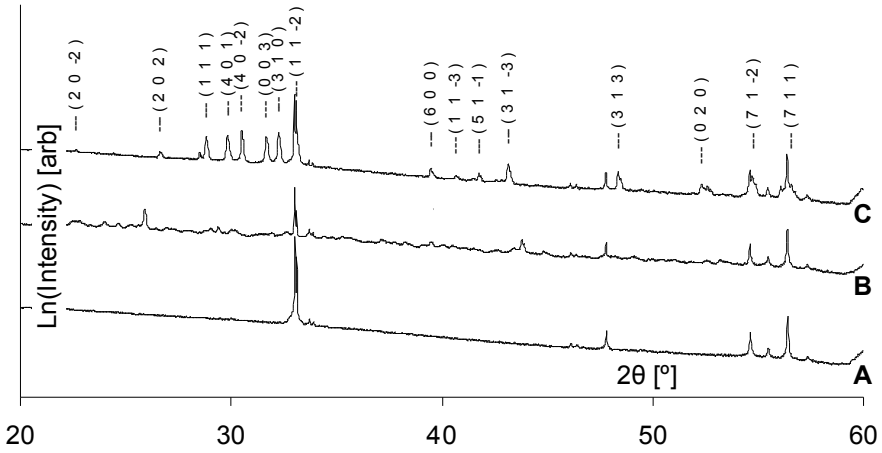

Figure 5.17. The powder XRD pattern of (a) Si 100 single crystal substrate and Y_2O_3:Eu sample deposited on Si (100) substrate under pressure of (b) 20Torr and (c) 40Torr. The diffraction peaks of monoclinic phase of Y_2O_3:Eu are marked.

It is known that the crystal size affects the x-ray diffraction. The finite size if a crystal causes a broadening of the x-ray peak and the broadening can be described using the Sreerrer equation

$$\beta_{hkl} = \frac{k \cdot \lambda}{L_{hkl} \cdot \cos(\theta_{hkl})} \tag{5.15}$$

Using this relation and the XRD data collected the calculations of the particle diameter were conducted for samples where the XRD pattern signal was strong. The diameter measurement for each sample was based on the XRD peak broadening for the (111), (401), $(40\bar{2})$, (003), (310), and $(31\bar{3})$ peaks. The results for the selected planes were

averaged and the deviation calculated. The results of the calculation are summarized in Table 5.4.

The calculations show that the crystal size was between 88 nm and 159 nm. There is no observable power or pressure dependence of the crystallite size. The observed particle sizes are consistent with the diameter 100 nm calculated using equations 3.13 and given precursor chemistry and concentration.

Table 5.3. The particle diameter calculation results using the broadening of XRD diffraction peaks for selected samples.

Deposition Power [W]	Deposition Pressure [torr]	Measured Diameter [nm]	Diameter Deviation [nm]
400	40	100.7	9.0
400	40	153.1	30.4
400	60	148.2	19.2
400	80	139.0	21.6
400	100	159.7	45.3
600	60	88.2	7.9
600	40	107.3	8.3
600	60	116.7	17.2
600	80	139.4	15.2
600	100	148.8	31.3
800	80	95.7	7.1
800	40	108.3	7.6
800	60	113.7	7.5
800	80	135.9	19.7
800	100	131.8	26.0
1000	60	97.8	10.1
1000	60	106.8	12.9
1000	80	137.9	23.4
400	40	100.7	9.0

The powder XRD measurements allow for analysis of the coating as a whole, while the HRTEM with SAED allows verifying the structure of single particle within the coating.

The Figures 5.18, 5.19, and 5.20 present the HRTEM image of single nanoparticle of Y_2O_3:Eu.

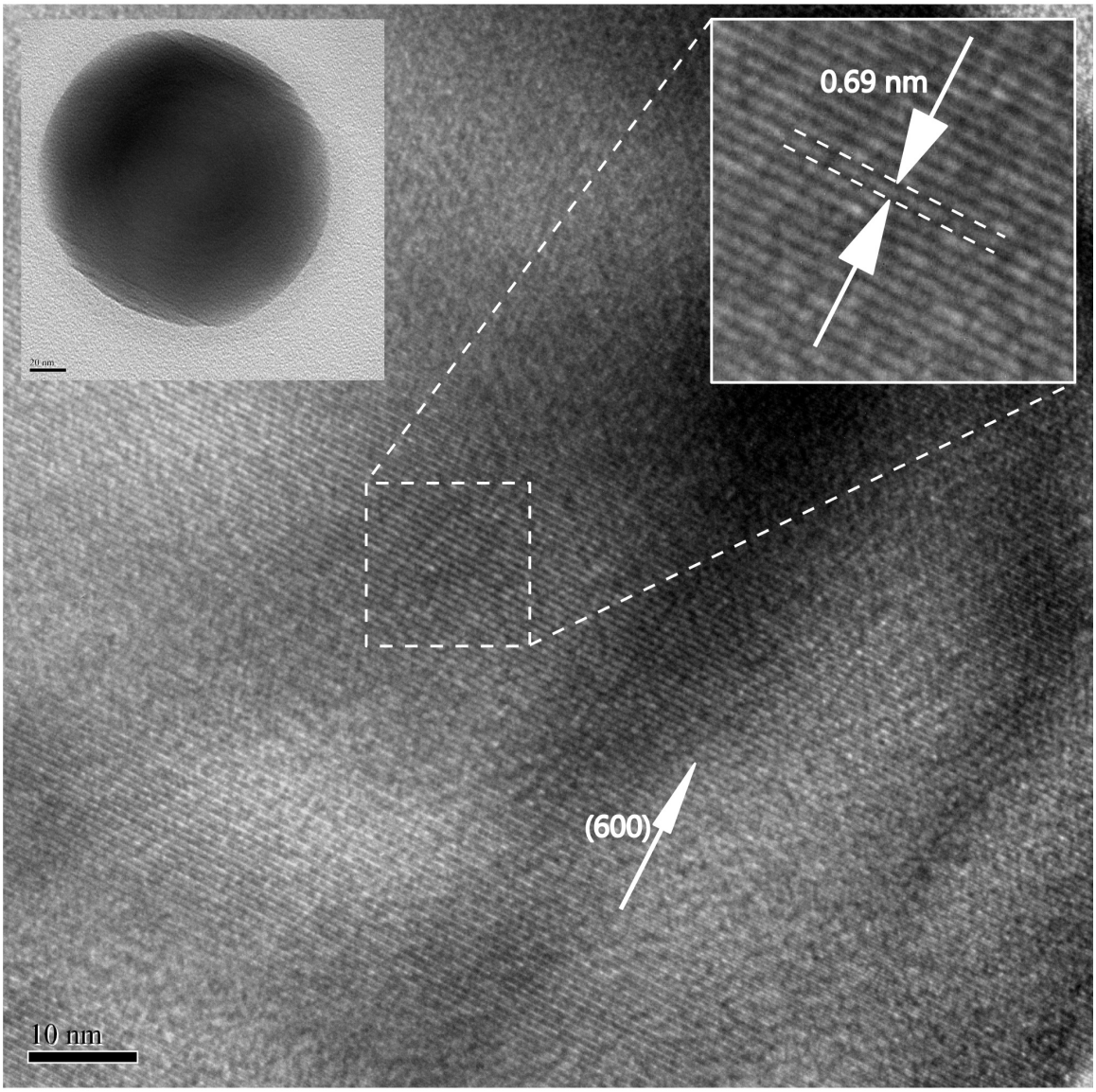

Figure 5.18. The HRTEM image of Y_2O_3:Eu nanoparticle. The observed interplanar spacing is 0.69 nm.

The interplanar distance found to be 0.69 nm, a value consistent with (6 0 0) plane being in focus of the HRTEM image. This measurement was verified in three locations of the particle.

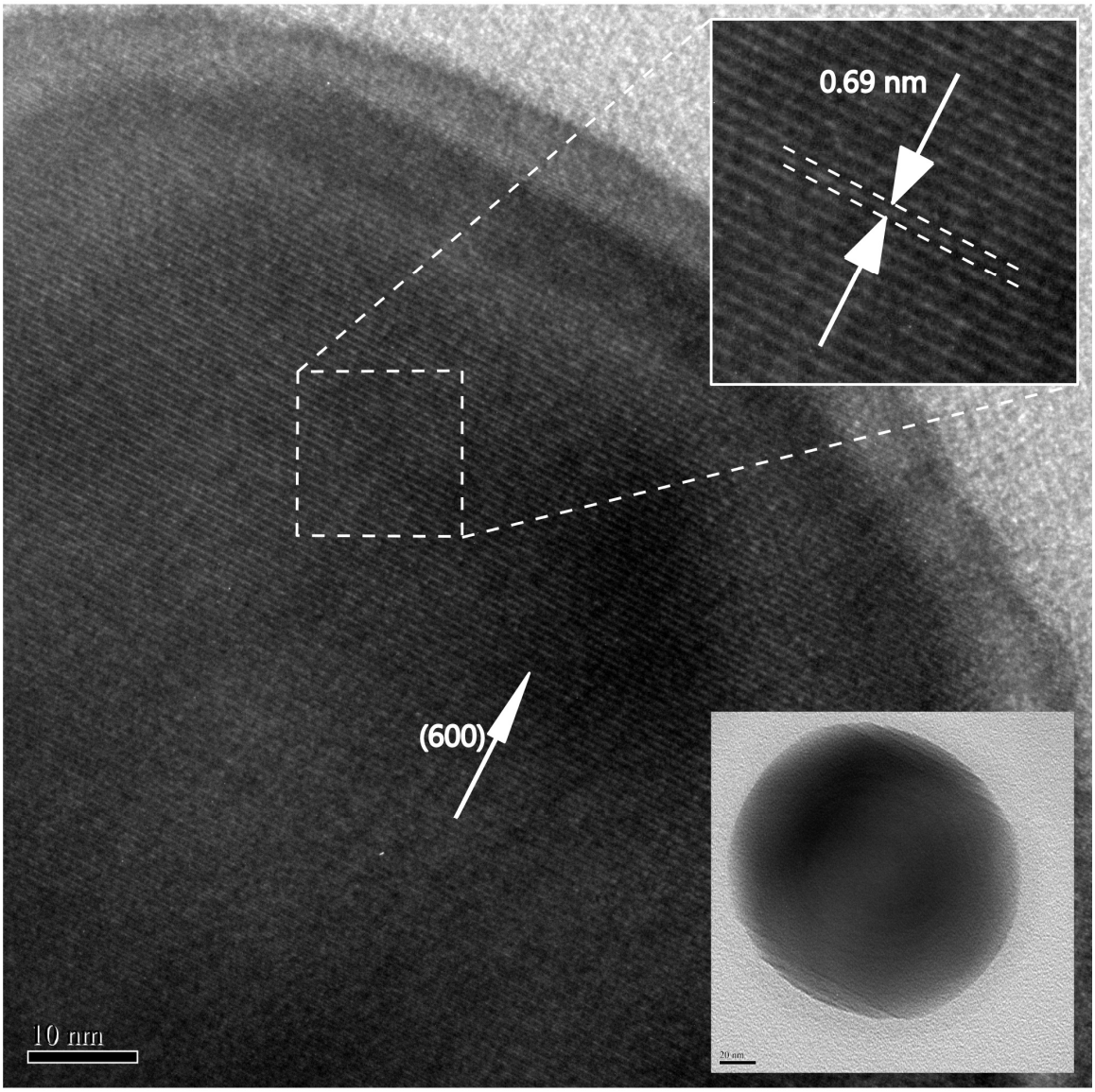

Figure 5.19. The HRTEM image of Y_2O_3:Eu nanoparticle. The observed interplanar spacing is 0.69 nm.

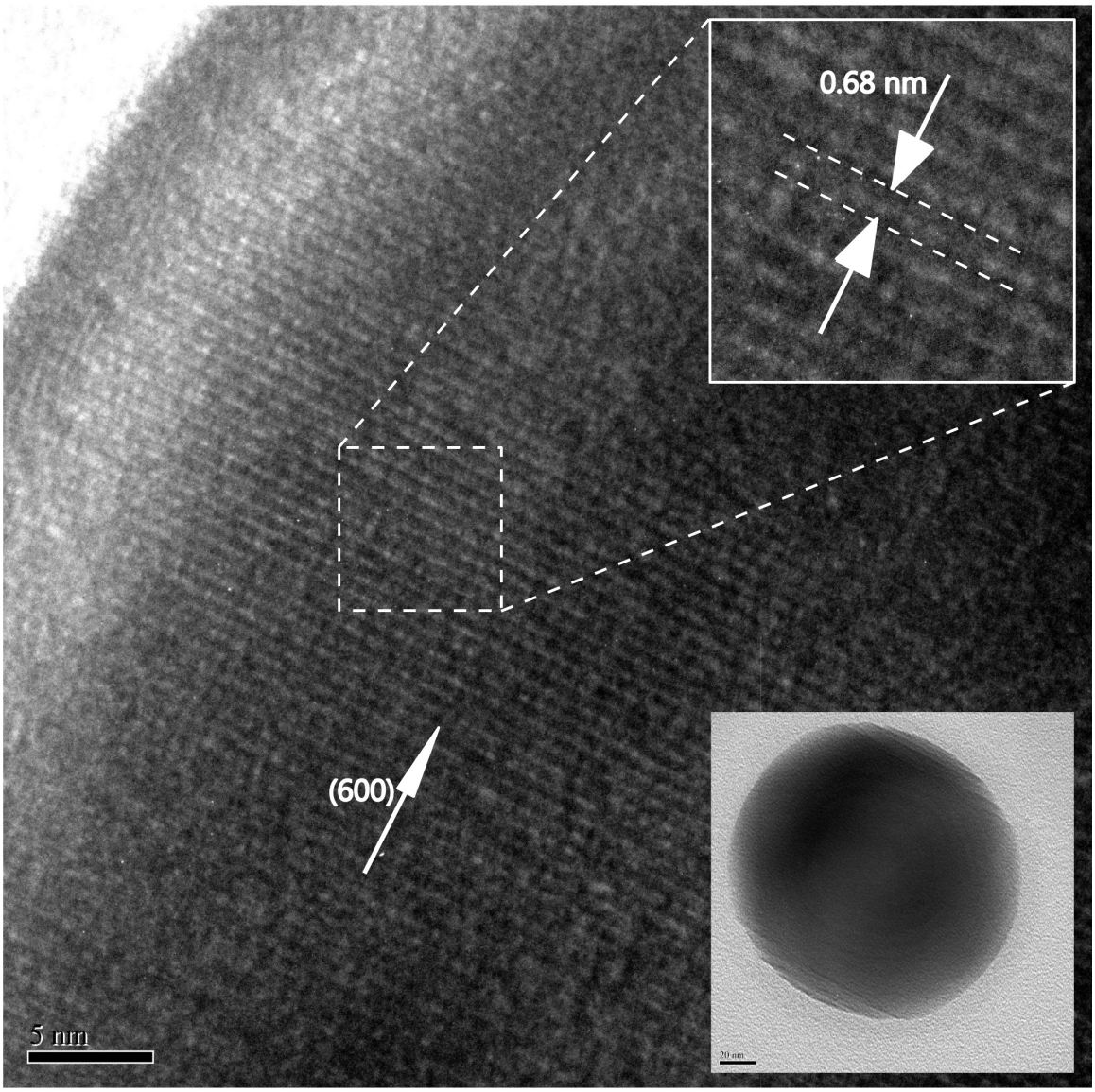

Figure 5.20. The HRTEM image of Y_2O_3:Eu nanoparticle. The observed interplanar spacing is 0.68 nm.

Figure 5.21 presents the HRTEM image of another Y_2O_3:Eu particle. The orientation of this particle differs from the orientation of the particle from Figures 5.18, 5.19, and 5.20. The observed interplanar distance is found to be 0.37nm suggesting that the image shows the (1 1 -2) plane of Y_2O_3:Eu crystal. The SAED diffractogram for this particle is shown.

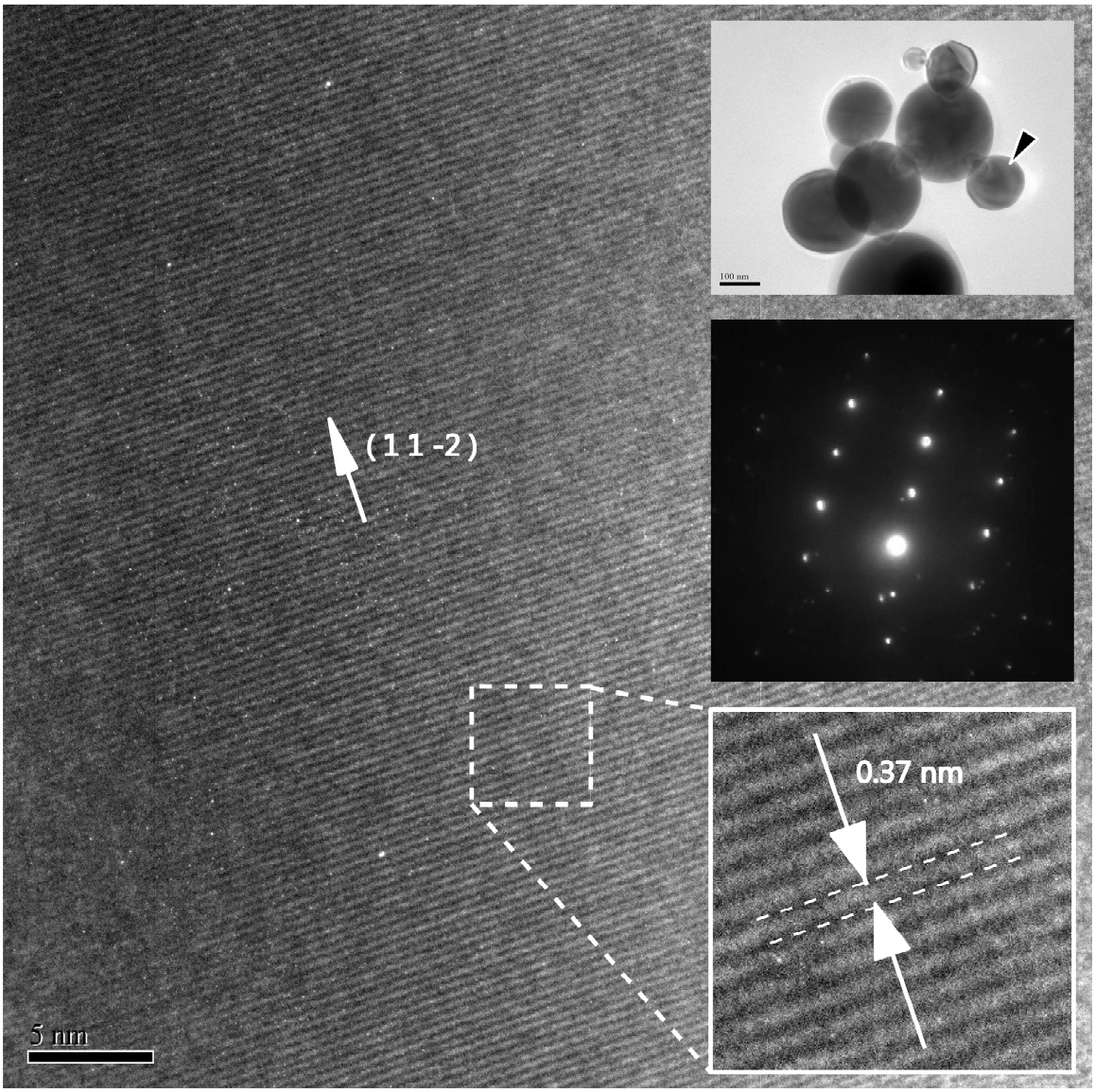

Figure 5.21. The HRTEM image of Y_2O_3:Eu nanoparticle. The observed interplanar spacing is 0.37 nm. The insert shows the SAED diffractogram.

5.7. The energy-dispersive X-ray spectrum of Y_2O_3:Eu coatings.

The TEM utilized allowed to perform energy-dispersive X-ray spectroscopy (EDS) measurement. The results of this measurement are shown in Figure 5.22.The Eu signal verifies that the particle is doped with Eu. The EDS

measurement allowed to measure the spectrum from small area of just four particles.

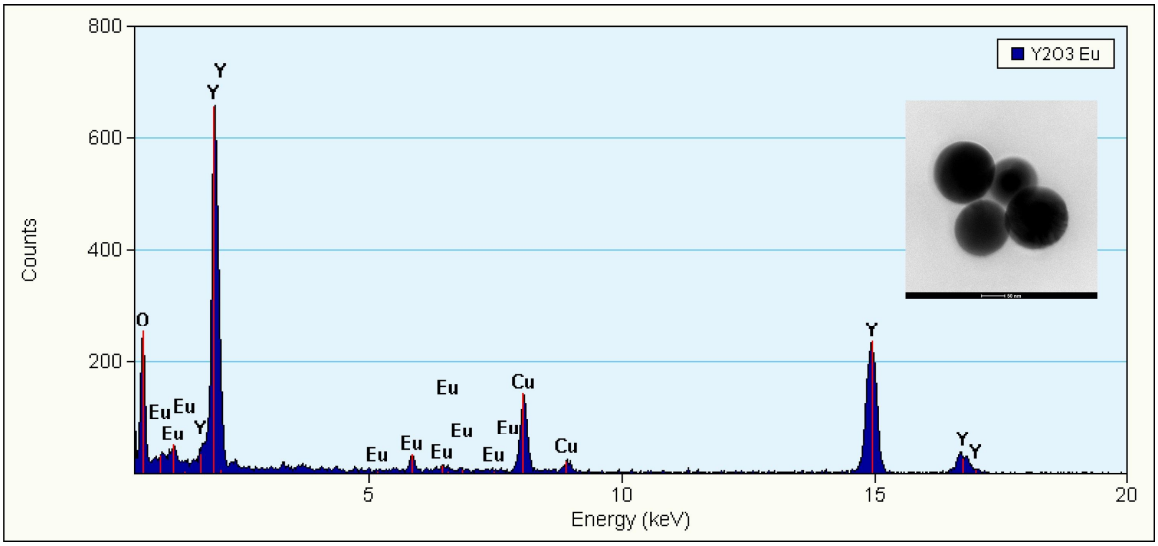

Figure 5.22. The energy-dispersive X-ray spectrum of small cluster of Y_2O_3:Eu particles.

However, the instrument utilized did not allow to perform quantitative analysis of the sample. Namely, the doping level of the Eu in the particles was not determined.

5.8. Anneal Study of Y_2O_3:Eu Coatings

The base centered monoclinic phase of Y_2O_3:Eu is a high pressure stable phase for bulk material while cubic phase is the energetically favorable phase. The most common phase of Y_2O_3:Eu is the BCC phase. In an attempt to obtain the BCC phase of Y_2O_3:Eu an anneal study on one sample was performed and the SEM images, and the XRD profile was recorded at five annealing temperatures. Each annealing step was done in Jelrus Temp-Master M model 18000 oven in air environment for the duration of 2 hours. Additionally, the annealing was repeated for the 1100 °C annealing for an additional 72hrs.

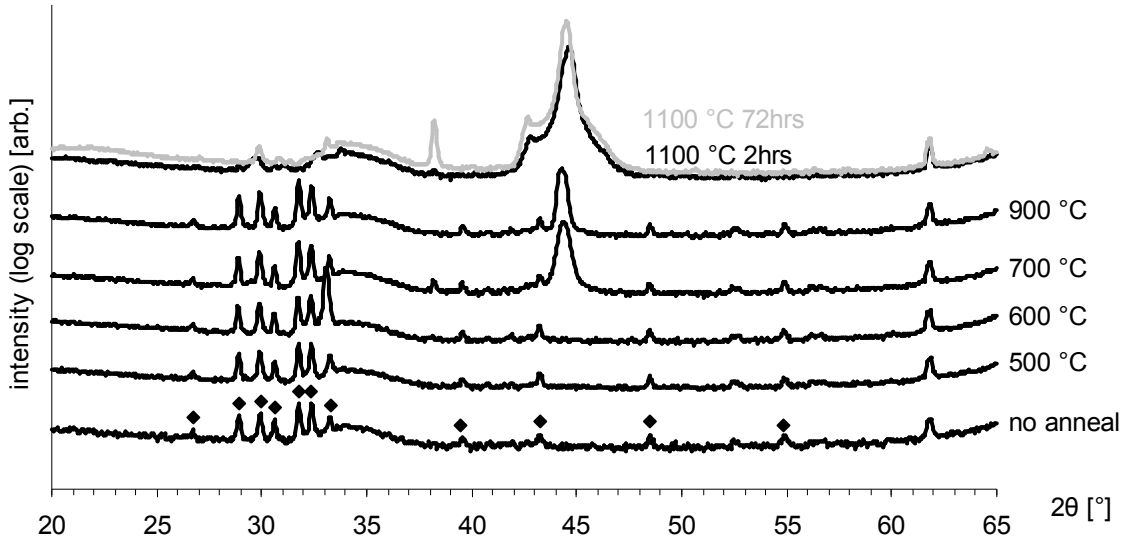

Figure 5.23. The XRD patterns for sample of Y_2O_3:Eu annealed at selected annealing temperatures. The diamond markers point to the characteristic XRD peak locations of base centered monoclinic phase of Y_2O_3:Eu.

The measured XRD patterns are presented in Figure 5.23. The monoclinic phase is present in all samples annealed at temperatures of 900 °C and below. However, at a temperature of 700 °C, there is an additional broad peak at 45° that is not consistent with the monoclinic, cubic, or even hexagonal phase of Y_2O_3:Eu. Annealing at the temperature of 1100 °C has destroyed the monoclinic phase: the characteristic peaks of monoclinic are absent in the sample annealed at 1100 °C, nor was the cubic phase of Y_2O_3:Eu observed.

5.9. Photoluminescence of Y_2O_3:Eu Coatings

The Eu doped Y_2O_3 crystal has been observed to luminescent in the red part of the visible spectrum. In order to verify this phenomenon a photoluminescence experiment was conducted.

A preliminary study utilizing the 410 nm wavelength laser and the set of 425, 420, 415, 405, 400, and 395 nm LED's showed no luminescence for all of the samples. This is consistent with published results for the monoclinic Y_2O_3:Eu that have shown that the absorption occurs around 250 nm. Therefore, the study utilizing a UV source was conducted.

The experimental setup utilizes a UV light source, short-pass filter, sample to be tested, long-pass filter, spectrometer, and computer with A/D acquisition card and custom software. The diagram below shows the basic arrangement of experimental setup.

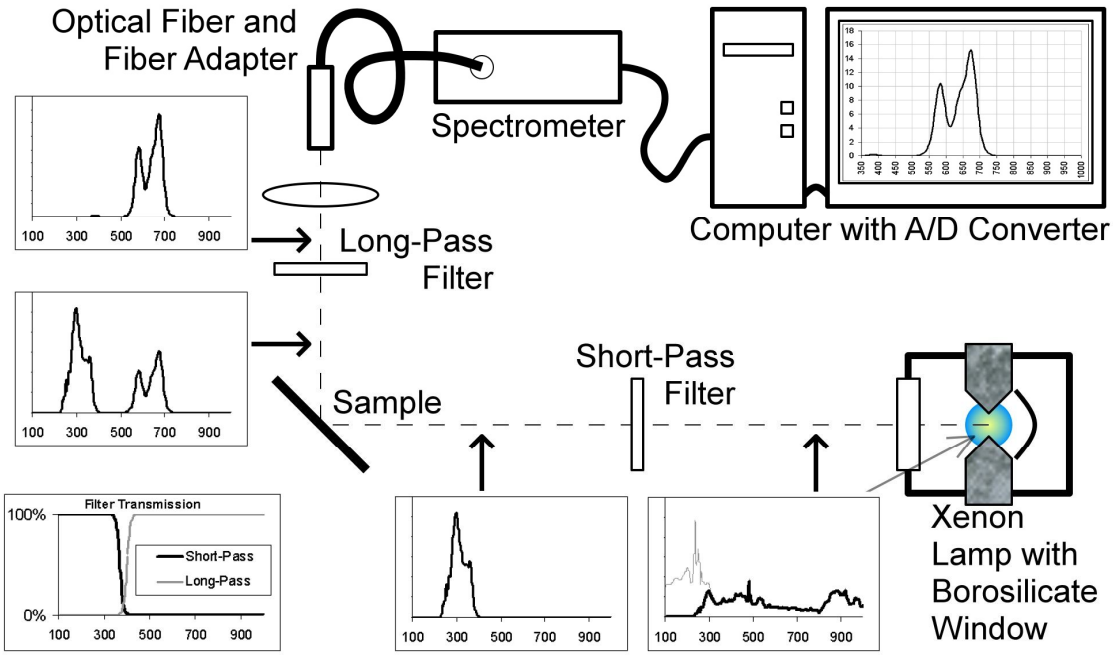

Figure 5.24. Photoluminescence experiment setup diagram

The UV light source utilized was a xenon short arc flash lamp with a borosilicate window (Perkin Elmer FX-1163). Although xenon arc lamps are capable of producing deep UV light, the construction of the arc lamp used, namely the borosilicate window of the lamp, limited the usable UV spectrum to wavelengths longer than 225nm.

The sample tested was exposed to UV radiation with the spectral profile controlled by the short-pass filter. The transmission spectrum of the short-pass filter is chosen as to prevent overlapping of the excitation signal and the photoluminescence signal of the sample.

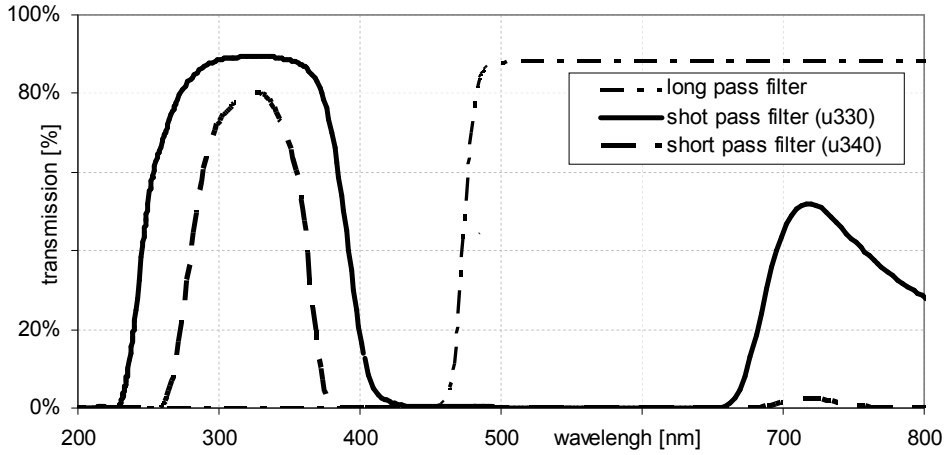

Figure 5.25. Transmission spectrum of filters utilized in the luminescence experiment.

The short-pass filters used in the experiment were the Hoya u330 and u340 glass. Although these filters have the desired UV characteristics, the visible and NIR transmission of the filters prevents the measurement of luminescence in the deep red range and NIR range. This is presented in Figure 5.25.

The photoluminescence signal of the sample was filtered using the long-pass filter with measured spectral profile shown in Figure 5.25. The long-pass filter helps to reduce the stray light signal in the spectrometer due to excitation light entering the spectrometer.

The light collected by the optical fiber was analyzed using a spectrometer (Ocean Optics model S2000) capable of spectrally resolving the light in the range of 350 nm to 1100 nm with a detector resolution of 0.36 nm/pixel and effective optical FWHM resolution of 9 nm. The spectrally resolved signal from the spectrometer was recorded on

the computer for further analysis with the help of an analog to digital acquisition card (National Instruments PCI-6251) and custom program written utilizing LabView software.

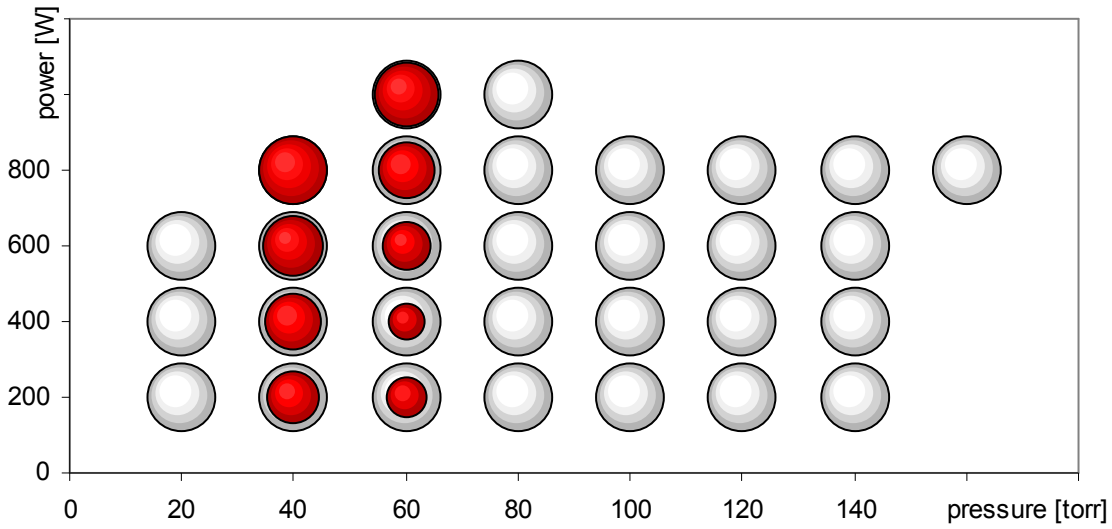

Figure 5.26. The power and pressure conditions for the thirty samples tested. The red bubble represents the photoluminescence detected. The varing red area represents the relative intensity of photoluminescence.

Thirty samples were analyzed for luminescence. Each sample was deposited using MPASD under different pressures and power while keeping other deposition conditions constant. The power was varied from 200 W to 1000 W absorbed power and the deposition chamber pressure was varied from 20 Torr to 160 Torr. Figure 5.25 presents each sample location on the Power – Pressure plane.

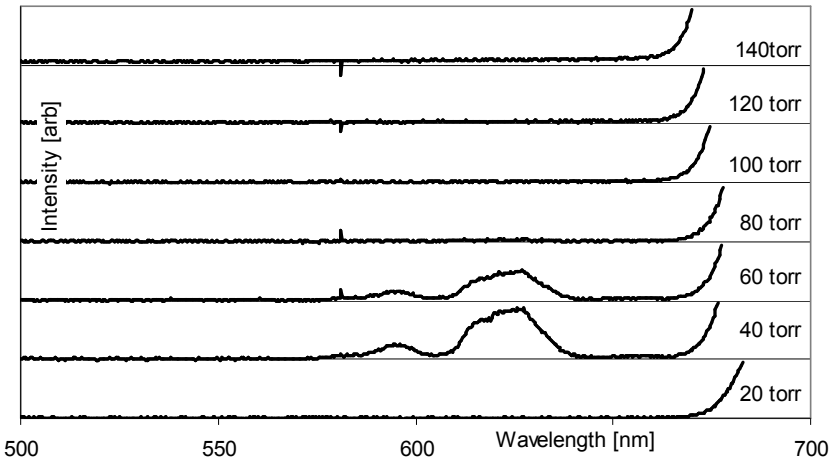

Figure 5.27. Optical spectrum of the photoluminescence of Y_2O_3:Eu particles deposited at 600W absorbed power. The excitation spectrum was filtered using Hoya U340 glass.

The first luminescence study was performed using the U340 filter placed in the excitation light path. The measurements showed that only the samples deposited under 40 Torr and 60 Torr of pressure had measurable luminescence, this is shown in Figure 5.27 for samples deposited under 600 W of absorbed power. Measurements for samples deposited under different microwave absorbed power conditions had similar photoluminescence properties as a function of pressure.

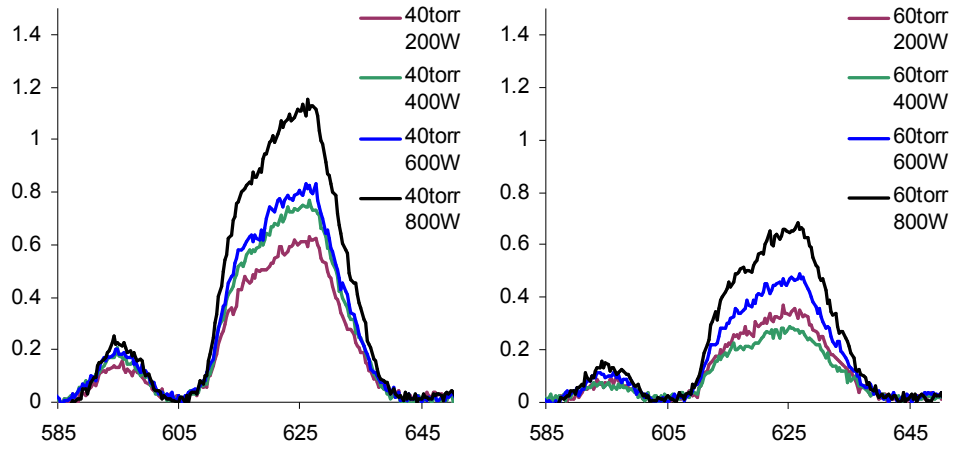

Figure 5.28. The spectral intensity photoluminescence of Y_2O_3:Eu particles deposited at 40 Ttorr and 60 Torr process chamber pressure. The excitation spectrum was filtered using Hoya U340 glass.

The luminescence of the samples deposited under 40 Torr and 60 Torr chamber pressure is shown in Figure 5.28. There are two observable intensity peaks at 595 nm and 626 nm. The spectrometer used in the experimental setup had an optical resolution of 9 nm FWHM. As a result, any features narrower than 9 nm are not distinguishable in Figure 5.28.

While comparing the photoluminescence intensity between different samples it is important to notice that the intensity of the photoluminescence does depend on the amount of the luminescent material on the sample. Although the material flow was kept constant for all deposited samples and the deposition times are constant, the actual deposited coating thickness or mass is unknown for the samples. For this study, the actual luminescence of the sample, regardless of the coating thickness or mass, was compared.

From Figure 5.28 it can be seen that the luminescence increases with process absorbed power and is larger for samples deposited at 40 Torr than 60 Torr. This trend is summarized in Figure 5.29 below. Because of the limited samples' deposition power range of this study, it is unknown where the intensity of the luminescence reaches its maximum within the power pressure range tested. This indicates the need for further study of new samples deposited under higher absorption power.

Because there are only two luminescent samples at each power level it was not possible to fully present the luminescence intensity as a function of pressure. However, from Figure 5.28 it is clear that the intensity of the samples deposited at 40 Torr deposition chamber pressure is higher than those deposited at 60 Torr.

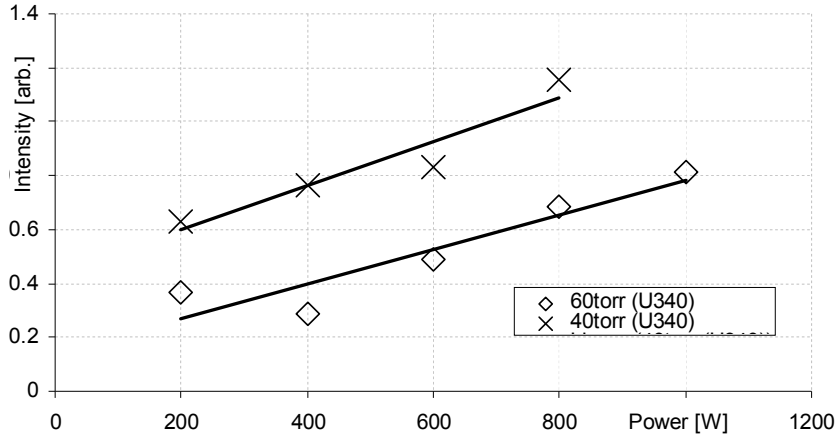

Figure 5.29. Luminescence intensity as a function of sample deposition absorbed power. The excitation spectrum was filtered using Hoya U340 glass.

The luminescence study was repeated with the excitation filter changed to the Hoya U330 filter. Other parameters of the study were kept consistent with the first part of the luminescence study.

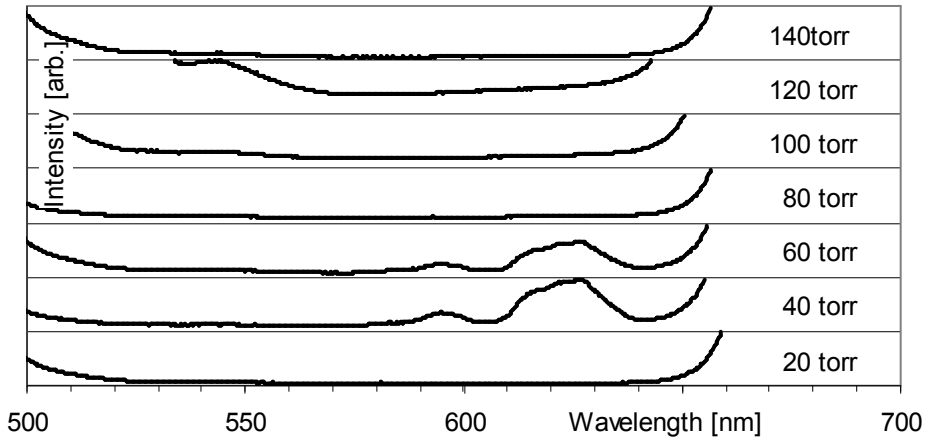

Figure 5.30. Optical spectrum of the photoluminescence of Y_2O_3:Eu particles deposited at 600 W absorbed power. The excitation spectrum was filtered using Hoya U330 glass.

Similar to the first part of luminescence study the measurements showed that only the samples deposited at 40 Torr and 60 Torr pressure had measurable luminescence. This is shown in Figure 5.30 for samples deposited under 600 W absorbed power.

Measurements for samples deposited under different absorbed power conditions have similar results.

The luminescence of the samples deposited under 40 Torr and 60 Torr chamber pressure is shown in Figure 5.31. The luminescence with peak intensity at 595 nm and 626 nm is similar to the results shown in Figure 5.28. Again, features which are narrower than the 9 nm resolution limit are not visible in Figure 5.31.

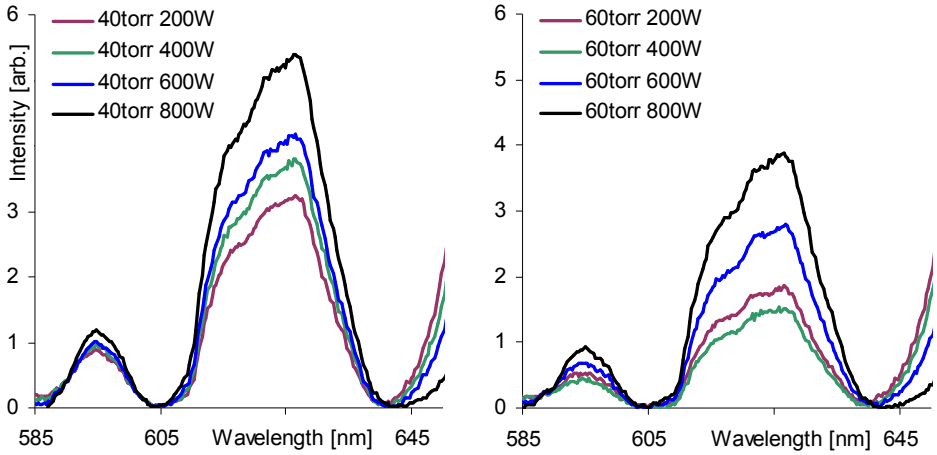

Figure 5.31. The photoluminescence of Y_2O_3:Eu particles deposited at 40 Torr and 60 Torr process chamber pressure. The excitation spectrum was filtered using Hoya U330 glass.

From Figure 5.31 can be seen that the luminescence increases with process absorbed power and is larger for samples deposited at 40 Torr than 60 Torr. This trend is summarized in Figure 5.32.

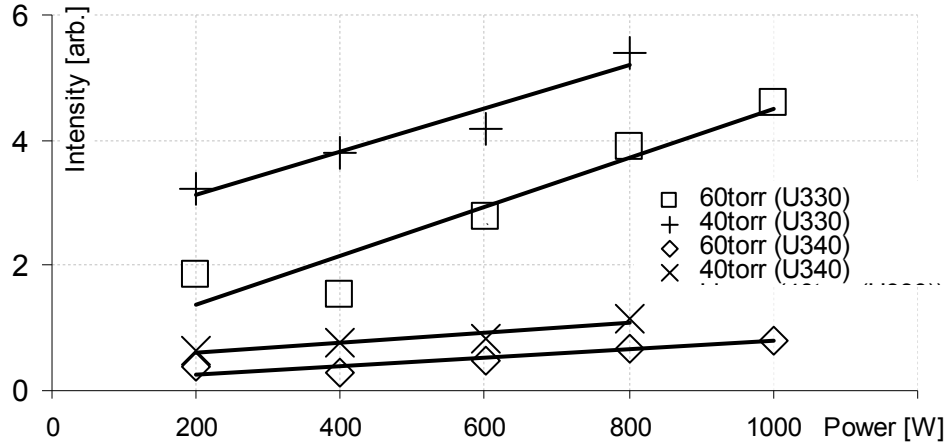

Figure 5.32. Luminescence intensity as a function of sample deposition Absorbed power.

The luminescence spectral response in this measurement is similar to the luminescence measurement where the U340 excitation filter was used. However, the intensity of the luminescence is significantly higher. The luminescence intensity when using the U330 filter has been increased by five times as compared to the study when the U340 filter was used.

The increase in luminescence intensity can be explained by comparing the excitation spectrum in the experiment that used the U330 filter to the experiment with U340 filter (Figure 5.33). This can be explained by looking at the absorption range of the Y_2O_3 nano-particles. The published absorption studies of Y_2O_3:Eu (Figure 5.33) show that the maximum absorption occurs at 250 nm. However, the peak intensity of excitation source used for this luminescence study is 330 nm and 340 nm for U330 and U340 filters, respectively. However, there is an overlap of the published absorption range of Y_2O_3:Eu and the excitation range in the experimental setup as it is shown in Figure 5.33. The excitation spectrum during the experiment utilizing both U330 and U340 filters clearly overlaps the absorption spectra of the Y_2O_3:Eu. However, the experiment utilizing the

U330 filter has greater overlap than in case of the U340 filter, which can explain the stronger photoluminescence in the experiment utilizing the U330 filter.

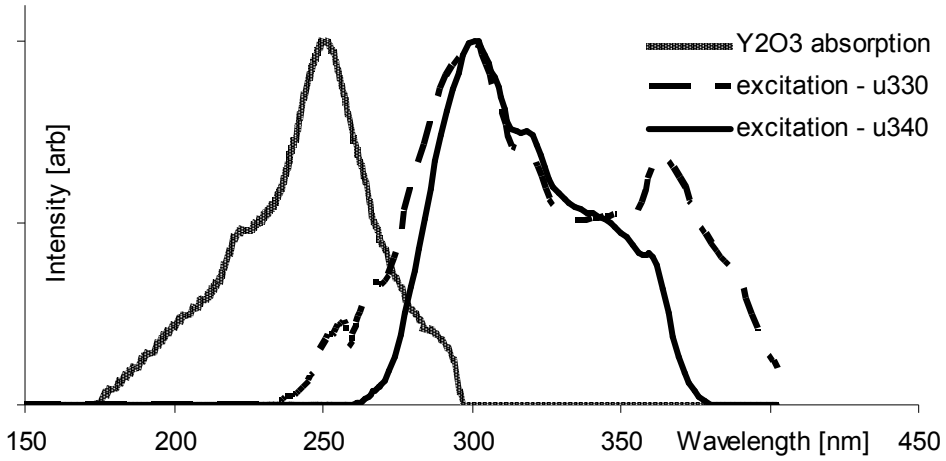

Figure 5.33. Comparison between the Y_2O_3:Eu absorption spectrum and the excitation spectrum of experiment with U330 and U340 excitation light filters.

The effect of the absorption and excitation spectral overlap on luminescence can be estimated. The intensity of luminescence will depend on the amount of the energy absorbed by the sample. The absorption range and excitation spectral profiles allow calculation of the difference between the two experiments due to the different excitation sources. In the calculations the Xenon lamp and the filter manufacturer's data was utilized together with the absorption study published in. The effective absorbed energy was calculated by multiplying the absorption and the excitation intensity at each wavelength in the 200 to 300 nm range.

The calculated effective absorbed spectrum for the experiment with U330 and U340 filters is presented in Figure 5.34. It is clear that the sample absorbs significantly less energy in experiment with the U340 filter than with the U330 filter. Simple integration shows that the energy absorbed by the sample in the experiment with U330 filter is about 3.5 times larger than with the U340 filter. This difference can be the most

significant reason for the difference in luminescence intensity between the experiment with U330 and U340 filters.

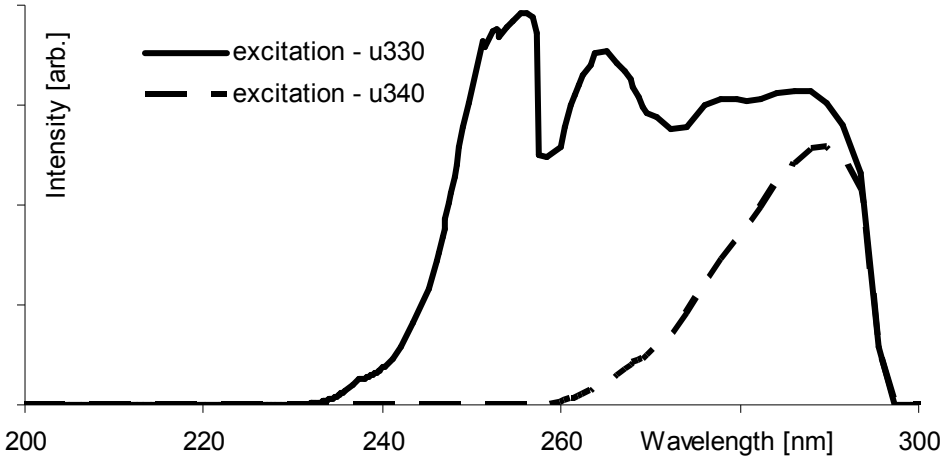

Figure 5.34. The spectrum of absorbed excitation light in experiment with U330 and U340 excitation path filter.

The lack of luminescence at pressures of 60 Torr and above combined with the crystal lattice size sheds light onto the state of the Eu doping in the crystal. Comparing lattice volume size and luminescence study shows that the samples with larger lattice volume are also the samples that luminescence. It is possible that the luminescence is due to the Eu^{3+} ion replacing the Y^{3+} ion of the Y_2O_3 structure. Since the ionic radius of the Eu^{3+} ion is larger than of the Y^{3+} ion then the lattice of Eu doped Y_2O_3 it is expected to increase if the Eu^{3+} ion is activated to the lattice location.

The luminescence study showed that the samples of Y_2O_3:Eu prepared using MPASD system do exhibit luminescence under some deposition conditions. The luminescence was observed only for the samples deposited under pressures of 40 and 60 Torr. The samples deposited under 40 Torr did luminescence more intensely than the samples deposited under 60 Torr of pressure by a factor of two. There is a luminescence dependence on power and the samples deposited at higher power levels luminescent

stronger. The lack of luminescence in samples deposited at 80 Torr and above is observed for samples with smaller lattice size. This suggest that Eu is not activated into lattice size in the samples deposited at pressures of 80 Torr and higher.

Although the absorption study was not performed, the use of two different excitation filters during the study showed different luminescence levels consistent with the published absorption data for Y_2O_3:Eu .

5.10. Chapter Summary

The deposition of Y_2O_3:Eu using MPASD system was successful. MPASD system allowed for synthesis of a crystalline nanoparticle coatings of Y_2O_3:Eu without the need for further post annealing. The effects of process pressure and process microwave power on the optical and structural properties of the deposited samples were presented.

As deposited the coatings had monoclinic structure and annealing did not change the structure to the more common cubic phase. Changes in properties of the coating with changing process parameters were observed. The coatings luminescence and crystal size depended on the deposition conditions. This suggests that the process parameters can be controlled to yield desired coating properties.

LIST OF REFERENCES

Abdelsayed, V. , Glaspell, G. , Nguyen, M. , Howe, J.M. , El-Shall, S. (2008) Laser synthesis of bimetallic nanoalloys in the vapor and liquid phases and the magnetic properties of PdM and PtM nanoparticles (M=Fe, Co and Ni). The Royal Society of Chemistry: Faraday Discussions. 138, 163-180.

Anh, T. , Benalloul, P. , Barthou, C. , Giang, L. , Vo, N. , Minch, L. (2007) Luminescence, energy transfer, and upconversion mechanisms of Y_2O_3 nanomaterials doped with Eu3+, Tb3+, Tm3+, Er3+, and Yb3+ ions. Journal of Nanomaterials. 48247.

Astruck, D. , Lu, F. , Aranzaes, J.R. (2005) Nanoparticles as recyclable catalysts: the frontier between homogeneous and heterogeneous catalysts. Angewandte Chemie International Edition. 44, 7852-7872.

Avvaru, B. , Patil, M.N. , Gogate, P.R. , Pandit, A.B. (2006) Ultrasonic atomization: effect of liquid phase properties. Ultrasonics. 44, 146-158.

Baughman, R.H. , Anvar, A.Z. , de Heer, W.A. (2002) Carbon nanotube – the routhe toward applications. Science. 297, 787-792.

Baughman, R.H. , Cui, C. , Zakhidov, A.A. , Iqbal, Z. , Barisci, J.N. , Spinks, G.M. , Wallace, G.G. , ... Kertesz, M. Carbon nanotube actuators. Science. 284, 1340-1344.

Baum, R. (2003) Drexler and Smalley make the case for and against ‘molecular assemblers’. Chemical & Engineering News. 81 (48), 37-42.

Bhargava, R.N. , Gallagher, D. (1994) Optical properties of manganese-doped nanocrystals of ZnS. Physical Review Letters. 72 (3), 416-419.

Borgia, I. , Brunetti, B. , Mariani, I. , Sgamellotti, A. , Cariati, F. , Fermo, P. , Mellini, M. , Viti, C. , Padeletti, G. (2002) Heterogenous distribution of metal nanocrystals in glazes of historical pottery. Applied Surface Science. 185, 206-216.

Camillone, N. , Adib, K. , Fitts, J. , Rim, T.R. , Flynn, G.W. , Joyce, S.A. , Osgood, R.M. (2002) Surface termination dependence of the reactivity of single crystal hematite with CCl4. Surface Science. 511, 276-282.

Champion, Y. (2007) Gas phase synthesis of nanopowders. Nanomaterials and Nanochemistry (16). Retrieved from www.springerlink.com

Chen, Q. , Zhou, M. , Fu, Y. , Weng, J. , Zhang, Y. , Yue, L. , Xie, F. , Huo, C. (2008) Magnetron sputtering synthesis silver and organic PEO nanocomposite. Surface & Coatings Technology. 202, 5576-5578.

Das, S.K. , Putra, N. , Thiesen, P. , Roetzel, W. (2003) Temperature dependance of thermal conductivity enchancement for nanofluids. Journal of Heat Transfer. 125, 567-574.

Dreesen, L. , Colomer, J. , Limage, H. , Giguère, A. , Lucas S. (2009) Synthesis of titanium dioxide nanoparticles by reactive DC magnetron sputtering. Thin Solid Films. 518, 112-115.

Drexler K. E. (1986) Engines of creation. Garden City, N.Y.: AnchorPress/Doubleday.

Drexler K. E. (1992) Nanosystems: molecular machinery, manufacturing, and computation. New York, N.Y.: Willey.

Eigler, D. M. , Schweizer, E. K. (1990) Positioning single atoms with a scanning tunnelling microscope. Nature. 344, 524-526.

Faraday, M. (1857) The Bakerian lecture: Experimental relations of gold (and other metals) to light. Phillosophical Transactions of the Royal Society of London. 147, 145-181.

František, H. (1984) Real structure of undoped Y_2O_3 single crystals. Acta Crystallographica Section B. B40, 76-82.

Freestone, I. , Meeks, N. , Sax, M. , Higgitt, C. (2007) The Lycurgus cup – a Roman nanotechnology. Gold Bulletin. 40 (4), 270-277.

Gao, P.X. , Mai, W. , Wang, Z.L. (2006) Superelasticity and nanofracture mechanics of ZnO nanohelices. Nano Letters. 6 (11), 2536-2543.

Gell, M. , Jordan, E.H. , Teichoiz, M. , Cetegen, B.M. , Padute, N.P. , Xie, L. , Chen, D. , Ma, X. , Roth, J. (2008) Thermal barrier coatings made by the solution precursor plasma spray process. Journal of Thermal Spray Technology. 17 (1), 124-135.

Geohegan, D. B. , Puretzky, A. A. , Rouleau C. , Jackson J. , Eres, G. , Liu, Z. , Styers-Barnett, D. , Hu, H. , Zhao, B. , Ivanov, I. , Xiao, K. , More, K. (2009) Laser interactions in nanomaterials synthesis. Laser-Surface Interactions for New Materials Production (1). Retrieved from www.springerlink.com.

Goldstein, A.N. , Echer, C.M. , Alivisatos, A.P. (1992) Melting in semiconductor nanocrystals. Science. 256 (5062), 1425-1427.

Golovchenko, J. A. (1986) The tunneling microscope: a new lok at the atomic world. Science. 232. 48-53.

Griem, H.R. (1997) Principles of plasma spectroscopy. Cambridge; New York: Cambridge University Press.

Griffin, E.J. (1976) Design of 3-screw tuners. Electronics Letters. 12 (25), 657-658.

Guo, B. , Harvey, A. , Risbud, S.H. , Kennedy, I.M. (2006) The formation of cubic and monoclinic Y_2O_3 nanoparticles in a gas-phase flame process. Philosophical Magazine Letters. 86 (7), 457-467.

Guyot, Y. , Moncorgé, R. , Merkle, L.D. , Pinto, A. , McIntosh, B. , Verdun, H. (1996) Luminescence properties of Y_2O_3 single crystals doped with Pr3+ or Tm3+ and codoped with Yb3+, Tb3+ or Ho3+ ions. Optical Materials. 5, 127-136.

Hao, B. V. , Huy, P. T. , Khiem, T. N. , Ngan, N. T. T. , Duong, P.H. (2009) Synthesis of Y_2O_3:Eu3+ micro- and nanophosphors by sol-gel process. Journal of Physics: Conferences Series. 187, 1-6.

Herlin, M.A. , Brown, S.C. (1948) Breakdown of gas at microwave frequencies. Physical Review. 74 (3), 291-296.

Hottel, H.C. (1967) Radiative transfer. New York, McGraw-Hill.

Hullman, A. (2007) Measuring and assessing the development of nanotechnology. Scientometrics. 70 (3), 739-758.

Ibrahim, E.A. , Marshall, S.O. (2000) Instability of a liquid jet of parabolic velocity profile. Chemical Engineering Journal. 76, 17-21.

Irish, R.T. , Bryant, G.H. (1964) Determination of ionization rate and electron temperature in a mercury discharge by a microwave method. Proceedings of Physical Society. 84, 975-982.

Javey, A. , Guo, J. , Wang, Q. , Lundstrom, M. , Dai, H. (2003) Ballistic carbon nanotube field-effect transistors. Nature. 424 (7), 654-657.

Jerby, E. , Golts, A. , Shamir Y. , Wonde, S. , Mitchell, B.A. , LeGarrec, J.L. , Narayanan, T. , Sztucki, M. , Ashkenazi, D. , Barkay, Z. , Eliaz, N. (2009) Nanoparticle plasm elected directly from solid copper localized microwaves. Applied Physics Letters. 95, 191501.

Jia, L. , Gitzhofer, F. (2010) Induction plasma synthesis of nano-structured SOFCs electrolyste using solution and suspension plasma spraying: a comparative study. Journal of Thermal Spray Technology. 19 (3), 566-574.

Jollet, F. , Noguera, C. , Thormat, N. , Gautier, M. , Duraud, J.P. (1990) Electronic structure of yttrium oxide. Physical Review B. 42 (12), 7587-7595.

Kawarada, H. (1996) Hydrogen-terminated diamond surfaces and interfaces. Surface Science Reports. 26, 205-259.

Keblinski, P. , Phillpot, S.R. , Choi, S.U.S. , Eastman, J.A. (2002) Mechanisms of heat flow in suspensions of nano-sized particles (nanofluids). International Journal of Heat and Mass Transfer. 45, 855-863.

Kettani, M.A. , Hoyaux, M.F. (1973) Plasma Engineering. New York: Wiley.

Kiss'ovski, Z. , Brochhaus, A. , Korzec, D. , Kytzia, S. , Engemann, J. (2007) Plasma parameters of an oxygen microwave discharge obtained by probe diagnostics: I. radial distributions. Plasma Sources Science and Technology. 16, 523-528.

Kiss'ovski, Z. , Tsankov, T. , Korzec, D. , Kytzia, S. , Engemann, J. (2006) Plasma parameters of an oxygen microwave discharge obtained by probe diagnostics: I. axial distributions. Plasma Sources Science and Technology. 15, 126-134.

Kitamura, N. , Sakamoto, T. , Matsuura, H. , Akatsuka, H. (2005) Dependence of vibrational and rotational temperatures of microwave discharge nitrogen-oxygen mixed discharge on their mixture ratio. Bulletin Research Labolatory for Nuclear Reactors.29 (1), 118-120.

Kuliński, J. , Kur, E. , Bednarczyk, D. (1998) Loop directional coupler for rectangular waveguides with small dimensions. Microwaves and Radar, 1998. MIKON '98., 12th International Conference on. 2, 615-619.

Lacas, F. , Versaevel, P. , Scouflaire, P. , Coeur-Joly, G. (1994) Design and performance of an ultrasonic atomization system for experimental combustion applications. Particle & Particle Systems Characterization. 11 (2), 166-171.

Litchfield, R.B. (1973) Tom Wedgwood, the first photographer. New York: Arno Press.

Lu, A , Salabas, E.L. , Schüth, F. (2007) Magnetic nanoparticles: synthesis, protection, fictionalization, and application. Angewandte Chemie International Edition. 46, 1222-1244.

Mädler, L. , Kammler, H.K. , Mueller, R. , Pratsinis, S.E. (2002) Controlled synthesis of nanostructured particles by flame spray pyrolysis. Journal of Aerosol Science. 33, 369-389.

Maslen, E.N. , Streltsov, V.A. , Ishizawa, N. (1996) A synchrotron x-ray study of the electron density in c-type rare earth oxides. Acta Crystallographica Section B. B52, 414-422.

Mazur, A. , Kostka, S. (2004) Loop coupler in rectangular waveguide working near to the cut-off frequency. Microwaves, Radar and Wireless Communications, 2004. MIKON-2004. 15th International Conference on. 2, 751-754.

Meijernik, A. (2008) Exciton dynamics and energy transfer processes in semiconductor nanocrystals. Semiconductor Nanocrystal Quantum Dots. Retrieved from www.springerlink.com.

Melmed, A. J. (1996) Recollections of Erwin Müller's labolatory: the development of FIM (1951-1956). Applied Surface Science. 94, 17-25.

Messing, G.L. , Zhang, S. , Jayanthi, G.V. (1993) Ceramic powder synthesis by spray pyrolysis. Journal of the American Ceramic Society. 76 (11) 2707-2726.

Mie, G. (1908) Beiträge zur Optik trüber Medien, speziell kolloidaler Metallösungen. Annalem der Physik. 25 (3), 377-445.

Min'ko, N. I. , Nartsev, V. M. (2008) Sciencefor Glass Production : Nanotechnology in glass materials (review). Glass and Ceramics. 65 (5), 148-153.

Mizutani, Y. , Uga, Y. (1972) An investigation on ultrasonic atomization. Bulletin of the JSME. 15 (83), 620-627.

Mooney, J.B. , Radding, S.B. (1982) Spray pyrolysis processing. Annual Review of Materials Science. 12, 81-101.

Muehe, C.E. (1968) A high-power waveguide tuner. IEEE Transactions on Microwave Theory and Techniques. 16 (10), 882-883.

Padovani, S. , Boriga, I. , Brunetti, B. , Sgamellotti, A. , Giulivi, A. , D'Acapito, F. , Mazzoldi, P. , Sada, C. , Battaglin, G. (2004) Silver and copper nanoclusters in the lustre decoration of Italian Renaissance pottery: and EXAFS study. Allied Physics A. 79, 229-233.

Pankhurst, Q.A. , Connolly, J. , Jones, S.K. , Dobson, J. (2003) Applications of magnetic nanoparticles in biomedicine. Journal of Physics D: Allied Physics. 36, R167-R181.

Pellerin, S. , Cormier, J.M. , Richard, F. , Musiol, K. , Chapelle, J. (1996) A spectroscopic diagnostic method using UV OH band spectrum. Journal of Physics D: Applied Physics. 29, 726-739.

Pfender, E. (1999) Thermal plasma technology: where do we stand and where are we going?. Plasma Chemistry and Plasma Processing.19 (1), 1-31.

Poland, C.A. , Duffin, R. , Kinloch, I. , Maynard, A. , Wallace, W.A. , Seaton, A. , Donaldson, A. (2008) Carbon nanotubes introduced into the abdominal cavity of mice show asbestos-like pathogenicity in a pilot study. Nature: Nanotechnology. 3, 423-428.

Rabat, H. , Izarra, C. (2004) Check of OH rotational temperature using an interferometric metchod. Journal of Physics D: Applied Physics. 37, 2371-2375.

Reitz, R.D. , Bracco, F.V. (1982) Mechanism of atomization of a liquid jet. Physics of Fluids. 25, 1730-1742.

Ruska, E. (1987) The development of the electron microscope and of electron microscopy. Reviews of Modern Physics. 59 (3), 627-638.

Salerno, M. , Landoni, P. , Vergantti, R. (2008) Designing foresight studies for nanoscienceand nanotechnology (NST) future developments. Technological Forecasting & Social Change.75, 1202-1223.

Scattergood, R.O. , Koch, C.C. , Murty, K.L. , Brenner, D. (2008) Strenghtening mechanisms in nanocrystalline alloys. Materials Science and Engineering A. 493, 3-11.

Schmid et al. (2006) Nanotechnology. Assessment and perspective. Berlin ; New York: Springer.

Scott, P.E. (9169) Microwave scattering by turbulent plasma. Journal of Physics A: General Physics. 2 (2), 75-86.

Sheen, S. , Yang, S. , Jun, K. , Choi, M. (2009) One-step flame method for the synthesis of coated composite nanoparticles. Journal for Nanoparticle Research. 11 (7), 1767-1775.

Shiraishi, K. (1996) First-principles calculations of surface adsorption and migration on GaAs surfaces. Thin Solid Films. 272, 345-363.

Smalley, R. (2001) Of chemistry, love and nanobots. Scientific American. 10, 76-77.

Stauffer, E. (2003) Concept of pyrolysis for fire debris analysts. Science & Justice. 43, 29-40.

Sun, J. , Simon, S.L. (2007) The melting behavior of aluminum nanoparticles. Thermochimica Acta. 463, 32-40.

Sun, X.L. , Tok, A.I.Y. , Lim, S.L. , Boey, F.Y.C. , Kang, C.W. , Ng, H.W. (2008) Combustion-aided suspension plasma spraying of Y_2O_3 nanoparticles: sunthesis and modeling. Journal of Applied Physics. 103, 034308.

Toumey, C. (2005) Apostolic succession. Engineering & Science. 1, 16-23.

Toumey, C. (2008) Reading Feynman into nanotechnology: a text for a new science. Techné. 12 (3), 133-168.

Touzeau, M. , Vialle, M. , Zellagui, A. , Goussett, G. , Lefebvre, M. (1991) Spectroscopic temperature measurements in oxygen discharges. Journal of Physics D: Applied Physics. 24, 41-47.

Tsuzuki, T. , McCormick, P. (2004) Mechanochemical synthesis of nanoparticles. Journal of Materials Science. 39, 5143-5146.

Walter, P. , Welcomme, E. , Hallégot, P. , Zaluzec, N. J. , Deeb C. , Castaing J. , Veyssière, P. , Bréniaux, R. , Lévêque, J., Tsoucaris, G. (2006) Early use of PbS nanotechnology for an ancient hair dyeing formula. Nano Letters. 6 (10), 2215-2219.

Wang, L. , Pan, Y. , Ding, Y. , Yang, W. , Mao, W.L. , Sinogeikin, S. , ... Mao, H. (2009) High-pressure induced phase transitions of Y_2O_3 and Y_2O_3:Eu^{3+}. Applied Physics Letters. 94, 061921.

Watanawanyoo, P. , Chaitep, S, Hirahara, H. (2009) Development of an air assisted fuel atomizer (liquid siphon type) for a continuous combustor. Americal Journal of Applied Sciences. 6 (3), 380-386.

Witanachchi, S. , Dedigamuwa, G. , Mukherjee, P. (2007) Laser-assisted spray pyrolysis process for the growth of TiO2 and Fe2O3 nanoparticle coatings. Journal of Materials Research. 22 (3), 649-654.

Yakel, H.L. (1979) A refinement of the crystal structure of monoclinic europium sesquioxide. Acta Crystallographica Section B. B35, 654-659.

Yang, H. , Hu, Y. , Zhang, X. , Qiu, G. (2004) Mechanochemical synthesis of cobalt nanoparticles. Materials Letters. 58, 387-389.

Yoda, T. , Miyamoto, S. , Tsuboya, H. (2004) Widely tunable CW Nd-doped Y_2O_3 ceramic laser. Conference on Laser and Electro-Optics.

Zhang, F.X. , Lang, M. , Wang, J.W. , Becker, U. , Ewing, R.C. (2008) Structural phase transitions of cubic Gd2O3 at high pressures. Physics Review B. 78, 064114.

Zyryanov, S.M. , Lopaev, D.V. (2006) Measurements of the gas temperature in an oxygen plasma by spectroscopy of the transition . Plasma Physics Reports. 33 (6), 563-574.

APPENDICES

APPENDIX A: Electric Diagrams

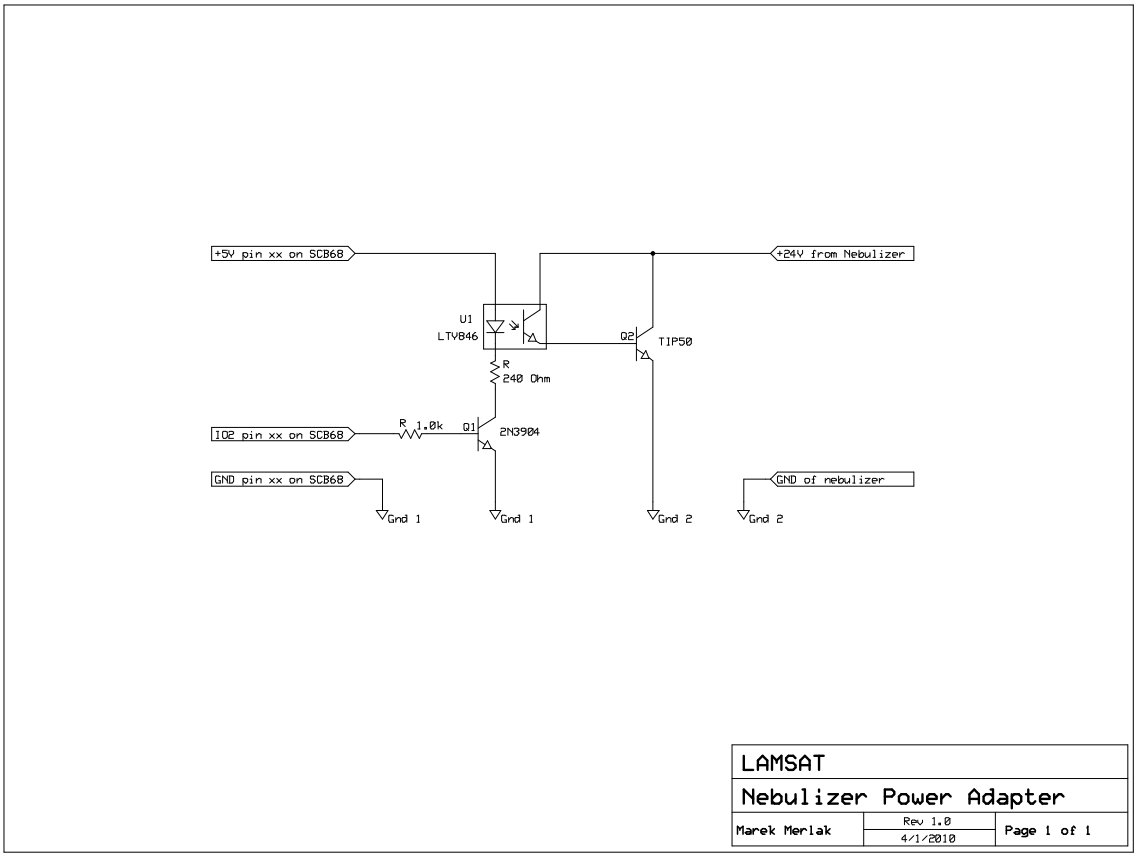

Figure A.1. Electric diagram of nebulizer power control adapter.